國 立 交 通 大 學

電信工程研究所

博 士 論 文

以新型90度耦合器電路設計之汽車防撞警示雷達及短距無線通訊前端電路

Development of Vehicle Collision Warning Radars and Short-Range Communication RF Front-End With New Quadrature Hybrid Based Circuits

研 究 生 ：何丹雄 Tan-Hsiung Ho

指導教授 ：鍾世忠博士 Dr. Shyh-Jong Chung

中 華 民 國 九十九 年 六 月

摘　　要

本論文提出利用 90 度耦合器組成的新型微波電路架構，用於開發汽車防撞警示雷達系統及短距無線通訊系統前端電路，提出利用新型電路設計之雷達及無線收發機架構，達成雷達及無線通訊系統前端電路精簡化。

本論文的第一部分提出三種 90 度耦合器構成的新型電路，一個新型 LO 穿透式混頻器，此混頻器由一個 90 度枝狀耦合器及兩個蕭基特二極體組成，此混頻器有將本地振盪信號傳輸至天線埠之特性。接著提出 LO 穿透式 IQ 混頻器架構，此 IQ 混頻器由兩個穿透式混頻器加上 45 度延遲線及兩個 90 度枝狀耦合器構成。如同一般 IQ 混頻器，所提出的 LO 穿透式 IQ 混頻器除了可同時接收信號的振福及相位外，也具備將本地振盪信號傳輸至天線埠的特性，應用於雷達收發機中接收時並不會有額外的接收功率損耗在功率分配網路上，可提高整體的功率使用效率。接著提出一個創新的全雙工雙向放大器，此雙向放大器由一個 90 度耦合器及兩個反射式放大器組成，所提出的放大器具有將傳輸及接收信號同時放大的特性；具備此特性，將此放大器應用在無線收發機前端電路中可省去信號切換器的使用。

本論文的第二部分提出一個 10.5 GHz 的都普勒雷達收發機。傳統單一天線架構的雷達收發機有本地振盪器信號使用效率不佳的問題，在此本文提出一個利用穿透式 IQ 混頻器設計的新型雷達收發機架構，用以改善本地振盪信號使用效率並將雷達前端電路精簡化。文中將實現一個利用 LO 穿透式 IQ 混頻器構成的 10.5 GHz 都普勒雷達收發機，此收發機採用一個 DGS (Defected-Ground-Structure)結構設計的本地振盪器，結合鎖相迴路構成的頻率產生器當作本地信號源，設計出來的雷達收發機可以操作在 10.36 至 10.74 GH，其輸出功率為 6 dBm。與傳統架構相比，在相同輸入功率 10 dBm 下利用 LO 穿透式 IQ 混頻器設計之收發機可提供多出 3.3 dB 的接收功率；當輸入功率只有 0 dBm 時，所提出之接收機可提供多出 16.2 dB 的接收信號強度。所設計之雷達收發機可用於偵測速度及移動方向並提供 0.25 km/hr 的速度解晰度。

本論文的第三部分提出兩個 FMCW 24 GHz 車用防撞雷達系統，一個側視雷達系統及一個前視雷達系統。此雷達系統由一個 6 GHz 的壓控振盪器驅動，信號經過兩個倍頻器倍頻後產生所需的 24 GHz 信號；一個 12 GHz 的放大器用來提供接收機所需的功率；使用一個次階混頻器來將雷達回波信號降頻至基頻直接處理。針對側視雷達的應用設計一個由微帶天線饋入的號角天線作為收發天線，所有的射頻電路、天線、及基頻控制信號處理板全部整合至一個尺寸為 60 × 45 × 30 mm^3 的模組中，此尺寸使雷達可以裝置在小型車的後照鏡下方。從實驗的結果顯示，此雷達模組當偵測對象是人時可以偵測到 8 公尺的距離，當對象是一台小型汽車時可以偵測至 15 公尺遠。接著提出一個 24 GHz 的前視雷達系統，提出一個 9x8 的串聯饋入式的天線陣列設計。此天線在 E-平面及 H-平面上功率分布都採用中央較高旁邊較低的設計，使的此天線有較好的旁波束能階(SLL)，此天線量測結果可達到 18.5 dBi 的增益，同時在 E-及 H-平面上的半功率波束角度分別為 10.5 及 11.2 度。此雷達系統的等效輻射輸出功率為 23 dBm，整個調變頻寬內只有 0.7 dB 的功率誤差。此論文中也提出一個線性頻率調整機制，此線性頻率調整器能將頻率調變的線性度從 9%的誤差調整至只有 0.3%調變誤差，並且實現 2D(二維)快速傅利業轉換(FFT)演算法來處理回波信號，此演算法可以同時解出待測物的相對距離及速度。從實驗結果，此前視雷達系統可偵測位於 15 公尺外的人，且提供 0.7 km/hr 的相對速度解析度。

最後，本論文將提出一個利用全雙工雙向放大器設計的無線通訊系統前端電路架構，設計一個 10 GHz 雙向放大器，此放大器的傳輸與接收增益分別為 14 與 13 dB。此收發機採用一個八木(Yagi)天線當作收發天線，此天線有 12 dBi 的天線增益，其半功率波束寬度為 40 度。一個典型的環型混頻器用來將基頻信號調變至射頻，且同時將接收到的射頻信號降頻至基頻。整合起來的收發機可提供 15.5 dBm 的等效輻射輸出功率，其整體升降頻的增益皆為 17 dB.

Abstract

This dissertation discusses the development of vehicle collision warning radars and short-range communication RF front-end with new quadrature hybrid composed circuits. A new radar and a communication RF front-end architectures using the proposed circuits are presented with simplified circuit complexity.

In the first part of this dissertation, three new quadrature hybrid composed circuits are presented. A new LO transparent hybrid mixer is proposed, which is composed of a branch-line coupler and two Schottky diodes. The new hybrid mixer can transmit the LO power to the antenna. Then, a LO transmissive quadrature hybrid mixer is proposed. The quadrature hybrid mixer is composed of two hybrid mixer, 45° delay lines, and branch-line couplers. The proposed quadrature hybrid mixer can receive signal with phase. Moreover, the proposed mixer shows high transmission efficiency to pass LO power to antenna and no received power wasted in the oscillator port. A novel full-duplex bi-directional amplifier is then presented. The bi-directional amplifier is composed of a quadrature hybrid and two reflection type amplifiers. The proposed amplifier can enhance the signals in both transmitting and receiving directions, which can be used in a transceiver front-end without using the signal switches.

In the second part, a 10.5 GHz Doppler radar using the proposed LO transmissive quadrature hybrid mixer is presented. The proposed architecture offers higher local power usage efficiency than the conventional ones and simplifies the front-end complexity. A defected-ground-structure local oscillator along with the phase-lock-loop frequency synthesizer is used in the system to provide better phase noise and good frequency stability. The designed transceiver can be operated from 10.36 to 10.74 GHz with output power level of 6 dBm. Compare to the conventional quadrature radar, the proposed one offers 3.3 dB received power more when the LO power is 10 dBm, and

16.2 dB more when the LO power is 0 dBm. The implemented radar can measure the speed and moving direction with 0.25 km/hr resolution.

In the third part, two complete FMCW 24 GHz collision warning radars are presented. The 24 GHz radars are designed for sideway-looking and the forward-looking applications. In the 24GHz radar systems, a 6 GHz VCO, two frequency doublers, a 12 GHz gain block, and a sub-harmonic mixer are developed. In the sideway-looking application, a patch-fed horn antenna is designed. All the RF circuits, antenna, and base-band signal processor are integrated into a dimension of 60 × 45 × 30 mm^3. This size is ready to be installed under the back-mirror of a small car. The developed radar shows a capability to detect a human in 8 meters and a small car located in 15 meters away. In 24 GHz forward-looking radar, a planar 9x8 series-fed patch antenna array is developed. The antenna has an antenna gain of 18.5 dBi, and the half power beam widths are 10.5 and 11.2 degrees, in E- and H-plane respectively. The radar transceiver shows an output EIRP of 23 dBm with only 0.7 dB power deviation within the whole modulation bandwidth. A frequency linearizer mechanism is presented. The frequency linearizer improves the modulation frequency deviation from 9 % to 0.3 %. A 2D-FFT signal processing algorithm is implemented to estimate the object speed and distance, simultaneously. From the experiment, the radar can detect a human up to 15 meters away and measure the relative speed with 0.7 km/h resolution.

In the end of this dissertation, a full-duplex communication RF front-end using the new bi-directional amplifier is presented. A 10 GHz bi-directional amplifier is developed, which has transmission gains of 14 and 13 dB in two directions. A planar Yagi-antenna is adopted. The antenna shows a gain of 12 dBi and half-power beam width 40 degrees. A ring mixer is used as the up / down converter to convert the signal between RF and base-band. The integrated transceiver shows the overall up / down conversion gain of 17 dB and output EIRP 15.5 dBm.

致　　謝

在博士班的求學過程中，首先要誠摯感謝我的指導教授鍾世忠博士，老師悉心的教導，使我得以熟知無線通訊相關理論與實務領域的深奧，並不時的與我討論、修正研究方向，在我遇到瓶頸困難的時候，給予適當的協助，使得這些年獲益匪淺，老師對於學問的嚴謹以及認真積極的處事態度更是我學習的典範。之外，亦得感謝陳俊雄教授、瞿大雄教授、郭仁財教授、張志揚教授、張盛富教授、邱煥凱教授以及郭建男教授，由於諸位口試委員給我的建議與評論，使得本論文能更加完善且嚴謹。

碩博士班七年多的日子裡，實驗室裡共同的生活點滴，不論是學術研究的討論、言不及意的閒聊、出遊玩樂的喜悅、分食食物的瘋狂…等等，都要感謝 912 的學長、同學、學弟妹們，也因爲有你們的陪伴，讓這七年的研究生活變的絢麗多彩。在此特別要感謝的是明仲、怡力、諭正給予我研究上相當大的幫助，譚博、文信等前輩的指導在迷惑時爲我解惑，以及凌博、佑信、明達在學業與研究上的互相砥礪，這些年來實驗室的所有成員們當然也不能忘記，你們的幫助同樣銘感在心。

在此，也要感謝造隆科技公司的成員王協理、朝熙、Gina、瓊千、Jeff，有你們的付出讓我可以有更多時間專心再論文的完成。此外，特別感謝爲我熬夜校稿的明達、珮華與智祥，因爲你們的協助，論文的錯誤修正不少。同時，更要感謝我摯愛的雙親，不只默默地支持我，任何時候也都會做我最溫暖而堅強的後盾，讓我能無後顧之憂的全心研究，進而完成博士班的學業。

最後，謹以此文獻給所有關心我與我關心的人！

何丹雄

List of Figures:

Chapter 1 Introduction

Chapter 2 New Quadrature Hybrid Composed Circuits

Chapter 3 Design and Measurement of a Doppler Radar using the LO Transmissive Quadrature Hybrid Mixer

Chapter 4 24 GHz Vehicle Collision Warning Radars

Chapter 5 A Compact RF Front-End Configuration for Short-Range Communication

List of Tables:

Chapter 1 Introduction

Chapter 3 Design and Measurement of a Doppler Radar using the LO Transmissive Quadrature Hybrid Mixer

Chapter 4 24 GHz Vehicle Collision Warning Radars

Chapter 1 Introduction

Microwave technology has attracted many attentions in many fields. These applications can be grouped into radar and communication systems. The microwave radar technology has been applied in many aspects in our life such as speed detection sensors, vehicle collision warning radars, traffic control monitors, health-care equipments, and motion detectors [1]. Among these applications, high performance, compact size, simple structure, and low cost are the most essential to these radars [2]. This dissertation proposes a new LO transparent hybrid mixer, a LO transmissive quadrature mixer, and a radar front-end architecture using the proposed mixer. By using the presented LO transparent mixer architecture, single antenna radar transceiver front-end can be achieved with simple circuit frame. This dissertation also proposes a novel full-duplex bi-directional amplifier, which can reduce the front-end circuit complexity in a short-range communication system. The first section of this chapter describes the motivation of this research and discusses the related radar front-end and the bi-directional amplifier design literatures. The contributions of this study are presented in the following section. Lastly, the outline of this dissertation is provided.

1.1 Motivation

Followed by the development of economy and technology, vehicle nowadays is quite popular. According to the report from the United Nations Environment Programme (UNEP) in 2009 [3], the total quantity of vehicles in 2050 will be three times as many as recent day. Because of the explosive increase of cars, traffic has become one of the most severe problems in the developed countries. The Intelligent-Transportation System (ITS) is considered as one of the most efficient

solution to the traffic problem [4]-[6]. By sharing the information and managing it, the ITS tends to minimize the traffic problem by tuning the existing transportation network more efficient. The ITS is composed of 5 major parts, (a) the Advanced Traveler Information System (ATIS), (b) Advanced Traffic Management System (ATMS), (c) Advanced Vehicle Control and Safety System (AVCSS), (d) Commercial Vehicle Organization (CVO), and (e) Advanced Public Transportation System (APTC). Among these systems, the (a), (b), (d), and (e) parts are focused on the traffic management and construction of infrastructures. The (c) part is an on board unit.

The AVCSS is also considered as the core to achieve smart transportation system. The AVCSS provides a safer and more comfortable driving experience to the drivers. Because the system is to be installed on a car, the potential market can be expected. The vehicle collision warning radar plays an important role in the AVCSS [7]-[8].

The vehicle collision warning sensor can be realized using sonar, infrared rays, vision, and microwave radar technologies. Because of the superior characteristics of working in all kinds of weather and environmental condition, the microwave radar is chosen by most of the auto-makers. The radar technology was developed since World-War II, as the detector of enemy airplanes. Now the radar has been integrated on a small vehicle, as a driver assistant unit [9]. As a complement of human sense, the automotive radar has been found in many auto-industry applications such as Adaptive Cruise Control (ACC), Blind-Spot Detecting System (BLDS), and so on. The radar can also be built on the road-side, to measure the quantity and average speed of vehicle flow [10]. The information of vehicle flow is quite helpful to the traffic control system.

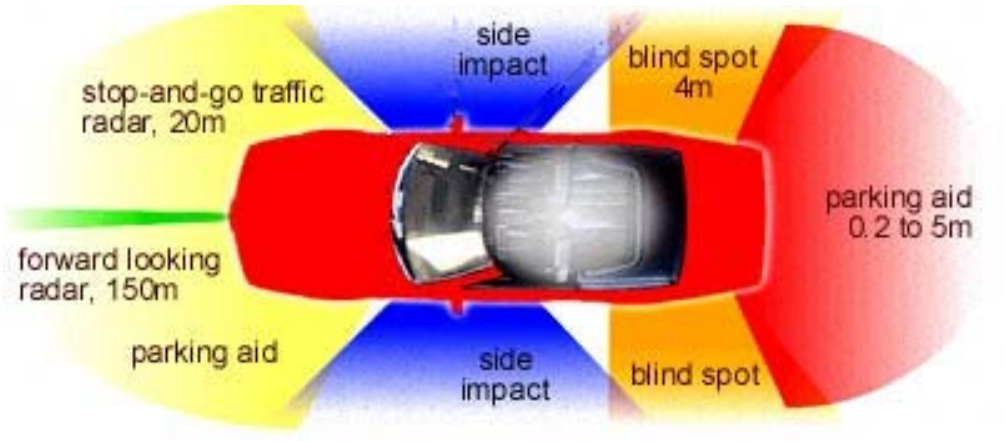

Figure 1.1 A sketch of the automotive radar applications within a car.

In general, there should be a forward-looking radar, two sideward-looking radar, and a backward-looking radar in a single vehicle to cover all the surrounding area, as illustrated in figure 1.1. Each radar takes care a specified region and provides different warning to the driver [11]. For example, the forward-looking radar tracks the distance and relative speed of vehicles in front of the radar vehicle itself, then warns if necessary [12]-[13]. The forward-looking radar gives the driver an extra reaction time, which may help to reduce the car accident rate. The sideward-looking radar detects the blind-spot area of a vehicle. This radar can be a driver assistant system to provide a visual and sound warning. The backward-radar senses the rear region of a vehicle and searches for the potential danger. The backward-radar is significantly useful in large vehicles, which the drivers may not be able to look the back region through a mirror [14]-[15].

Several available sensing technologies can provide solutions to detect objects in the nearby region, such as sonar (ultrasonic wave), light (visible light, laser, infrared rays), and microwave technologies. Table 1-1 [16] gives a comparison of all existing sensing technologies. The sonar fails under high air flow speed environment, thus, this technology is impossible to be used when the vehicle running in high speed. The

infrared rays, laser, and video sensing technologies fail in a dirty or moist environment. Only the microwave radar technology survives in all kinds of weather condition.

Table 1-1 A comparison of the existing sensing technologies.

Technologies / Performance feature	Ultra-sonic	Infrared ray	Laser	Video	Microwave radar
Long range capability	Poor	Fair	Good	Good	Good
Target discrimination capability	Poor	Poor	Fair	Good	Good
Minimizing false alarm	Poor	Poor	Fair	Fair	Good
Temperature stability	Poor	Fair	Good	Good	Good
Darkness penetration	Good	Good	Good	Poor	Good
Adverse weather penetration	Poor	Poor	Poor	Poor	Good
Sensor dirt / moisture performance	Fair	Poor	Poor	Poor	Good

Since 1972, the moat large auto-makers in this world have developed their own automotive radar systems. In 1990s, many applications have been proposed by using the radar technology. To be installed on a small vehicle and accepted by the mass population, developing a compact and low cost radar system becomes the major trend.

The microwave radars are composed of the transmitting / receiving antenna(s), Radio-Frequency (RF) transceiver, and a Digital Signal Processor (DSP). Various modulation mechanisms in both pulsed and Continuous-Wave (CW) type have been developed to obtain the target information [17]. Among these mechanisms the Linear Frequency Modulated Continuous-Wave Modulation (LFMCW) is commonly used in automotive radar applications. This modulation provides target distance and speed information in single acquisition with relative good resolution and simple front-end circuit complexity [18].

Personal wireless communication brings a significant convenience to our life. To be used on a portable device, the compact and relative low cost transceiver architecture is vital. Due to the dramatic increase of the wireless personal communication need in

recent years, numerous new transceiver architectures have been proposed to simplify the front-end circuit configuration and to reduce the system cost. The transceiver with single antenna is considered to have the minimum size. In the typical single antenna architecture, signal switches or diplexers are used to separate the transmitting and receiving paths. These components increase the circuit complexity and thus reflect on the price. The bi-directional amplifier concept is proposed to eliminate the usage of signal split components [19].

1.2 Literature Survey

Among the radar technologies, the CW radars have relatively simple circuit structure, allowing the compact size and low-cost solutions [20]. This kind of radar has been found in many applications within the automotive field such as speed sensor, collision warning radar, and traffic control systems [21]. Among these systems, a single local oscillator (LO) is used to generate transmitting power and drive the receiver at the same time, as shown in figure 1.2.

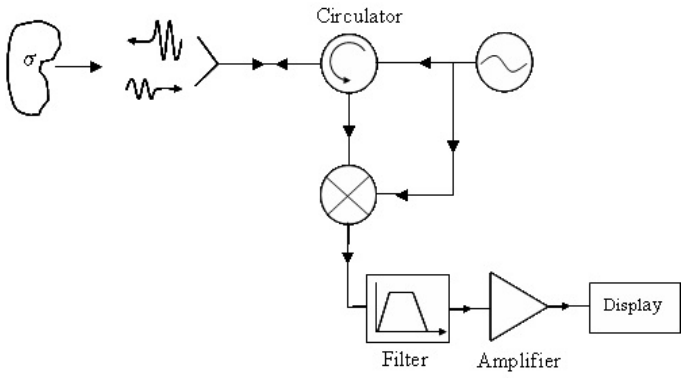

Figure 1.2 Block diagram of the continuous wave radar transceiver.

Because there is only one signal source, the LO power usage efficiency is used to state how efficient the radar front-end use the LO power in both transmitting and receiving ways. For short range applications, the CW radars with low-power LO have

the optimum size and cost. In the associated applications such as health-care sensor and speed detector, a high LO power usage efficiency is crucial to improve the sensing quality. The higher LO power usage efficiency implies higher signal strength can be acquired from the sensor with the same LO power inject into the radar. The systems with two antennas are likely to have best local power usage efficiency regardless the transmission loss in the power distribution network [22]-[23]. However, the system size is twice larger than the system with single antenna. The radar with single antenna is typically implemented with a circulator or a coupler following the antenna. The circulator components usually cost extremely high price, while in the coupler architecture half of the receiving power is dissipated at the LO port, in addition, half of the transmission power is taken to drive the mixer. In this thesis, a new LO transparent type hybrid mixer is proposed in order to improve the power usage efficiency of the local oscillator. The proposed hybrid mixer is placed in series between the signal source and antenna. It has the characteristic to pass the LO power through and down convert the radar signal. The proposed hybrid mixer has been proven that fewer than half power is required to drive the mixer and no power is lost in the receiving path.

The quadrature radars, as shown in figure 1.3, can detect the speed and direction of a target. This kind of radar can also be used to measure the displacement of objects in a static environment [24]-[25]. Extremely small displacements such as human vital signals are detected very well with quadrature mixing technology [26]-[27], because this kind of radar extracts Doppler signal with much higher signal-to-noise ratio [28].

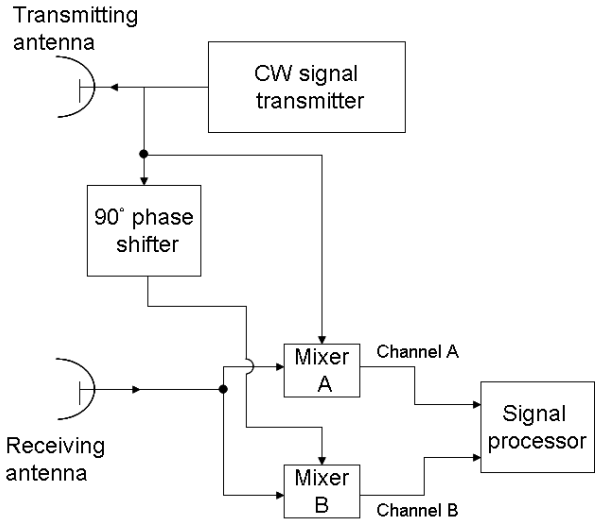

Figure 1.3 A classic quadrature radar architecture.

The typical single antenna quadrature radar architecture applied a coupler to isolate the transmitter and receiver paths. C. Y. Kim [29]-[30] proposed a balanced coupler network and a circularly polarized radar architecture to improve the transmitter-to-receiver leakage. However, these approaches suffer from low power usage efficiency that the reflected LO powers from the mixers are terminated at a resistor and half of the receiving power is dissipated in the LO port. In the following of this dissertation, a LO transmissive quadrature hybrid mixer is proposed. The new quadrature hybrid mixer can perform the same function as the quadrature mixer and improve the local power usage efficiency as well.

In the short-range communication systems, the design of transceiver is not focused on increasing the communication distance but on the convenience in the near proximity area of the users. Thus, the circuit performance can be somewhat sacrificed in order to obtain a compact and low-cost circuit configuration. The typical wireless front-end circuit of the transceivers contains two individual signal paths, one for transmitting and the other for receiving. The use of two individual T/R paths has the advantages of achieving optimum designs for each path and result in an improved communication range and quality. However, these architectures also have the drawbacks of more circuit

components, more complicated circuit layout, and larger circuit area. T. Tsukii [31] and J. W. Archer [32] presented single-path transceiver architectures using a switched bi-directional amplifier. The transmitting signal and the receiving signal share the common RF circuits, and thus simplify the circuitry complexity. However, these architectures can only be used in a half-duplex system. In this dissertation, a compact RF front-end configuration using a novel full-duplex bi-directional amplifier is presented. The proposed bi-directional amplifier is composed of a quadrature hybrid and reflection type amplifiers. Without using the signal switch, this configuration requires only one path for the transmitting / receiving signals and can be used in both half- and full-duplex systems.

1.3 Contributions

In this dissertation, a new LO transparent hybrid mixer, a unique LO transmissive quadrature hybrid mixer, and novel full-duplex bi-directional amplifier architectures are presented. A radar front-end architecture using the proposed hybrid mixer is proposed. The proposed radar architecture can reduce the transmission power loss and has no received power wasted in the signal split network in theory. Thus, an optimized LO power usage efficiency is achieved. A 10.5 GHz Doppler radar system is implemented using the proposed LO transmissive quadrature hybrid mixer architecture. A local oscillator designed with the defected-ground-structure, which possesses a low phase noise, is applied as the local oscillator to the radar. A frequency synthesizer is implemented to provide a stable signal source in all kinds of operation environment. A complete radar transceiver with the proposed quadrature hybrid mixer is implemented and tested.

Two complete 24 GHz vehicle collision warning radars are presented. The radars are

developed for the sideway-looking and forward-looking applications, respectively. The RF front-ends, antennas, and base-band signal processor within the 24 GHz radars are built up. The LFMCW mechanism is applied in these radar systems, also a modulation linearizer is adopted to improve the modulation linearity. A 2D-FFT signal processing algorithm is presented for simultaneously measuring the object relative speed and distance.

A new transceiver front-end architecture using the proposed full-duplex bi-directional amplifier for wireless communication is presented. Without using the signal switch or diplexer, the transceiver fulfills full / half duplex functionalities in single path architecture. The transceiver complexity is minimized when using the bi-directional amplifier.

1.4 Outline of the Dissertation

This dissertation is organized as follows: The chapter-2 proposes the new quadrature hybrid composed circuits. A new LO transparent hybrid mixer is proposed for the radar applications, which offers a solution to reduce the front-end circuit complexity and cost. The operation principle of the proposed hybrid mixer is illustrated. A unique LO transmissive quadrature hybrid mixer is presented, which provides two orthogonal base-band outputs. These orthogonal outputs make the radar receiver able to identify direction of displacement. The basis of the proposed quadrature hybrid mixer is illustrated. Then, a novel full-duplex bi-directional amplifier is also presented, which is proposed to simplify the RF front-end in a wireless communication system. The bi-directional architecture and operation principle are described in this chapter.

Chapter 3 presents a 10.5 GHz quadrature radar using the LO transmissive quadrature hybrid mixer. The implementation of 10.5 GHz radar transceiver is

illustrated, which includes a proposed quadrature hybrid mixer, a 5.25 GHz defected-ground structure VCO, a Phase-Lock Loop (PLL) frequency synthesizer, and an active frequency doubler. The output performance of the implemented transceiver is presented. Then, a performance comparison of the radar front-end architecture between the conventional one and the proposed one using the quadrature hybrid mixer is presented. A test environment is built to simulate a continuously moving object with constant relative speed. At the end of this chapter, the radar transceiver is established as a road-side unit to measure the speed of vehicles passing by.

Chapter 4 presents two complete 24 GHz collision warning radar systems. The 24GHz radars are developed with one for the side-way looking and the other one for the forward-looking applications. A 6 GHz VCO is designed as the signal source, then, two active type frequency doublers multiply the 6 GHz signal to the 24 GHz required signal. A sub-harmonic mixer is adopted in this study to down convert the radar signal to base-band directly. A modulation linearizer mechanism is proposed to provide excellent frequency modulation linearity. A 2D-FFT signal processing algorithm is presented, which shows a capability to acquire the relative speed and distance information of moving objects, simultaneously.

Chapter 5 proposes a new transceiver RF front-end using the full-duplex bi-directional amplifier. The design of bi-directional amplifier is illustrated. A RF front-end composed of a bi-directional amplifier, a ring mixer, and a printed Yagi-antenna is implemented. The proposed architecture shows a capability to transmit / receive signals using single path.

Chapter 2 New Quadrature Hybrid Composed Circuits

In this chapter, a new LO transparent hybrid mixer, a LO transmissive quadrature hybrid mixer, and a novel full-duplex bi-directional amplifier are proposed. These new mixers and amplifier are configured using the quadrature hybrid architecture. Different from the conventional mixers, the proposed hybrid mixers are designed to pass the local oscillator power to the antenna port, and also able to down-convert the received signal from antenna. Having this unique characteristic, the proposed hybrid mixer architecture is suitable to be used in the radar front-end. Using the LO transparent hybrid mixer, single path transmitting / receiving can be accomplished with simple circuit complexity. A LO transmissive quadrature hybrid mixer composed of the new hybrid mixers is then presented. The quadrature hybrid mixer not only has the same performance as the hybrid one but also output both the I / Q IF signals simultaneously. These I / Q signals are useful to distinguish the sign of frequency shift in the Doppler radar applications, which helps to recognize the sign of relative speed. In the end of this chapter, a full-duplex bi-directional amplifier is presented. With the unique characteristic of enhancing the signals in both transmitting and receiving path, the bi-directional amplifier is proposed to simplify the RF front-end complexity when used in a short-distance communication system.

2.1 New LO transparent hybrid mixer

Most radar systems use single signal source as detecting signal and local oscillating signal to the receiver. Among these radar systems the single antenna architecture is considered to have the smallest size and simplest circuit complexity. As

illustrated in figure 2.1 (a), a circulator component is commonly used to isolate the input and output signals in the conventional radar system. However, the circulator device costs extremely high price. In this thesis, a LO transparent hybrid mixer architecture is proposed for the radar applications. As shown in figure 2.1 (b), the proposed hybrid mixer is connected in series between the local source and antenna, which has the capability to bypass the local power to the antenna and down convert the received radar signal to base-band as well.

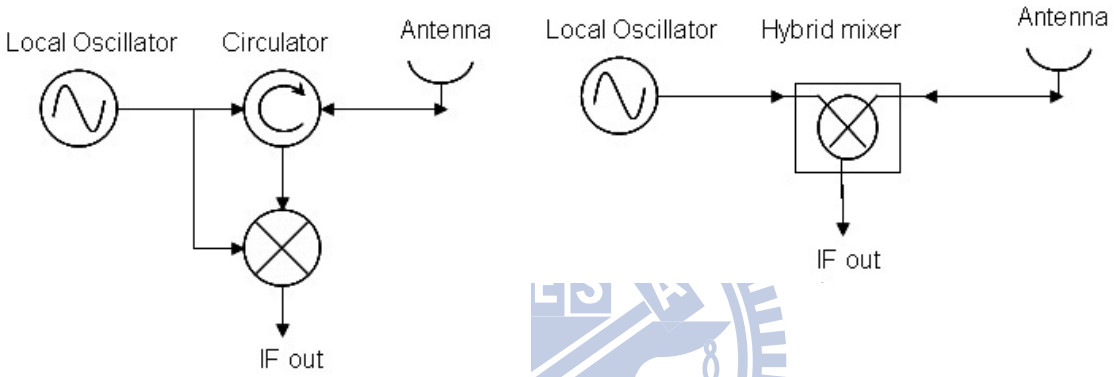

(a) (b)

Figure 2.1 (a) A typical single antenna radar transceiver front-end architecture and (b) the architecture using the proposed LO transparent hybrid mixer.

Owning to the reason that the radar system uses the same signal source as the transmitting signal and down converter driving signal, there is no LO to RF isolation problem in the radar systems. Instead, the idea of LO transparent hybrid mixer tends to maximize the LO to RF transmission. As illustrated in figure 2.2, the new LO transparent hybrid mixer is composed of a 90° half-power coupler, two mixer diodes, and Low-Pass Filters (LPFs).

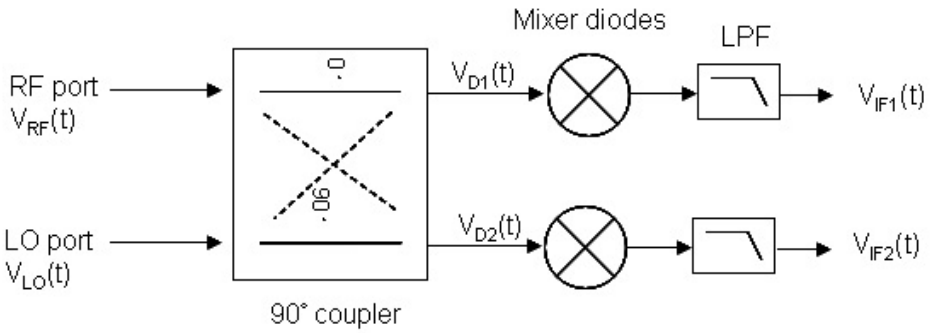

Figure 2.2 The sketch of the new LO transparent hybrid mixer.

Let the RF and LO signals expressed as:

$$V_{RF}(t) = A_{\mathrm{RF}} \cos(\omega_{\mathrm{R}} t + \theta_{RF})$$
$$V_{LO}(t) = A_{\mathrm{LO}} \cos(\omega_{\mathrm{T}} t + \theta_{LO}) \quad (2\text{-}1)$$

where A_{RF} and A_{LO} represent the received and local oscillator amplitude respectively. ω_{R} and ω_{T} indicate the frequencies of the received and transmitted signal. After passing through the 90° coupler, the signals at the mixer diodes can be expressed as:

$$V_{D1}(t) = \frac{A_{\mathrm{RF}}}{\sqrt{2}} \cos(\omega_{\mathrm{R}} t + \theta_{RF}) + \frac{A_{\mathrm{LO}}}{\sqrt{2}} \cos\left(\omega_{\mathrm{T}} t + \theta_{LO} + \frac{\pi}{2}\right)$$
$$V_{D2}(t) = \frac{A_{\mathrm{RF}}}{\sqrt{2}} \cos\left(\omega_{\mathrm{R}} t + \theta_{Rf} + \frac{\pi}{2}\right) + \frac{A_{\mathrm{LO}}}{\sqrt{2}} \cos(\omega_{\mathrm{T}} t + \theta_{LO}) \quad (2\text{-}2)$$

After mixing the contents within $V_{D1}(t)$ and $V_{D2}(t)$, the fundamental term can be filtered out by the LPF and thus expressed as:

$$V_{IF1}(t) = \frac{A_{RF}}{2} \alpha_c \cos\left((\omega_{\mathrm{R}} - \omega_{\mathrm{T}})t + \theta_d - \frac{\pi}{2}\right)$$
$$V_{IF2}(t) = \frac{A_{RF}}{2} \alpha_c \cos\left((\omega_{\mathrm{R}} - \omega_{\mathrm{T}})t + \theta_d + \frac{\pi}{2}\right) \quad (2\text{-}3)$$

these two outputs will be equal amplitude and out of phase. Within Equ. (2-3) α_c represents the conversion efficiency from the RF to IF, which is a function of LO power

strength, diode characteristic, and LPF efficiency.

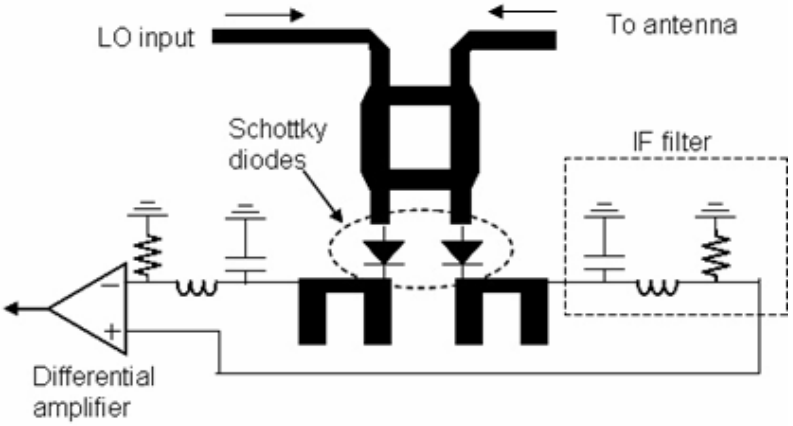

Figure 2.3 Complete circuit schematic of the LO transparent hybrid mixer.

Figure 2.3 gives a complete circuit schematic of the LO transparent hybrid mixer. A branch-line coupler is adopted as the 90° half-power coupler. Two mixer diodes are connected in parallel. A quarter-wavelength open stub is connected at the end of mixer diode. The $\lambda/4$ open stubs provide both the RF and LO signal the small signal ground. An inductor and capacitor composed LPF is connected to the IF output. The resistors connected at each end of the LPF provide discharge paths for the DC components generated by mixer diodes. A differential amplifier which converts the differential output to single-ended with required first stage gain, is connected to the IF outputs,

2.2 The LO transmissive quadrature hybrid mixer

Figure 2.4 (a) and (b) illustrate the block diagrams of the quadrature radar transceivers with conventional mixers and with the proposed LO transmissive quadrature hybrid mixer, respectively. The conventional radar consists of an antenna, an LO source, two branch-line couplers, a two-way power divider, and two mixers along with two LPFs. In this architecture, the first branch-line coupler is used to separate the transmitting and

receiving signals, while the other one is to generate two LO signals with 90° phase difference for quadrature mixing. Half of the output power from the signal source is transferred to the antenna through the first quadrature coupler. During the receiving process, the received signal is coupled to the mixer by the first quadrature coupler and down converted to the base-band by the mixers. The unwanted higher-order harmonic signals are rejected by the LPFs.

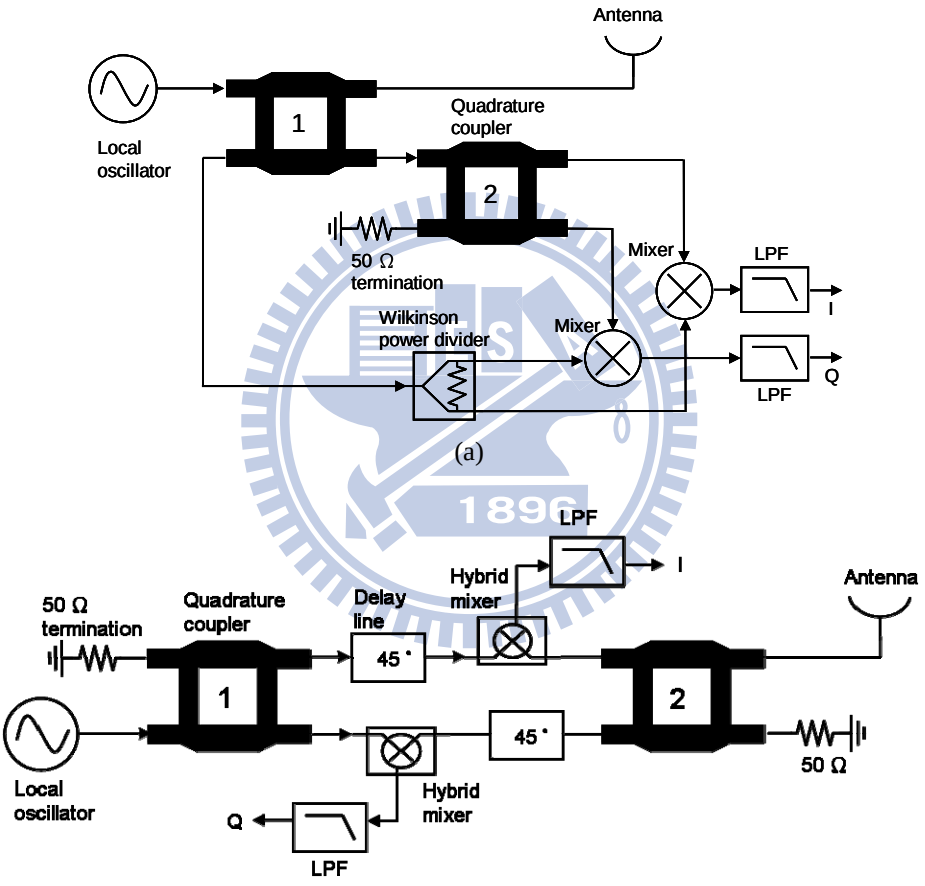

Figure 2.4 Block diagram of (a) conventional quadrature radar with branch-line coupler and quadrature mixer, and (b) the proposed radar with LO transmissive quadrature hybrid mixer.

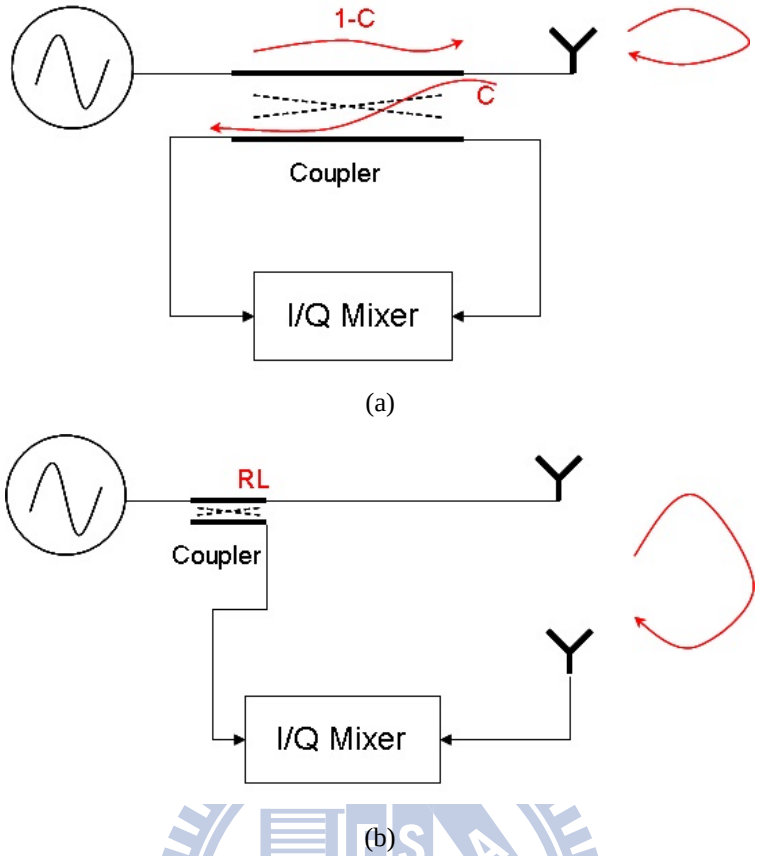

Figure 2.5 The equivalent models of the (a) conventional and (b) proposed radar front-end architecture.

Figure 2.5 shows the equivalent models of the conventional architecture and the proposed one. In figure 2.5 (a), C represents the coupling coefficient of the first coupler, which is 0.5 when using the branch-line coupler. In figure 2.5 (b), The RL indicates the power loss due to a certain of the LO power is taken to pump the mixer diodes. From the ideal model, the conventional architecture shown in figure 2.4 (a) has significant power loss. In spite of the transmission loss contributed by the transmission lines and path loss from antenna to object, there are always 6 dB power loss contributed by the quadrature coupler in theory. There is 3 dB power loss in the transmitting path that half of the transmitting power is transferred to drive the mixers. Another 3 dB loss that half of the received power is terminated at the LO port in the receiving path. The proposed architecture shown in figure 2.4 (b) is used to solve problem. During transmitting process, the LO power is equally divided by the first quadrature coupler and put into the

LO transparent hybrid mixers. The hybrid mixer takes the necessary energy it needs to drive the mixing diodes only, and then pass the remnant power through. Eventually, the remained power from the two hybrid mixers is combined at the antenna port of the second quadrature coupler. When receiving, the second quadrature coupler divides the received power equally with 90° phase difference and put into the mixers. In theory, this architecture has 6 dB enhancement of overall performance from the equivalent model. In practice, a certain of LO power injected into the hybrid mixer is taken to drive the mixer diodes. The power taken by mixer diodes is typically lower than half of the total LO power. Therefore, the overall LO power is efficiently used in this architecture. Note that there are two 45° delay lines placed individually in the upper and lower paths to produce the required phase difference of I / Q IF signals.

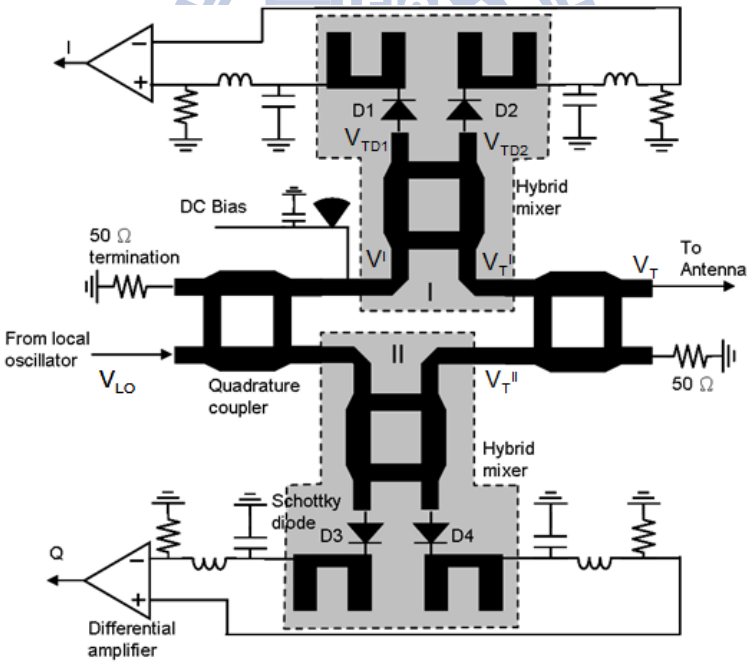

Figure 2.6 Schematic of the LO transmissive quadrature hybrid mixer.

Figure 2.6 illustrates the complete schematic of the proposed LO transmissive quadrature hybrid mixer, which consists of two hybrid mixers and two attached 90° branch-line couplers. Each hybrid mixer is composed of a 90° branch-line coupler, two

Schottky diodes, and followed be two LPFs. Let the signal from the LO be given by:

$$V_{LO} = A_{LO}\cos(\omega_T t) \tag{2-4}$$

where A_{LO} is the amplitude of the LO signal and ω_T the LO frequency (which is also the frequency of the transmitting signal). After passing through the first quadrature coupler and the 45° delay line, the signal, V^I, entering the upper hybrid mixer (mixer-I) can be expressed as:

$$V^I = \frac{A_{LO}}{\sqrt{2}}\cos\left(\omega_T t - \frac{5\pi}{4}\right) \tag{2-5}$$

This signal is then divided into two parts by the branch line coupler in the hybrid mixer and delivered to the two Schottky diodes D_1 and D_2, where these signals have the forms of:

$$V_{TD1} = \frac{A_{LO}}{2}\cos\left(\omega_T t + \frac{\pi}{4}\right) \tag{2-6}$$

$$V_{TD2} = \frac{A_{LO}}{2}\cos\left(\omega_T t - \frac{\pi}{4}\right) \tag{2-7}$$

The signal power here is used to drive for the mixer operation, after that, most power is reflected from the diodes with a large reflection coefficient α_D, and eventually, the reflected powers combine at the RF port of the hybrid mixer-I as:

$$V_T^I = \frac{A_{LO}}{\sqrt{2}}\alpha_D\cos\left(\omega_T t - \frac{3\pi}{4}\right) \tag{2-8}$$

In the mean time, the LO signal also enters the lower hybrid mixer (mixer-II), resulting in a signal, V_T^{II}, from mixer-II as:

$$V_{\mathrm{T}}^{\mathrm{II}} = \frac{A_{\mathrm{LO}}}{\sqrt{2}} \alpha_{\mathrm{D}} \cos\left(\omega_{\mathrm{T}} t\right) \tag{2-9}$$

This output signal from mixer-II passes through the 45° delay line and then enters the second quadrature coupler. The LO signal passing through mixer-II combines with the signal from mixer-I at the antenna port of the second branch-line coupler. The combined transmitting signal at the antenna port is obtained as:

$$V_{\mathrm{T}} = A_{\mathrm{LO}} \alpha_{\mathrm{D}} \cos\left(\omega_{\mathrm{T}} t - \frac{5\pi}{4}\right) \tag{2-10}$$

It is seen that only the reflection loss ($1/\alpha_{\mathrm{D}}$) at the Schottky diodes contributes to the insertion loss of the transmitting signal from LO to antenna.

In the receiving path, the signal received by the antenna can be given by:

$$V_{\mathrm{R}} = A_{\mathrm{R}} \cos\left(\omega_{\mathrm{R}} t\right) \tag{2-11}$$

where A_{R} and ω_{R} are the amplitude and frequency of the signal received. After passing through the second branch-line coupler and entering hybrid mixer-I, the received signals at diodes D_1 and D_2 are given by:

$$V_{\mathrm{RD1}} = \frac{A_{\mathrm{R}}}{2} \cos\left(\omega_{\mathrm{R}} t - \frac{3\pi}{2}\right) \tag{2-12}$$

$$V_{\mathrm{RD2}} = \frac{A_{\mathrm{R}}}{2} \cos\left(\omega_{\mathrm{R}} t - \pi\right) \tag{2-13}$$

These signals are mixed with the LO signals (2-6) and (2-7), respectively, leading to the output of fundamental harmonics obtained as:

$$V_{IF1} = \frac{A_R}{2} C_L \cos\left((\omega_T - \omega_R)t - \frac{\pi}{4} \right) \tag{2-14}$$

$$\begin{aligned} V_{IF2} &= \frac{A_R}{2} C_L \cos\left((\omega_T - \omega_R)t + \frac{3\pi}{4} \right) \\ &= -V_{IF1} \end{aligned} \tag{2-15}$$

where C_L is the conversion coefficient of the mixer diode, 1/ C_L is also expressed as the mixer conversion loss. The outputs at these IF port within a single hybrid mixer section are out of phase, therefore, a low-noise differential amplifier with gain of G_{diff} is used here to convert the differential signal into single-ended. The differential amplifier can also help to reject the common-mode noise which helps to improve the receiver sensitivity [33]. After this amplifier, the received IF signal at the in-phase port (I port) has the following form:

$$V_{IF}^{I} = A_R G_{diff} C_L \cos\left((\omega_T - \omega_R)t - \frac{\pi}{4} \right) \tag{2-16}$$

Similarly, the IF signal at the quadrature-phase port (Q port) can be derived as

$$V_{IF}^{Q} = A_R G_{diff} C_L \cos\left((\omega_T - \omega_R)t + \frac{\pi}{4} \right) \tag{2-17}$$

Apparently, the IF outputs at both I and Q ports of the mixer are equal amplitude and 90° difference in phase.

2.3 The full-duplex bi-directional amplifier

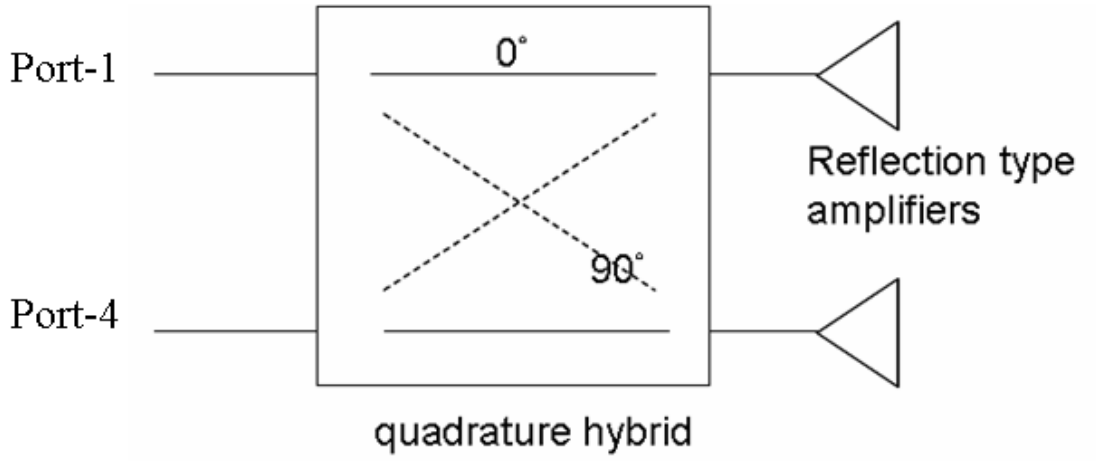

Figure 2.7 The block diagram of the full-duplex bi-directional amplifier.

Figure 2.7 shows the proposed configuration of the full-duplex bi-directional amplifier, which contains two reflection-type amplifiers and a quadrature hybrid. The amplifiers are connected to the output ports 2 and 3 of the hybrid, respectively. The input and isolating ports of the hybrid serve as the input / output ports of the bi-directional amplifier.

The scattered wave coming out from the quadrature hybrid is $\overline{V^-} = \left[V_1^-, V_2^-, V_3^-, V_4^-\right]^T$, where the scattering matrix of the quadrature hybrid is [34]:

$$[S] = \frac{-1}{\sqrt{2}} \begin{bmatrix} 0 & j & 1 & 0 \\ j & 0 & 0 & 1 \\ 1 & 0 & 0 & j \\ 0 & 1 & j & 0 \end{bmatrix} \tag{2-18}$$

Let only the port-1 have wave incident and port-4 be terminated. The scattering wave at port-2 and 3 are expressed as:

$$V_2^- = \frac{-j}{\sqrt{2}} V_1^+, \quad V_3^- = \frac{-1}{\sqrt{2}} V_1^+ \tag{2-19}$$

Noting that the reflection-type amplifier with gain G at port-2 and -3 ($V_2^+ = GV_2^-$, $V_3^+ = GV_3^-$), the outputs at port-1 and 4 are then obtained:

$$V_1^- = 0, \quad V_4^- = jGV_1^+ \tag{2-20}$$

It is seen that no power is reflected back to the input port and that the transmission gain $\left|V_4^- / V_1^+\right|$ is the same as the gain G of the reflection-type amplifiers. Owing to the symmetric architecture, the same result can also be derived when wave is excited from port-4 to port-1.

In practice, the reflection-type amplifiers will have small performance deviation, which maybe cause by the mismatch of active components used in the reflection-type amplifiers. The slight gain deviation ΔG causes the reflection coefficient and transmission gain becomes:

$$\left|\frac{V_{1-}}{V_1^+}\right| = \frac{\Delta G}{2} \tag{2-21}$$

and

$$\left|\frac{V_{4-}}{V_1^+}\right| = G\left(1 + \frac{\Delta G}{2G}\right) \tag{2-22}$$

The same results can be obtained when wave is coming from the port-4. It is seen that the gain deviation mainly contributes to the reflection coefficient, only little change in the transmission gain.

Chapter 3 Design and Measurement of a Doppler Radar using the LO Transmissive Quadrature Hybrid Mixer

In this chapter, a 10.5 GHz Doppler radar transceiver using the LO transmissive quadrature hybrid mixer is presented. The new transceiver architecture is proposed with higher LO power usage efficiency and simpler circuit complexity. The operation principle of the new LO transmissive quadrature hybrid mixer was illustrated in chapter-2. The design of the proposed quadrature hybrid mixer and the other components which compose a complete radar transceiver are illustrated. The performance of the integrated radar transceiver is shown. In the following, another single antenna radar transceiver using the conventional quadrature mixer is fabricated for comparison. An experiment shows the received power is improved in new LO transmissive quadrature hybrid mixer architecture. The implemented radar is also tested on the road side to detect the vehicle flow and their relative speed.

3.1 Development of the 10.5 GHz quadrature radar transceiver

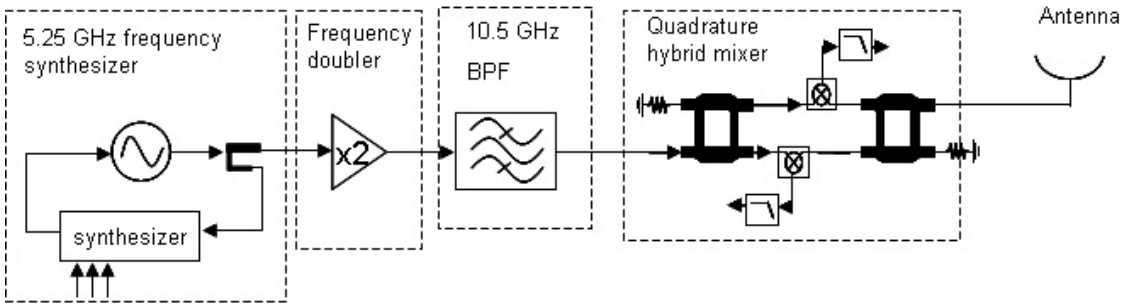

Figure 3.1 Block diagram of the single antenna radar transceiver using proposed LO transmissive quadrature hybrid mixer.

Figure 3.1 illustrates the building block of the proposed radar transceiver front-end using the LO transmissive quadrature hybrid mixer. The transceiver is composed of a 5.25 GHz frequency synthesizer, a frequency doubler, a 10.5 GHz Band-Pass Filter, along with a LO transmissive quadrature hybrid mixer. A stable signal source is vital for the radar application. In this study, the frequency synthesizer architecture is adopted to mend the frequency deviation due to temperature difference or component performance decay. A Defected-Ground-Structure (DGS) is used in the VCO design to provide better phase noise performance. An active frequency doubler is designed to supply the required 10.5 GHz signal from doubling the 5.25 GHz input signal. Instead of using the passive design, the active frequency doubler is chosen for two reasons. First of all, to minimize the component cost, the frequency doubler itself provides sufficient output power for short-range applications, thus the output amplifier not required. Furthermore, the output power can be adjusted on demand by changing the bias voltage to the frequency doubler. A 10.5 GHz BPF is connected to the output of frequency doubler. The 10.5 GHz BPF is used to filter out the unwanted harmonic signals produced by the frequency doubler. The BPF helps to minimize the harmonic signal emission, and also improves the conversion efficiency of frequency doubler. The LO transmissive quadrature hybrid mixer is connected between the BPF and antenna. The mixer performs the function to down-convert the received radar signal and delivers the local signal power to the antenna as well.

3.1.1 The LO transmissive quadrature hybrid mixer

A 10.5 GHz quadrature hybrid mixer is developed at 10.5 GHz, which is composed of branch-line couplers, delay lines, and LO transparent hybrid mixer. The couplers and delay lines are designed using a 2.5-D EM simulator IE3D [35]. The developed quadrature hybrid mixer is implemented on a RO4003 substrate with a dielectric

constant 3.38 and thickness 20-mil. The M/A-COM MA4E2054 Schottky diode is selected as the mixer diode in this study. The simulation of large signal is performed using the Ansoft Microwave Office [36]. Figure 3.2 gives SPICE model of the MA4E2054 Schottky diode and equivalent circuit model of the SOD-323 package.

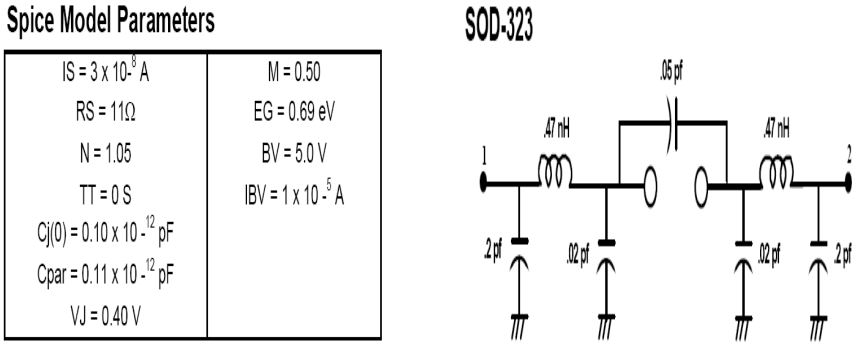

(a) (b)

Figure 3.2 The (a) SPICE model and (b) equivalent circuit model of MA4E2054-1141T Schottky diode and SOD-323 package.

Table 3-1 The simulated input impedances of a single diode section versus input power level.

Power (dBm)	Real(Z11)	Imag(Z11)
-20	0.0264209	-50.9851
-16	0.0417531	-50.9851
-12	0.144746	-50.9849
-8	1.09514	-50.9392
-4	3.5659	-50.53
0	6.05	-50.2329
4	8.03959	-50.0439
8	9.48108	-49.8283
12	10.4763	-49.5965
16	22.3281	-47.9826
20	59.5466	-54.4993

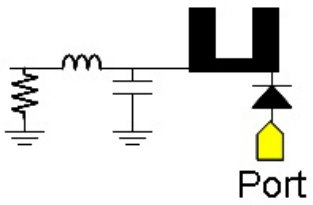

Table 3-1 gives the simulation result of the diode input impedance versus the input signal strength. In this simulation, a 10.5 GHz single-tone large signal is excited directly into the anode pin of the Schottky diode, where the cathode pin of the diode is connected to a quarter wavelength open stub. The quarter wave open stub provides a virtual ground

to the RF signal. The residual LC components are used to filter out the other harmonic signals to the IF output, which shows no affection to the input impedance. From this result, the input impedance at the excitation level of 4 dBm is 8–j50 ohm. The imaginary part of the input impedance versus input power level does not change observably, however, the real part varies a lot. Figure 3.3 shows the Smith chart of simulated input impedance versus input power level at 10.5 GHz. From this result, the diode acts like a capacitor in low power condition.

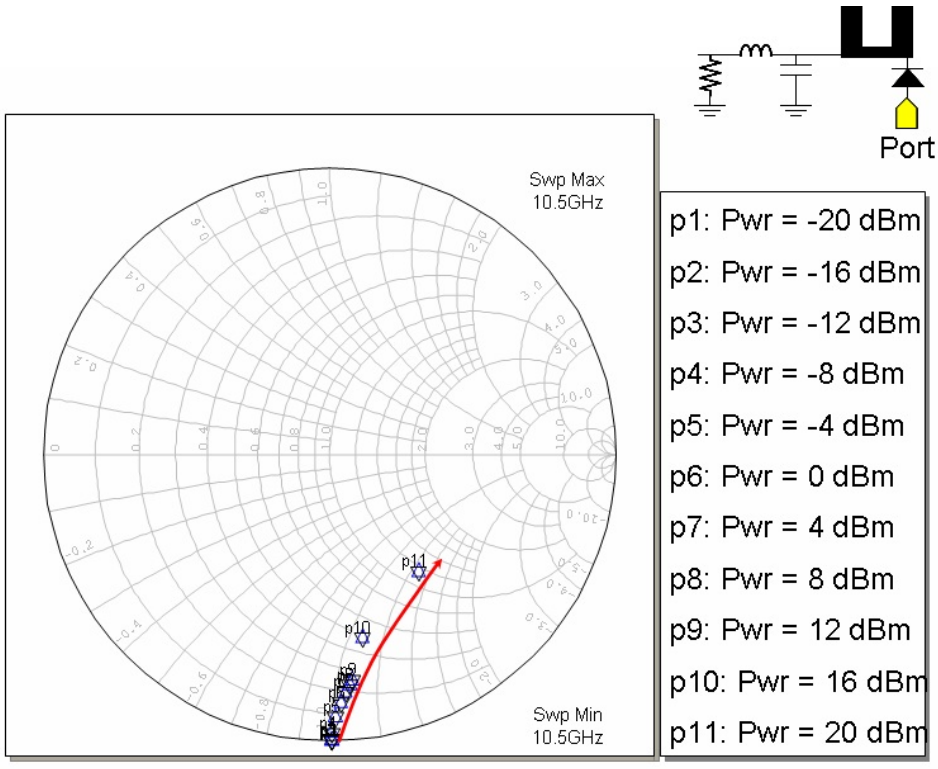

Figure 3.3 Smith chart of the simulated input impedances of a single diode section at 10.5 GHz.

Figure 3.4 illustrates how the mixer diode consume the LO power in terms of reflection coefficient. From this result, all the LO power are reflected when power level lower than -10 dBm, mixing signal fails at this condition because the voltage swing does not bigger than the diode barrier voltage. As the power increase, the reflection ratio reduces. When the input power level exceeds 12 dBm, the reflection coefficient drops rapidly, the lost power has been converted into higher order harmonic signals. This is a kind of waste because the other harmonic signals are useless in the mixer application.

From this result, the input power range from 0 to 10 dBm is considered suitable for the mixer design for acceptable reflection coefficient and sufficient LO power do drive the mixer diodes.

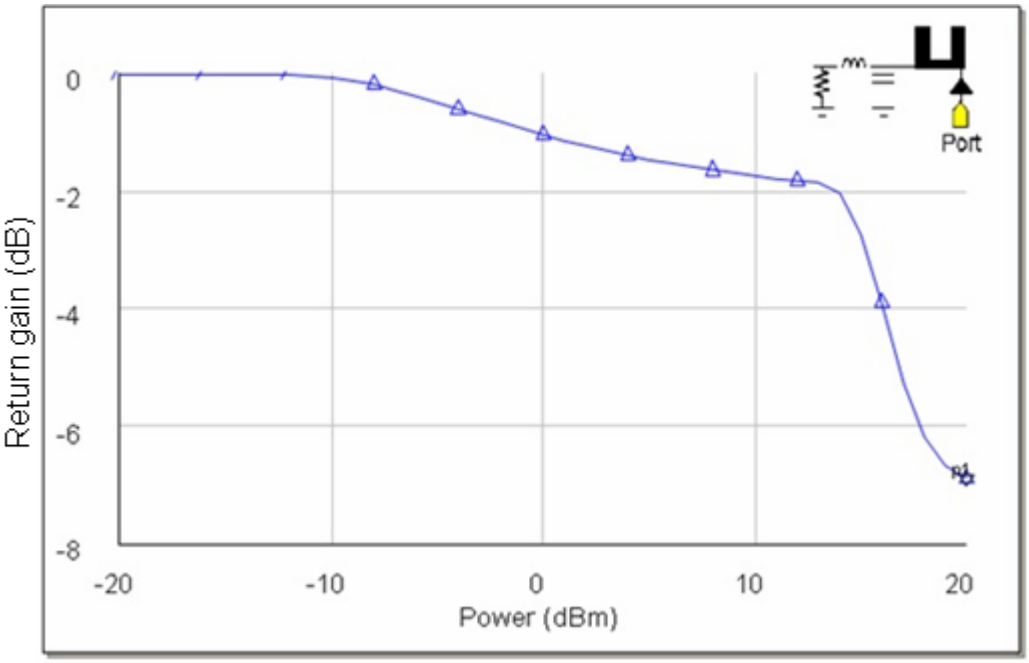

Figure 3.4 The simulated reflection coefficient of the LO power at 10.5 GHz.

In the hybrid mixer, the RF and LO signals are excited together to the anode pin of mixer diode. The RF signal is considered as a small signal, while the LO is large signal. A two-tone simulation is performed to the mixer diode section to estimate how the RF and LO signals affect each other. Table 3-2 gives simulation result of the two-tone simulation, where the LO signal is excited with a level of 4 dBm and the RF power level of -50 dBm. The input impedance of both LO and RF signal are obtained independently. There is no equipment can measure the two-tone input impedance because the frequency of these two signal are too close, only the simulation can observe the input impedances independently. Compare to the result shown in table 3-1, the input impedance of the LO signal does not change a lot when the RF signal excited. However, the result shows a significant change in the input impedance of the RF signal when LO is excited. The input impedance of RF

signal is 25 - j44.7 ohm, which means most of the RF signal is absorbed by the mixer diode.

Table 3-2 The simulated input impedances of a two-tone signal in a single diode section.

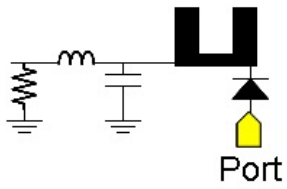

	LO (4 dBm)		RF (-50 dBm)	
Frequency (GHz)	Real(Z11)	Imag(Z11)	Real(Z11)	Imag(Z11)
9.5	6.40607	-59.0616	17.5876	-59.2154
9.6	6.06222	-58.4964	13.6039	-59.1284
9.7	5.26928	-57.7096	11.6874	-55.9261
9.8	4.83438	-55.3753	14.0298	-47.9696
9.9	5.20417	-52.8698	15.3677	-43.2896
10	6.16386	-51.6249	15.9798	-42.6678
10.1	7.0154	-51.6128	19.494	-43.1206
10.2	7.408	-51.0057	21.5865	-41.7064
10.3	7.73401	-50.7146	23.2908	-41.2323
10.4	7.93361	-50.5076	24.3385	-42.4038
10.5	8.04945	-50.2274	25.0287	-44.6653
10.6	8.10642	-49.9168	25.3524	-47.1026
10.7	8.11542	-49.606	24.9285	-49.1719
10.8	8.072	-49.3234	23.5056	-50.8242
10.9	7.95704	-49.1007	20.6739	-52.2541
11	7.38087	-49.3022	14.7023	-49.3984
11.1	7.59029	-47.9491	18.6135	-50.5851
11.2	7.43415	-47.6193	15.8338	-50.6125
11.3	7.17505	-47.165	14.0499	-50.2882
11.4	6.90211	-46.5838	13.1076	-49.541
11.5	6.6833	-45.8373	13.2995	-48.2711

Figure 3.5 shows another simulated reflection coefficients of both LO and RF signals in the mixer diode section. The LO and RF are excited at a level of 10 and -50 dBm, respectively, with a relative frequency difference of 1 MHz. From this result, the return loss of the LO signal is lower than 2 dB around the designed frequency range. Only small percentage of RF signal is reflected by the diode.

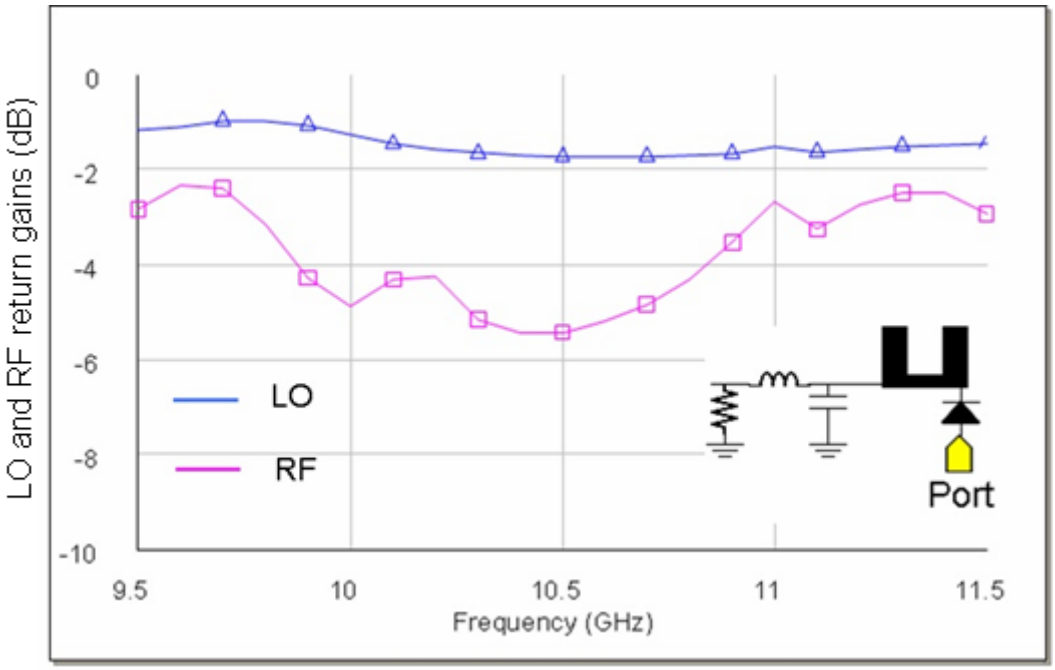

Figure 3.5 The simulated reflection coefficient of LO and RF signals.

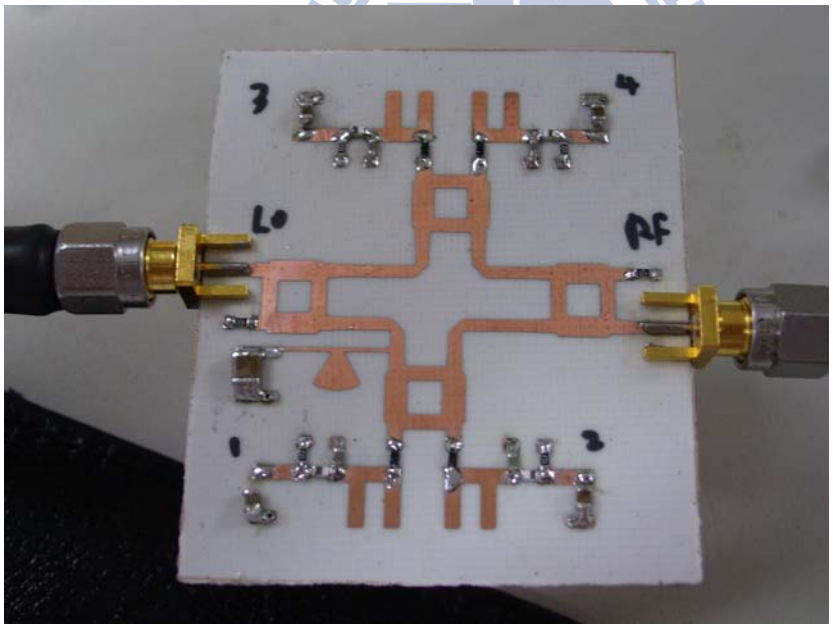

Figure 3.6 Photograph of the LO transmissive quadrature hybrid mixer.

Figure 3.6 shows a photograph of the implemented LO transmissive quadrature hybrid mixer. Four branch-lines along with four Schottky diodes compose the quadrature hybrid mixer. An external voltage bias network is added, which gives a feasibility to optimize the performance according to different LO power level. The additional bias is

necessary because the change in the transmitting signal power affects the conversion efficiency significantly.

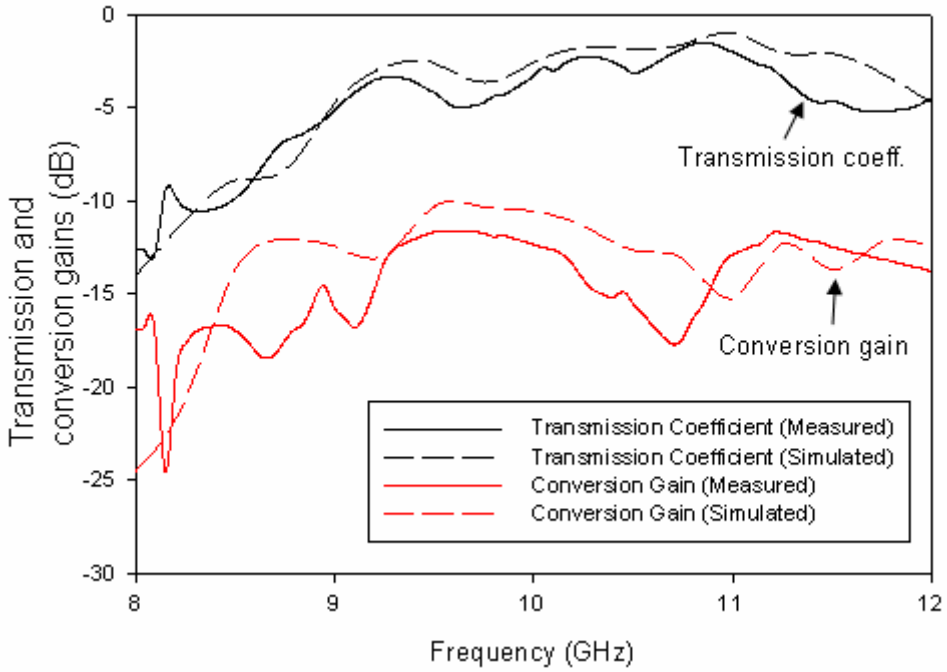

Figure 3.7 Simulated and measured conversion gain of the hybrid mixer and the insertion loss from LO to antenna of the proposed quadrature hybrid mixer.

Figure 3.7 illustrates the measured frequency response of the implemented quadrature hybrid mixer without bias voltage. In this measurement, the insertion loss (includes the reflection loss $1/\alpha_D$ from diode and the overall circuit losses) from LO to antenna, and the conversion loss (1/ C_L) of the quadrature hybrid mixer are shown. This experiment is executed with an LO power at 10 dBm. Considering that the non-linear characteristic should generate a lot of harmonic signals, these results were measured by a spectrum analyzer. Around the operating point at 10.5 GHz, the mixer shows a conversion loss of 15.5 dB from RF to the I-channel, the insertion loss of 3.1 dB from the signal source to the antenna, and return loss better than 15 dB which covers the range from 9.8 to 11.2 GHz. According to this result, the proposed mixer takes approximate half of the transmitting power to drive the mixer diodes and leaves the rest half power to the antenna

port. The difference between the simulated and measured ones are caused by the variation of each diode, this unbalance characteristic will slightly deteriorate the mixer conversion and insertion performance. The measured result also shows most of the LO power is reflected by the diode. It shows a good agreement with previous simulation result at single diode stage.

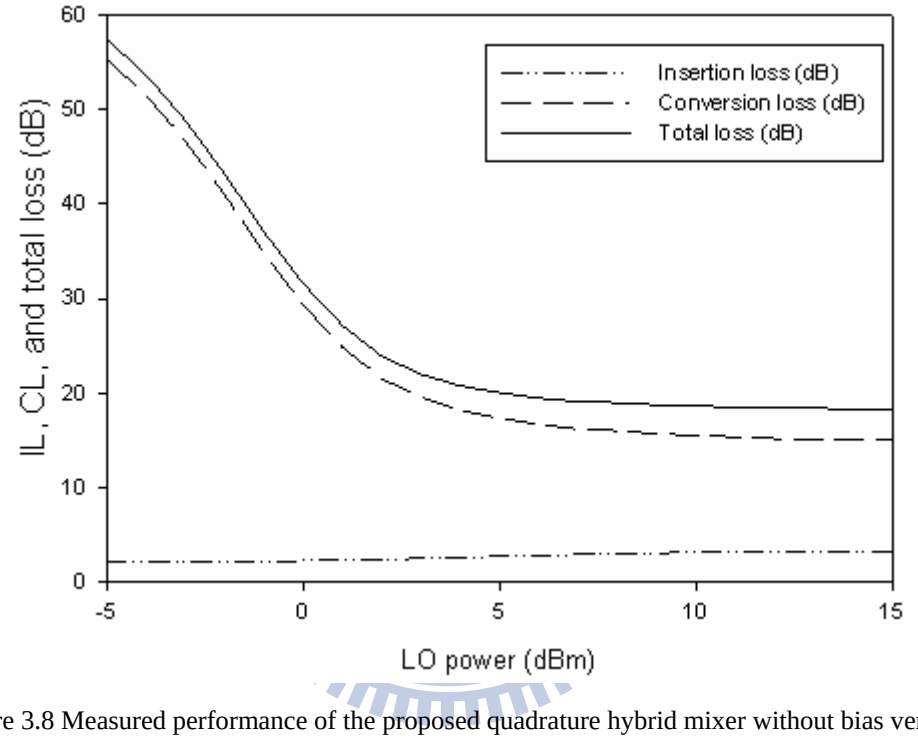

Figure 3.8 Measured performance of the proposed quadrature hybrid mixer without bias versus LO power level.

In the applications like automotive radars, biological sensors, the radars need to be operated under low LO power condition. The performance versus different LO power level is considered. The result illustrated in figure 3.8 gives the insertion loss, conversion loss, and the total loss, versus the LO power level. No bias voltage is applied to the mixer in this measurement. It is observed that, the conversion loss for LO power lower than 0 dBm is extremely high. As the power increases, the conversion loss becomes better, and finally saturates at 15 dB when the LO power is higher than 10 dBm. While only slight insertion loss regression when the LO power increases. In the

single antenna radar architecture, the LO signal leakage to the RF port is used as the interrogating signal of the radar. Therefore, a parameter called the total loss, which is defined as the summation of the conversion loss and insertion loss, is recommended. The total loss shows how many loss contributed by the transceiver itself in both transmitting and receiving path, which provides a better way to estimate the how efficient the LO power is been used in a low power radar system. The total loss in the proposed architecture saturates to 18.2 dB when LO comes more than 10 dBm. An external bias voltage is added in this mixer to enhance conversion efficiency during low LO power level condition. Adding bias voltage to the mixer diode is helpful to lower the barrier-voltage, thus it helps to improve the performance in low power condition [37]. The four diodes within the quadrature hybrid mixer are placed in parallel, therefore these diodes can be biased using a single bias network.

Figure 3.9 gives a simulated transmission and conversion gain of the LO transmissive quadrature hybrid mixer performance with additional bias voltage applied when the LO power is 0 dBm.

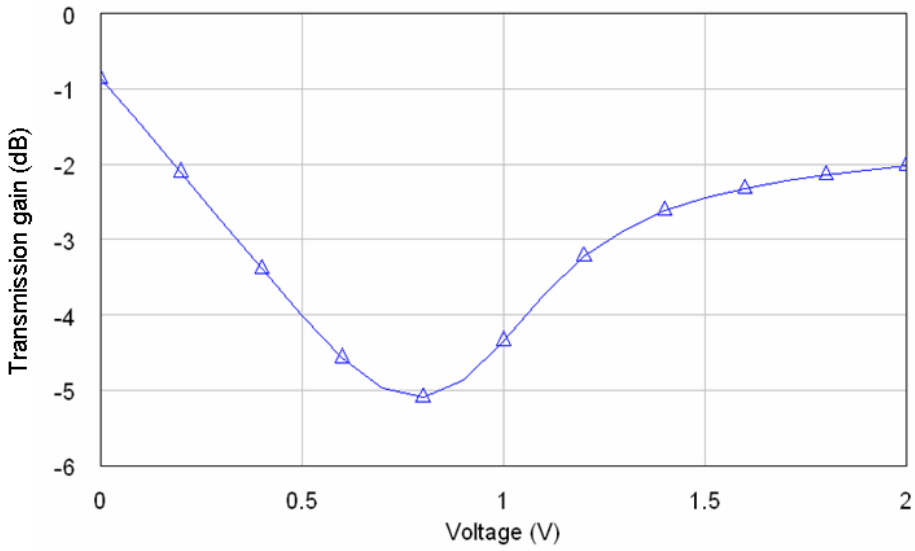

(a)

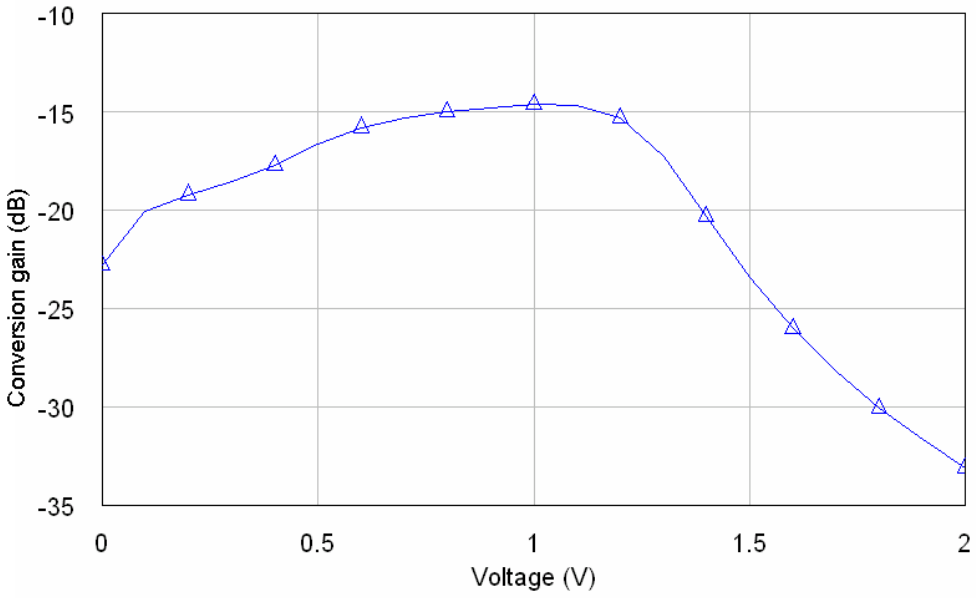

(b)

Figure 3.9 Simulation results of the (a) transmission gain and (b) conversion gain of the quadrature hybrid mixer with LO power 0 dBm.

Table 3-3 Measured quadrature hybrid mixer performance versus bias voltage.

The Summary of I/Q Hybrid Mixer measurement results												
LO Power	Loss (dB)	DC Bias (V)										
		0	0.2	0.4	0.6	0.8	1	1.2	1.4	1.6	1.8	2
-4	Insertion Loss	2.15	2.83	3.7	3.12	2.6	2.28	2.1	1.93	1.83	1.76	1.77
	Conversion Loss	54.5	21	17.67	18.5	22.17	26.83	31.17	34.83	38.33	40.83	43.67
	Total Loss	56.65	23.83	21.37	21.62	24.77	29.11	33.27	36.76	40.16	42.59	45.44
-2	Insertion Loss	2.18	2.93	3.67	3.26	2.66	2.31	2.12	1.94	1.83	1.76	1.76
	Conversion Loss	44	20	17.17	17.33	19.33	23.5	27.83	31.83	35.17	38.17	40.83
	Total Loss	46.18	22.93	20.84	20.59	21.99	25.81	29.95	33.77	37	39.93	42.59
0	Insertion Loss	2.25	3.03	3.64	3.37	2.78	2.37	2.16	2.09	1.85	1.79	1.82
	Conversion Loss	32.33	19.17	17	16.83	17.5	20	23.83	28	31.83	34.83	37.67
	Total Loss	34.58	22.2	20.64	20.2	20.28	22.37	25.99	30.09	33.68	36.62	39.49
2	Insertion Loss	2.39	3.14	3.61	3.51	2.96	2.48	2.23	2.12	1.89	1.81	1.84
	Conversion Loss	24.5	18.67	17	16.83	16.5	17.5	19.67	23.33	27.5	31	34.67
	Total Loss	26.89	21.81	20.61	20.34	19.46	19.98	21.9	25.45	29.39	32.81	36.51
4	Insertion Loss	2.58	3.23	3.59	3.59	3.17	2.65	2.35	2.18	1.93	1.83	1.82
	Conversion Loss	21.17	18.17	17.17	16.83	16.33	16.33	17.17	18.83	22	25.67	29.5
	Total Loss	23.75	21.4	20.76	20.42	19.5	18.98	19.52	21.01	23.93	27.5	31.32
6	Insertion Loss	2.8	3.29	3.56	3.63	3.36	2.88	2.55	2.29	2.05	1.9	1.87
	Conversion Loss	19.67	18	17	16.83	16.33	16.17	16.5	16.67	17.83	19.83	23
	Total Loss	22.47	21.29	20.56	20.46	19.69	19.05	19.05	18.96	19.88	21.73	24.87
8	Insertion Loss	2.97	3.34	3.55	3.63	3.54	3.1	2.77	2.5	2.23	2.05	2
	Conversion Loss	19	17.83	17	16.83	16.5	16.17	16.17	16.17	16.33	16.83	18
	Total Loss	21.97	21.17	20.55	20.46	20.04	19.27	18.94	18.67	18.56	18.88	20
10	Insertion Loss	3.12	3.39	3.53	3.64	3.54	3.3	3.03	2.75	2.48	2.26	2.18
	Conversion Loss	18.5	17.67	17	16.83	16.67	16.33	16.17	16.17	16.17	16	16.33
	Total Loss	21.62	21.06	20.53	20.47	20.21	19.63	19.2	18.92	18.65	18.26	18.51
12	Insertion Loss	3.21	3.41	3.51	3.63	3.59	3.42	3.25	3.03	2.78	2.54	2.45
	Conversion Loss	18.17	17.67	17.17	17	16.67	16.5	16.33	16.17	16.17	16	16
	Total Loss	21.38	21.08	20.68	20.63	20.26	19.92	19.58	19.2	18.95	18.54	18.45
14	Insertion Loss	3.27	3.4	3.48	3.58	3.61	3.48	3.38	3.23	3.04	2.84	2.76
	Conversion Loss	18	17.67	17.17	17.17	16.83	16.67	16.5	16.5	16.33	16.17	16
	Total Loss	21.27	21.07	20.65	20.75	20.44	20.15	19.88	19.73	19.37	19.01	18.76

From the simulation result, an optimized conversion loss is obtained when applying 1V to the mixer diodes, however, it costs a higher insertion loss to the LO signal. Table 3-3 gives a summary of the measurement results of the implemented quadrature hybrid mixer when applying bias voltage.

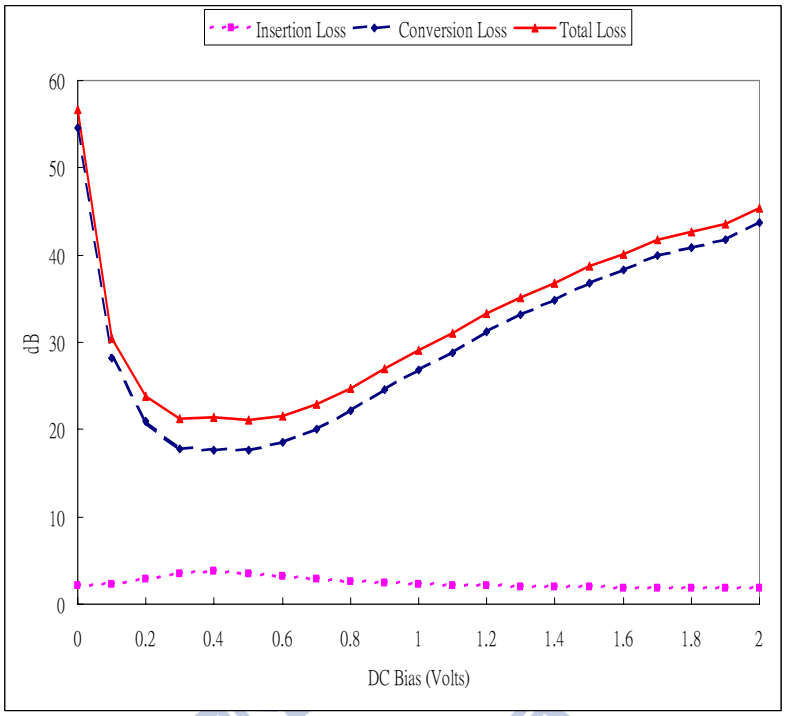

(a) LO = -4 dBm

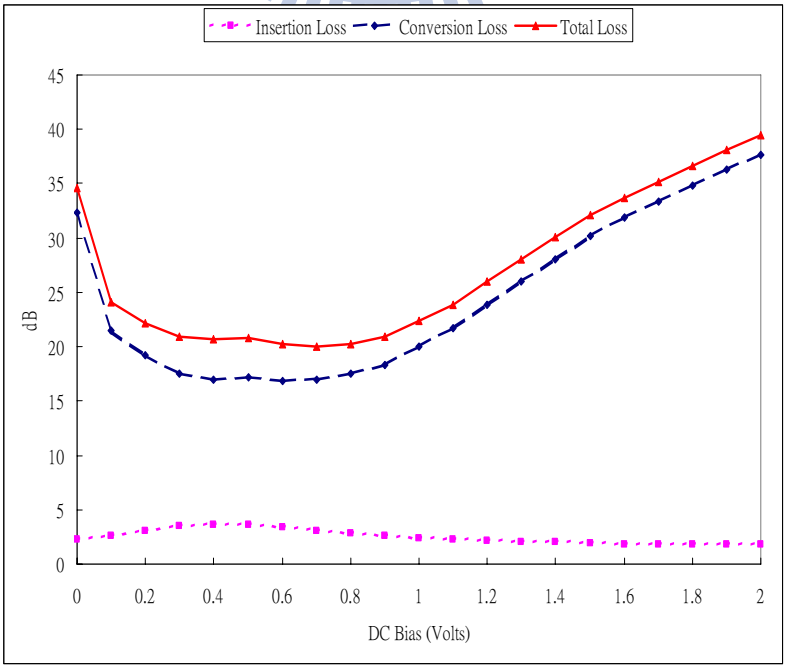

(b) LO = 0 dBm

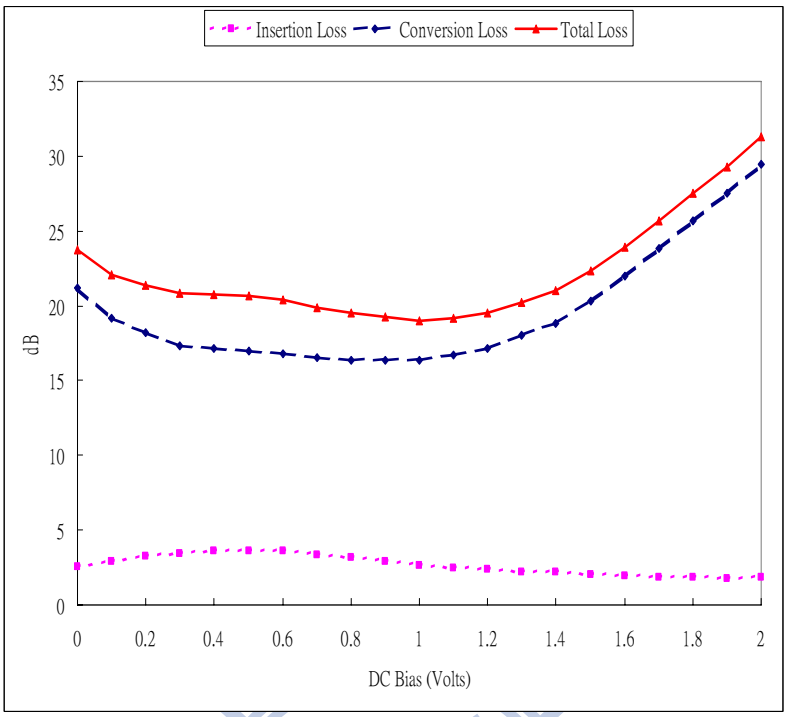

(c) LO = 4 dBm

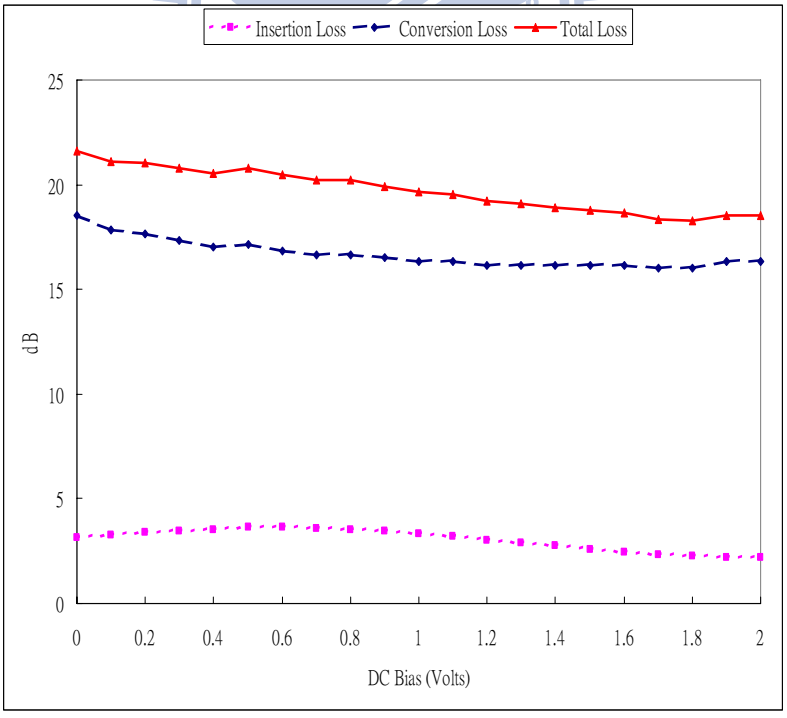

(d) LO = 10 dBm

Figure 3.10 Measured insertion loss, conversion loss, and total loss of the LO transmissive quadrature hybrid mixer versus bias voltage with different LO power levels.

Figure 3.10 show the transmission and conversion performances of the mixer versus the bias voltage when LO power is -4, 0, 4, and 10 dBm, respectively. When the LO power is 0 dBm (figure 3.10 (a)), the insertion loss changes only a little when bias voltage change from 0 to 2 V. The conversion loss reaches to the lowest when the bias voltage is 0.7 V. Higher conversion loss is obtained when the bias voltage becomes more than 1 V. Consequently, an optimized total loss can be obtained when the bias is 0.7 V. When the LO power is above 10 dBm (figure 3.10 (d)), the additional bias voltage does not affect the performance a lot. An optimum bias point can be obtained for each LO power level. Table 3-4 gives a summary of the optimized operating point for various LO power level.

Table 3-4 Summary of the optimized bias point and performance of the proposed quadrature hybrid mixer versus LO power level.

LO power (dBm)	Optimal DC bias (volts)	Conversion loss (dB)	Insertion loss (dB)	Total loss (dB)
-4	0.5	14.70	3.49	18.19
-2	0.6	14.33	3.26	17.59
0	0.7	14.00	3.05	17.05
2	0.8	13.50	2.96	16.46
4	1.0	13.33	2.65	15.98
6	1.3	13.33	2.38	15.71
8	1.5	13.17	2.34	15.51
10	1.8	13.00	2.26	15.26
12	1.9	12.83	2.83	15.66
14	2.0	13.00	2.76	15.76

The LO transmissive quadrature hybrid mixer is to be connected to the antenna directly, thus, the harmonic signals generated by the mixer itself may leak to the air through the antenna. Figure 3.11 shows a measurement result of the largest 2nd harmonic

power at the antenna port of the quadrature hybrid mixer with various input power level. The result shows a -26 dBm of 2nd harmonic power will be generated when the LO power is 10 dBm. As the LO power increases, the relative 2nd harmonic power also increases. The harmonic power is lower than -20 dBm during this experiment.

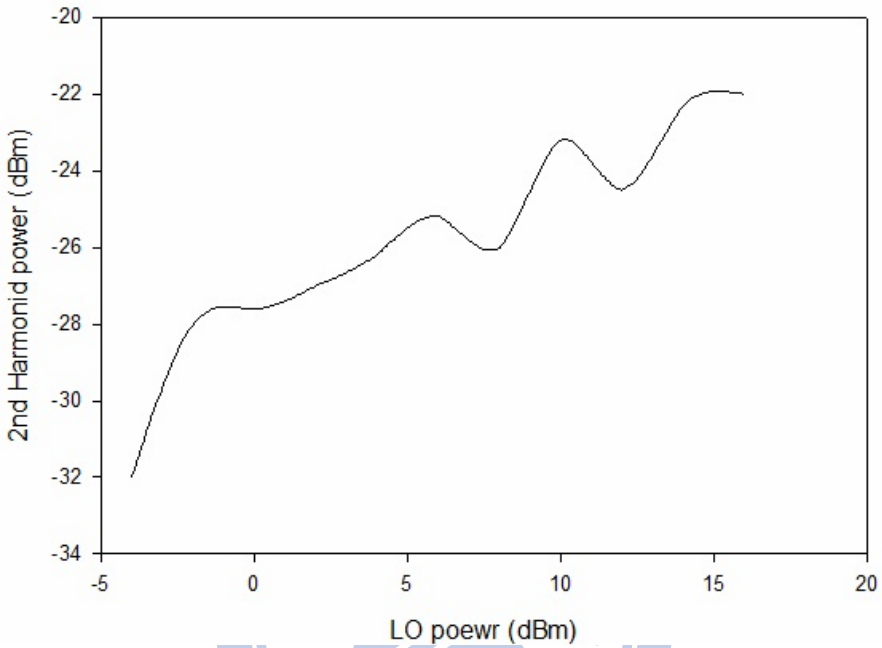

Figure 3.11 Measured largest 2nd harmonic signal strength.

3.1.2 The 5.25 GHz frequency synthesizer

Figure 3.12 shows a block diagram of a Phase-Lock Loop (PLL) frequency synthesizer.

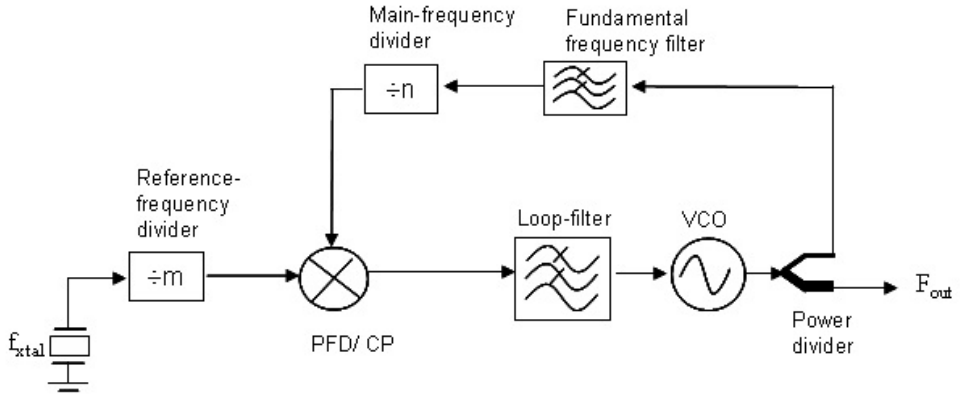

Figure 3.12 Block diagram of a typical PLL frequency synthesizer.

The frequency synthesizer is composed of a VCO, a power divider, fundamental

frequency filter, a main frequency divider, a precise reference frequency oscillator along with relative reference frequency divider, a Phase-Frequency Detector (PFD) integrated with a Charge-Pump (CP), and a loop-filter. The PFD detects the phase deviation between the divided main and reference signal source, and generates the relative feedback voltage to adjust the VCO output frequency. In this study, a commercial available frequency synthesize IC ADF4106 is selected, which integrates the main / reference frequency divider, PFD/CP together, and provides a bandwidth of 6 GHz. The divider ratio and CP current can be controlled by a 3-wire interface, which provides a feasibility to adjust the output frequency and PLL lock-in time according to the operating environment. The reference signal is driven by a temperature compensated crystal oscillator (TCXO) with output frequency of 40 MHz. The loop-filter is designed using typical LC circuitry with low pass characteristic and bandwidth of 2.5 KHz. The VCO design and frequency synthesizer integration are described in the following sections.

3.1.2.1 The 5.25 GHz VCO

The design of the VCO starts from the negative-impedance concept. As we know all the active devices are possible to be configured as a negative-impedance device, the Bipolar-Junction Transistor (BJT) is usually considered to have better phase noise performance than other devices. In this study, a general purposed BJT Philip BFG425W is used as the transistor in the VCO design. The transistor is biased at the condition of V_{CE} = 2V and I_C = 25 mA.

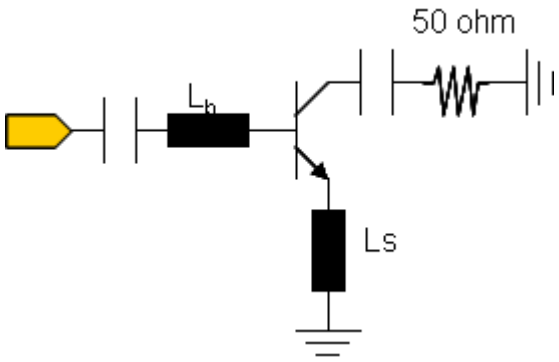

Figure 3.13 Schematic of the negative-impedance implementation using the BFG425W.

Figure 3.13 gives the negative-impedance circuit schematic using the BFG425W transistor. A short-stub is connected to the emitter port of the transistor, which provides an electric current path for the bias current to ground and a feedback path for the small signal to make the circuit unstable at the desired frequency band.

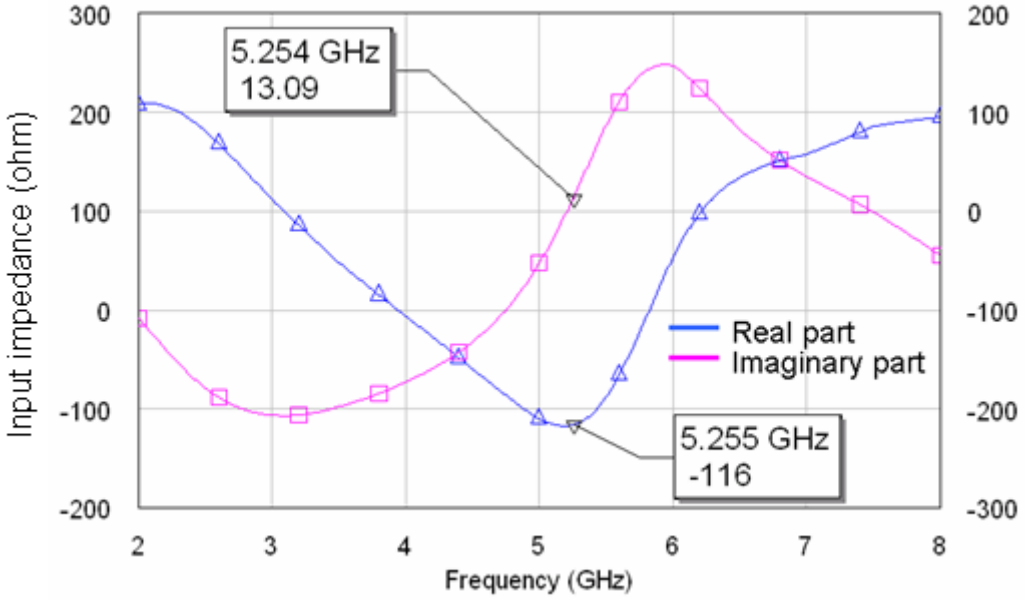

Figure 3.14 Simulation result of the negative-impedance section.

Figure 3.14 shows the simulation result of the negative impedance circuit using the BFG425W transistor. The left and right Y-axis gives the real part and imaginary part of the input impedance, respectively. As illustrated in the Fig 3.14, the negative-impedance is obtained from 4 to 5.8 GHz, with the lowest real part impedance of -116 ohm at 5.25GHz.

After the negative-impedance design, a corresponding resonator circuit is designed for the proper oscillating frequency. A resonator with high quality (Q)-factor is considered to have better phase noise performance in the VCO design. There are several ways to design a resonator with high Q-factor, however, they cost extra components or additional circuit area. In this study, the DGS architecture is adopted in the resonator design. The DGS is an etched area in the backside ground of a microstrip line. The disturbance on the ground plane can change characteristics of a transmission line such as line capacitance and inductance. The DGS provides a band-gap characteristic in the designed frequency with only one unit lattice, and results in better quality factor than other microstrip planar structures [38]. The DGS has been found in many filter applications and also been proven to improve the oscillator phase noise [39]. Fig. 3.15 (a) illustrates the two-section DGS used in this study. The equivalent circuit of the DGS can be modeled as a parallel LC resonant circuit in the series arm and two shunted capacitors, as shown in Fig. 3.15 (b). Each section of DGS behaves as a low-pass filter with an out-band transmission zero provided by the parallel LC pair. Figure 3.16 gives the measurement results of the two-section DGS designed with a cutoff frequency at 5.25 GHz. By fixing the cutoff frequency near the oscillation frequency, a high input phase slope can be obtained in the transmission coefficient, which implies high frequency stability in the oscillator design. It is also seen that the in-band insertion loss is better than 0.7 dB and a deep transmission zero at 8.3 GHz is produced.

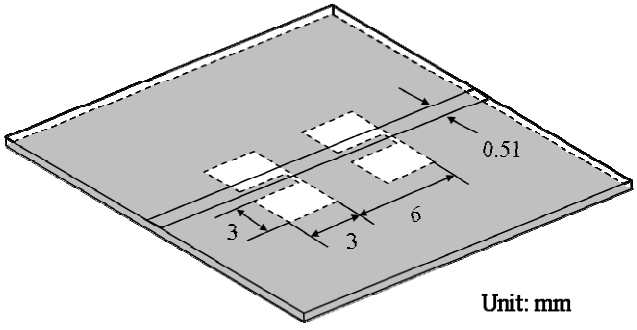

(a)

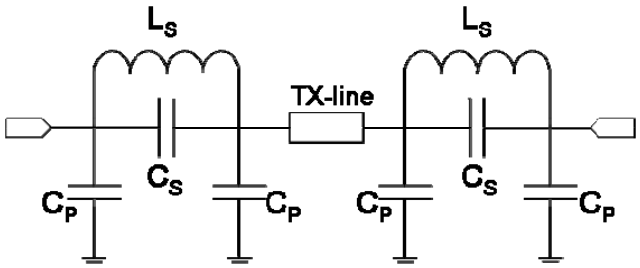

(b)

Figure 3.15 (a) A sketch of the two-section DGS and (b) the equivalent circuit model of the two-section DGS.

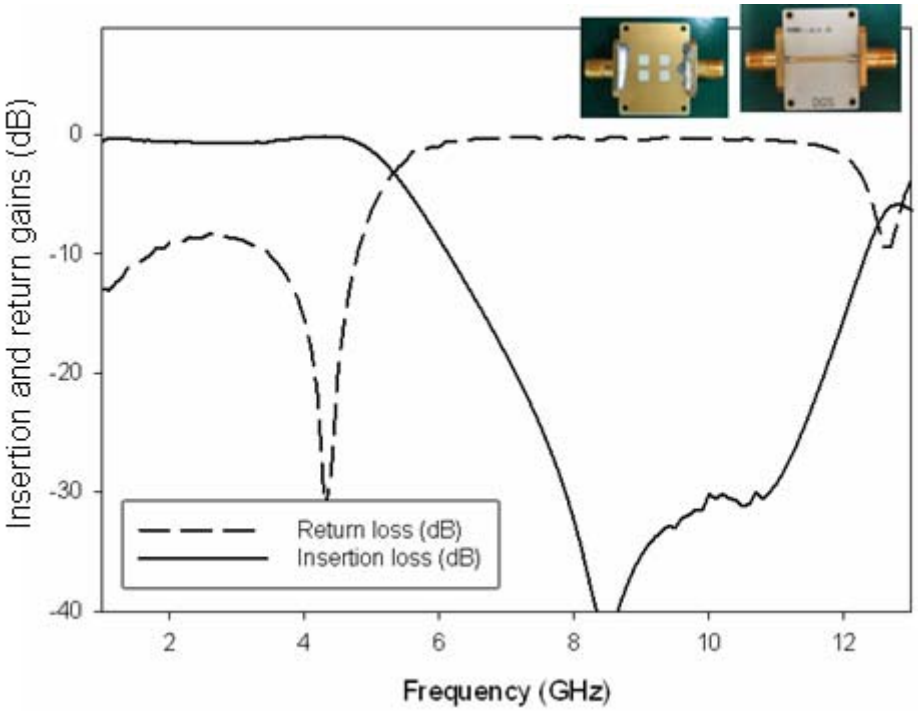

Figure 3.16 The measurement result of the two-section DGS.

The varactor diode is commonly used in the VCO design. Here we choose the TOSHIBA 1SV285 varactor diode as the voltage tuning device in this VCO. The 1SV285 has a C_{1V}/C_{4V} ratio of 2.3 which is suitable for the wide tuning range VCO design. Figure 3.17 gives a sketch of the circuit schematic of resonator design using the 1SV285 and DGS. Another design without the DGS is also implemented for comparison.

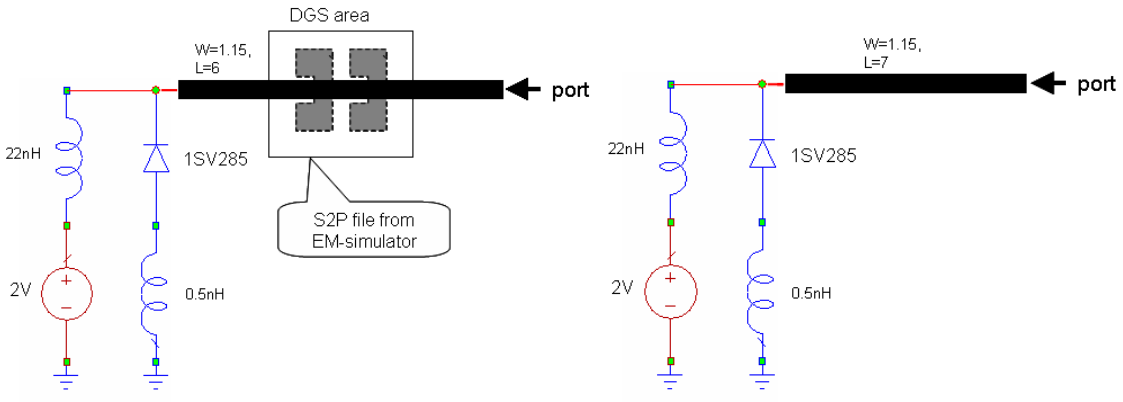

(a) (b)

Figure 3.17 Schematic of the resonator design (a) with DGS and (b) without DGS.

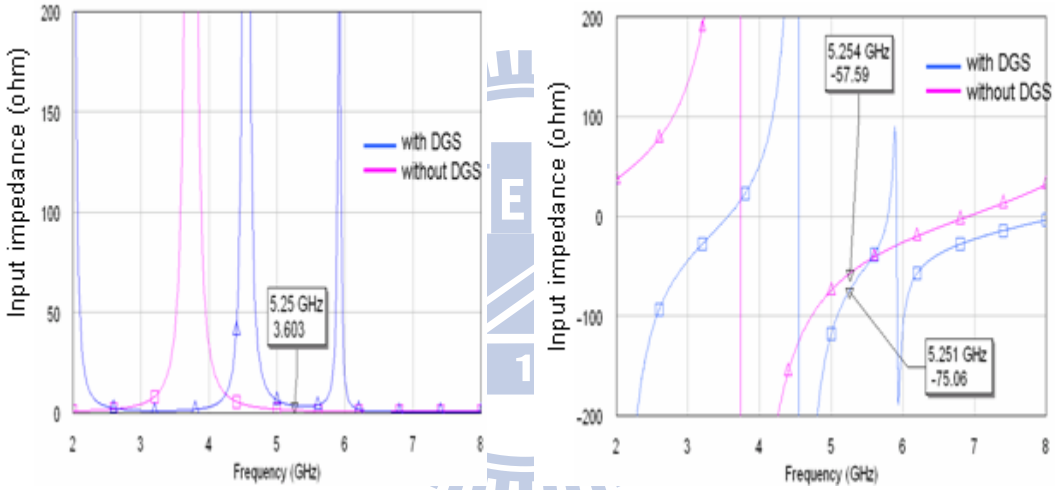

(a) real-part of input impedance (b) imaginary-part of input impedance

Figure 3.18 Simulation results of the resonator with and without DGS.

Figure 3.18 gives the simulation result of the resonator with and without DGS. As illustrated, the resonator with DGS has two poles in the real part of input impedance at 4.5 and 5.9 GHz. In the imaginary part, the slope of the input impedance with DGS is higher than that of the one without DGS, which means a better Q-factor is accomplished at the structure with DGS.

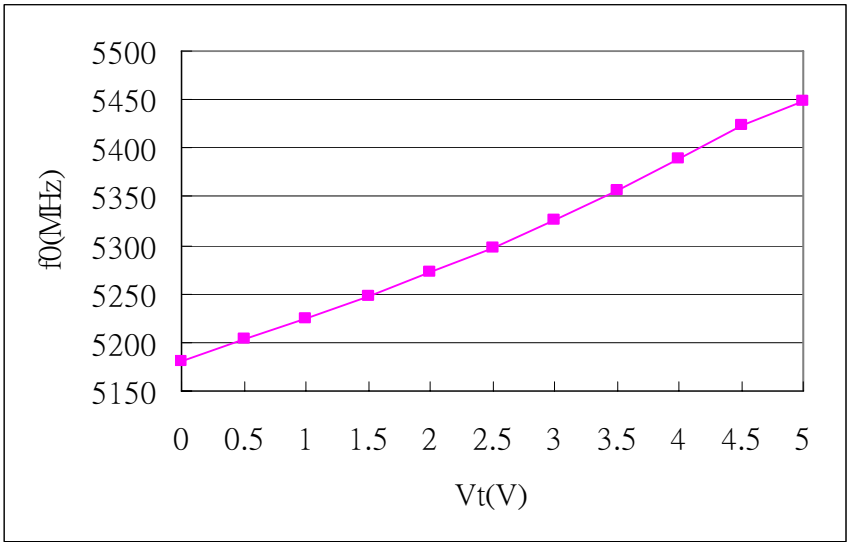

Figure 3.19 Measured output frequency versus the tuning voltage of the implemented VCO with DGS.

Figure 3.19 gives the measured output frequency and tuning voltage relationship of the implemented 5.25 GHz VCO. From this measurement, a tuning range of 275 MHz is achieved when tuning voltage comes from 0 to 5 volts. Table 3-5 gives a summarization of the VCO output power and frequency performance versus tuning voltage.

Table 3-5 Measured output performance of the implemented 5.25 GHz VCO.

Vt (V)	fo (MHz)	Output power (dBm)
0	5181	5.5
0.5	5204	5.5
1	5225	5.5
1.5	5248	5.67
2	5272	5.67
2.5	5297	5.67
3	5326	5.83
3.5	5357	6
4	5390	6.33
4.5	5423	6.5
5	5449	6.67

3.1.2.2 The 5.25 GHz PLL Frequency Synthesizer

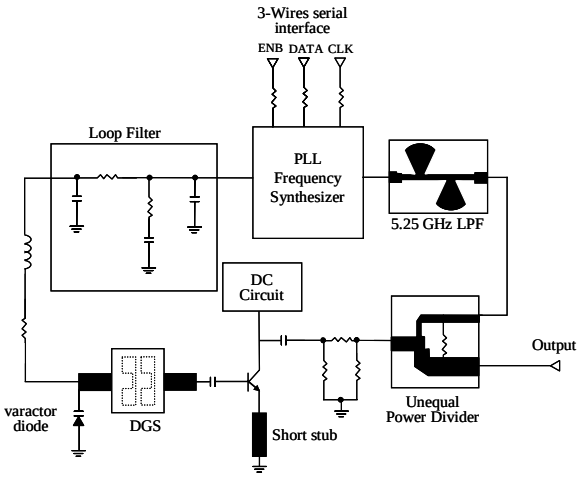

Figure 3.20 Schematic of the 5.25 GHz frequency synthesizer with two-section DGS.

The 5.25 GHz PLL frequency synthesizer is integrated as the schematic shown in figure 3.20. An unequal power divider and low-pass filter is also designed within the frequency synthesizer. The power divider splits a certain amount of power to drive the synthesizer IC without affecting the output power too much. In this study, the output power from the VCO is about 5 dBm, while the synthesizer IC requires -10 dBm at least. Theoretically, a power divider with dividing ratio of 3:1 is sufficient, however, considering the circuit loss and adding some power margin to the output power. The dividing ratio of unequal power divider is designed to be 2:1. Figure 3.21 shows the photograph of the implemented power divider and the measurement results. The fabricated one shows the S_{21} and S_{31} characteristics of 2.12dB and 7.01dB respectively.

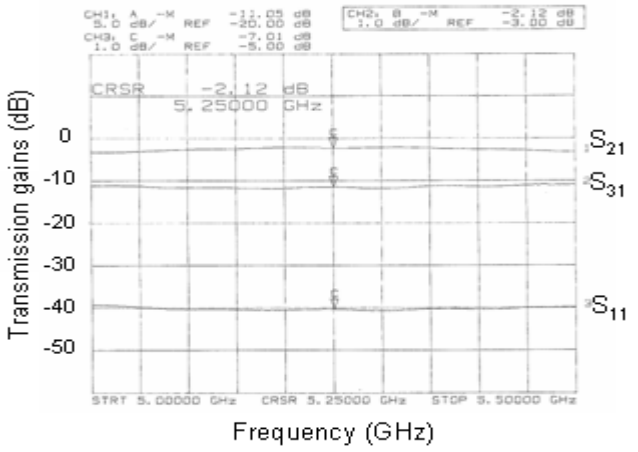

(a) (b)

Figure 3.21 (a) A photograph of the implemented unequal power divider and (b) measurement result.

Since the harmonic signals generated by the VCO may cause the synthesizer fail. A 5.25 GHz low-pass filter is required to obtain the pure fundamental signal at the RF input of synthesizer IC. The LPF is designed having high rejection ratio to the 2nd- and 3rd- harmonic frequencies. The cut-off frequency is designed at 5.25 GHz and a fan stub structure is adopted in this study to obtain good rejection ratio at the harmonic frequencies. Figure 3.22 shows the photograph of the fabricated 5.25 GHz LPF along with the measurement result. From this result, the 2nd and 3rd harmonic reject ratios are better than 30 and 25 dBc, respectively.

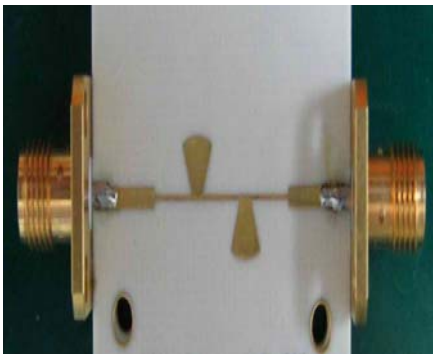

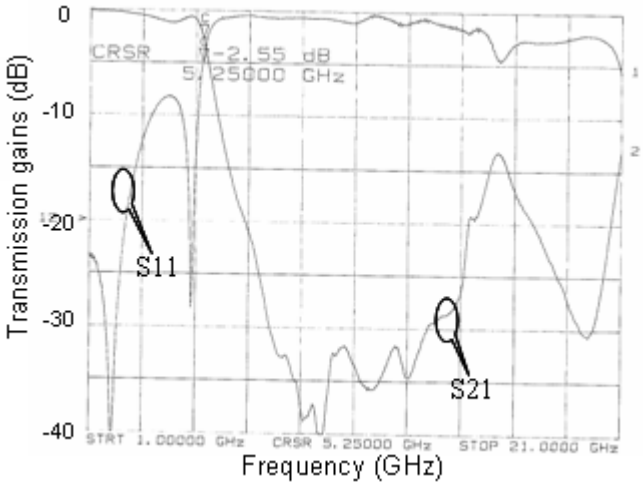

(a) (b)

Figure 3.22 (a) A photograph of the implemented 5.25 GHz low-pass filter and (b) measurement result.

Figure 3.23 gives a photograph of the integrated frequency synthesizer. All circuits are implemented on a substrate of RO-4003 with thickness 20-mil. The frequency synthesizer is composed of a 5.25 GHz VCO, a PLL synthesizer IC (ADF4106), a 40 MHz TCXO, a 5.25 GHz low-pass filter, and an unequal power divider. In the bottom side, an etched ground area which forms the DGS to provide better phase noise performance.

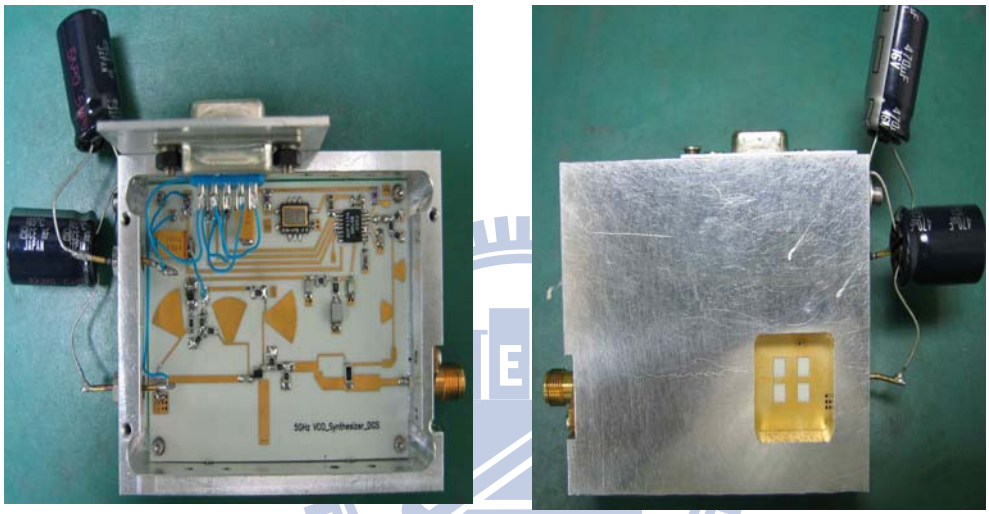

(a) top view (b) bottom view

Figure 3.23 Photographs of the 5.25 GHz PLL frequency synthesizer with DGS.

Figure 3.24 gives the measurement result of the integrated frequency synthesizer. The output power is 5.5 dBm at 5.25 GHz, and the maximal power deviation is lower than 1 dB when output frequency sweep from 5.2 to 5.4 GHz. Figure 3.24 (b) gives the measurement result of the harmonic spectrum, both the 2^{nd} and 3^{rd} harmonic are lower than -30 dBm.

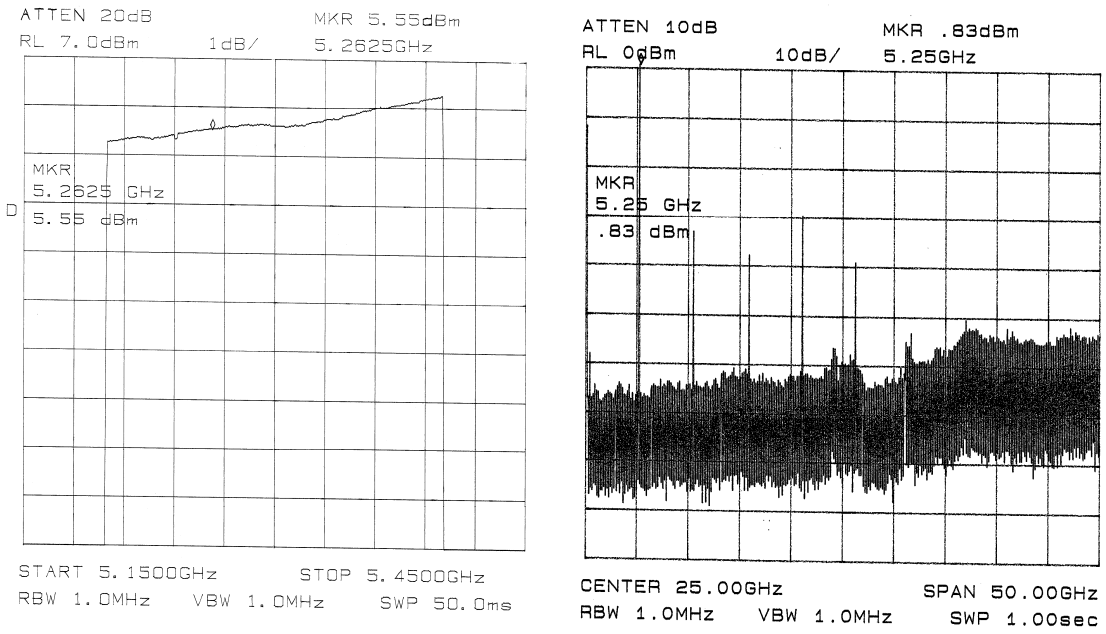

Figure 3.24 Measured (a) output power and (b) harmonic frequency spectrum of the 5.25 GHz frequency synthesizer.

Figure 3.25 shows the phase noise performance of the frequency synthesizer. The phase noises measurement result of 5.2, 5.25, 5.3, 5.35 GHz at offset frequency of 100 kHz are -110.2, -109.6, -109.5, and -105.2 dBc/Hz, respectively.

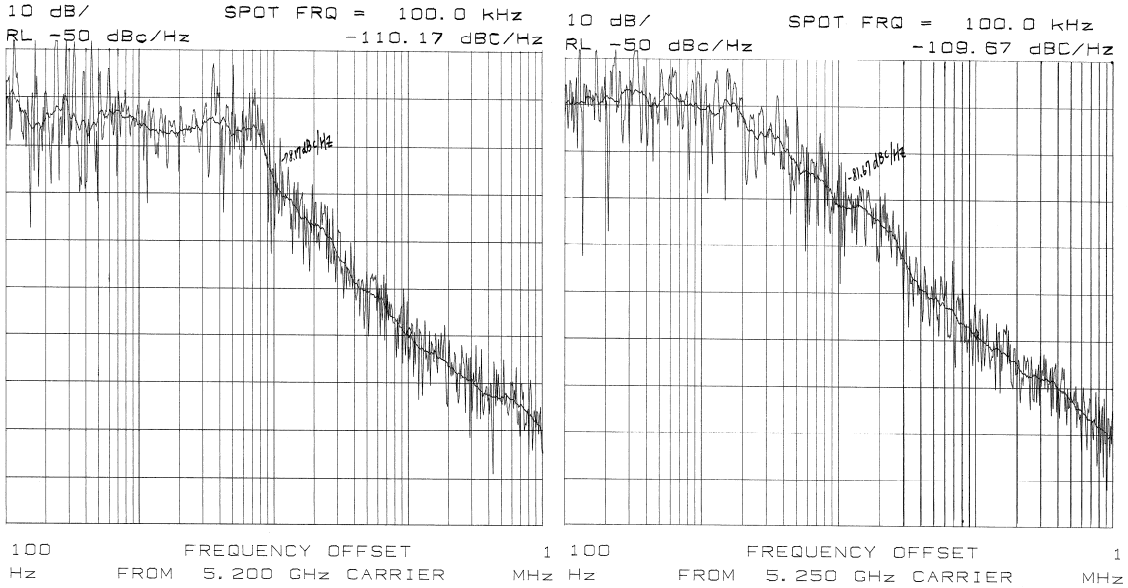

(a) f_0 = 5200MHz (b) f_0 = 5250MHz

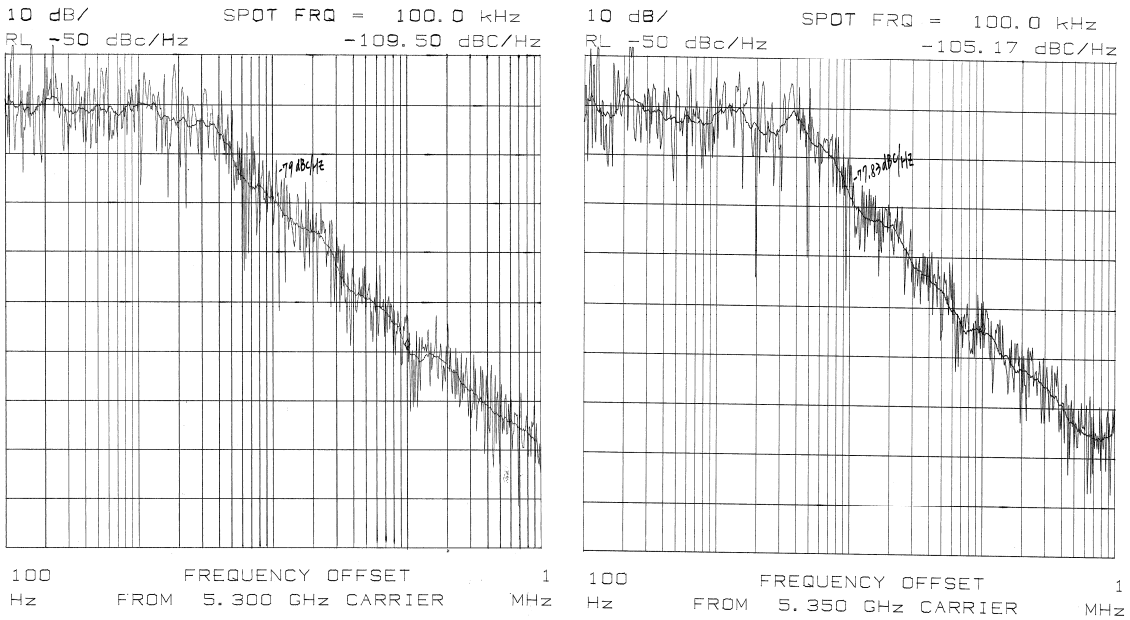

(c) f_0 = 5300MHz (d) f_0 = 5350MHz

Figure 3.25 Measured phase noise performance of the implemented 5.25 GHz frequency synthesizer.

3.1.3 The 5.25 GHz frequency doubler

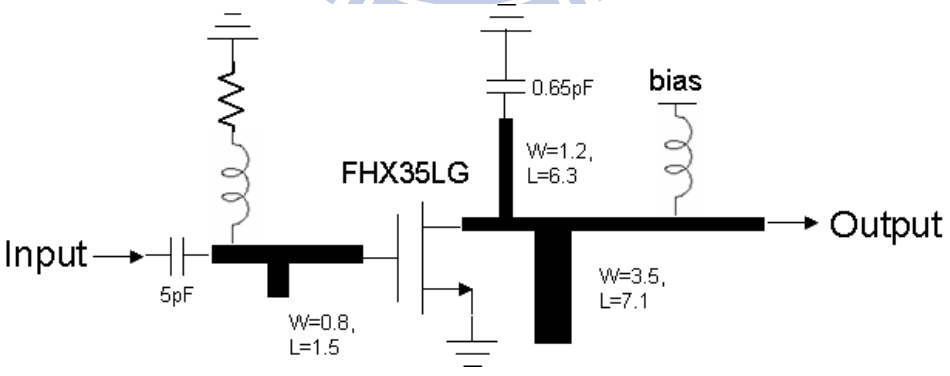

Figure 3.26 Circuit schematic diagram of the 5.25 GHz active frequency doubler.

The 5.25 GHz frequency doubler is used to convert the input of 5.25 GHz to the desired 10.5 GHz output. An active type frequency doubler is adopted in this thesis for the advantages of minimized component cost and feasibility to adjust the output power.

A general purposed FET transistor Fujitsu FHX35LG is used to design the active frequency doubler. Figure 3.26 illustrates the circuit schematic diagram of the active frequency doubler. The transistor is biased at V_{GS}= 0 V, and I_D= 25 mA. The transistors biased at zero V_{GS} usually have the best non-linear characteristic which is suitable for the doubler design. An open stub with length equivalent to a quarter of fundamental frequency wavelength is connected at the output stage of the frequency doubler as a frequency stopper to reflect the leaked 1st harmonic signal. The open stub reduces the fundamental signal leakage and also improves the conversion efficiency.

Figure 3.27 gives the simulation result of the 5.25 GHz frequency doubler when input power is 4 dBm. From the simulation results, the conversion gain at 5.25 GHz is 1 dB and the signal rejection ratio to the 1st harmonic is 19.6 dBc.

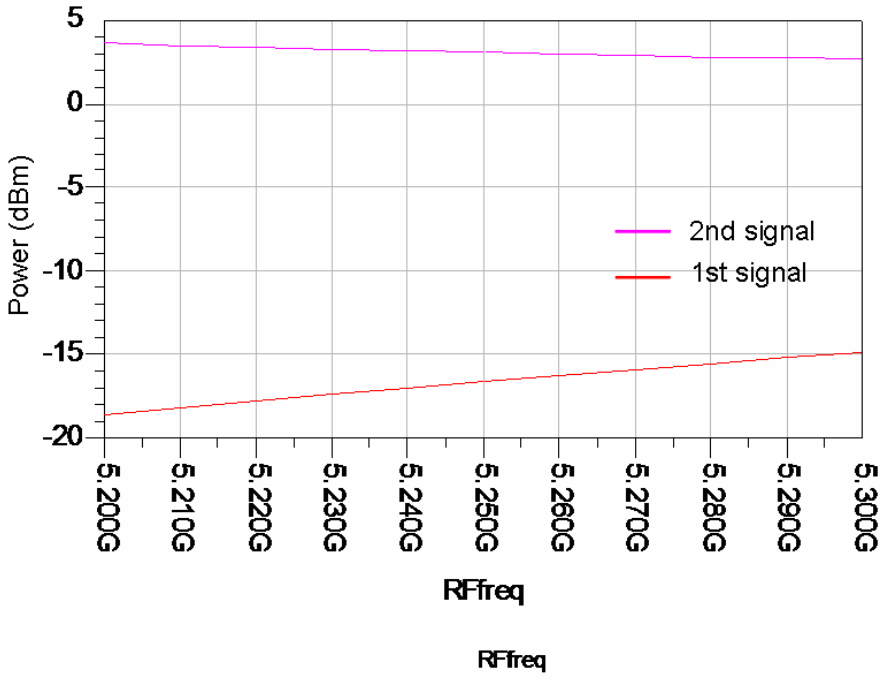

(a)

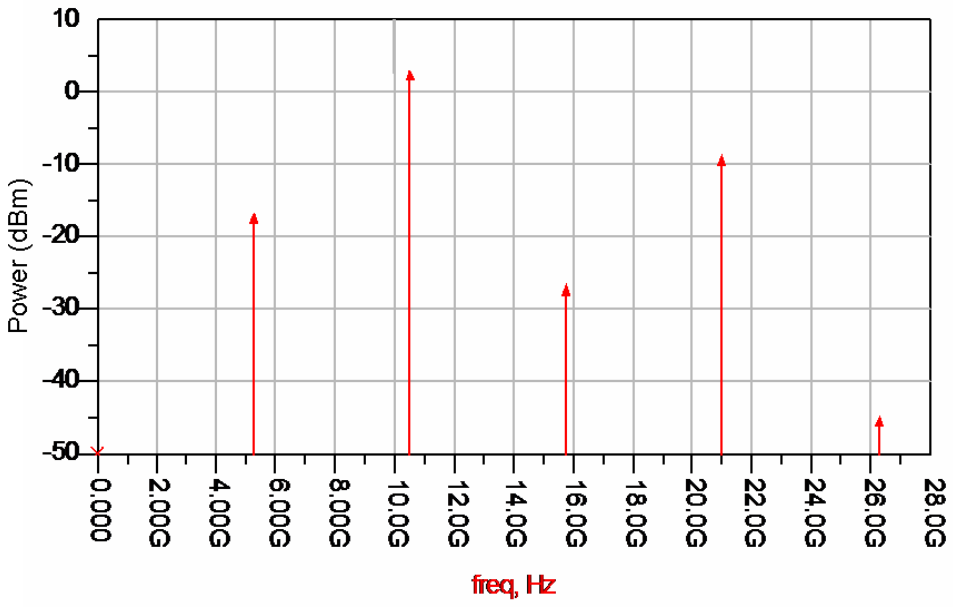

(b)

Figure 3.27 Simulated (a) output power and (b) harmonic spectrum of the frequency doubler with input power 4 dBm.

Figure 3.28 shows the photograph of the implemented 5.25 to 10.5 frequency doubler, and figure 3.29 illustrates the measured output power and harmonic spectrum when input power is 4 dBm. The results show a conversion gain is 4.7 dB and fundamental signal rejection ratio is better than 30 dBc. The experiment result shows better performance than the simulation one attributing to a better non-linear characteristic when biased at V_{GS}= 0 V in the real case than the equivalent circuit mode.

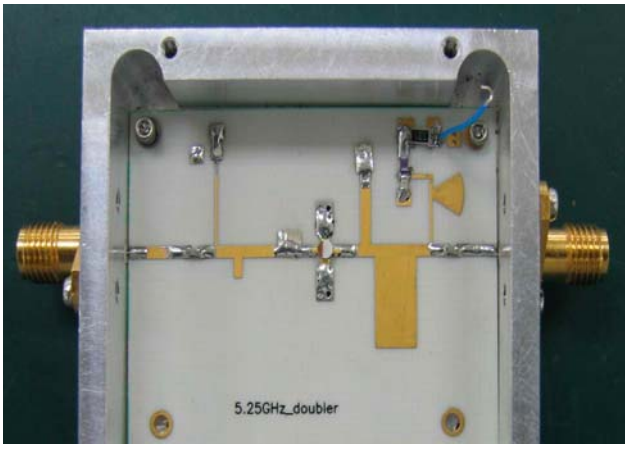

Figure 3.28 Photograph of 5.25GHz to 10.5GHz frequency doubler.

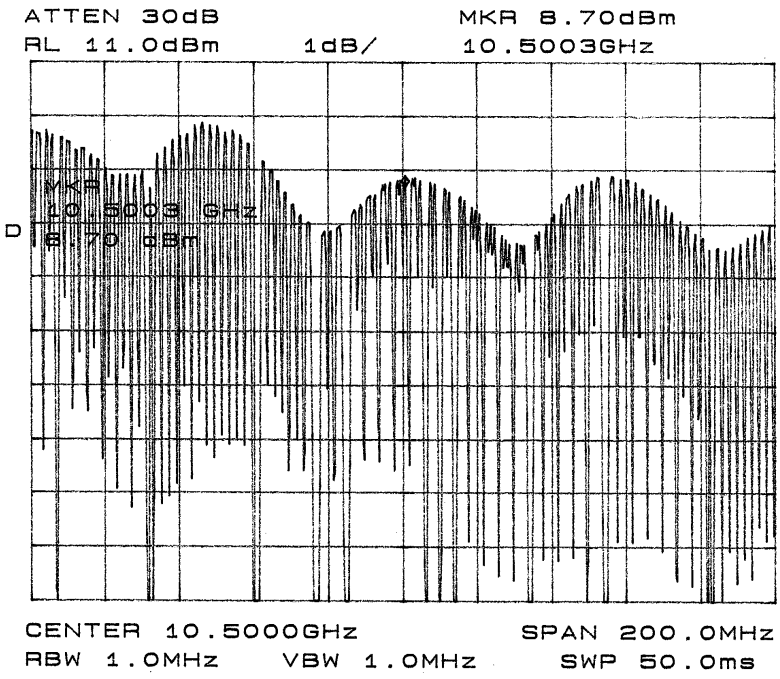

(a)

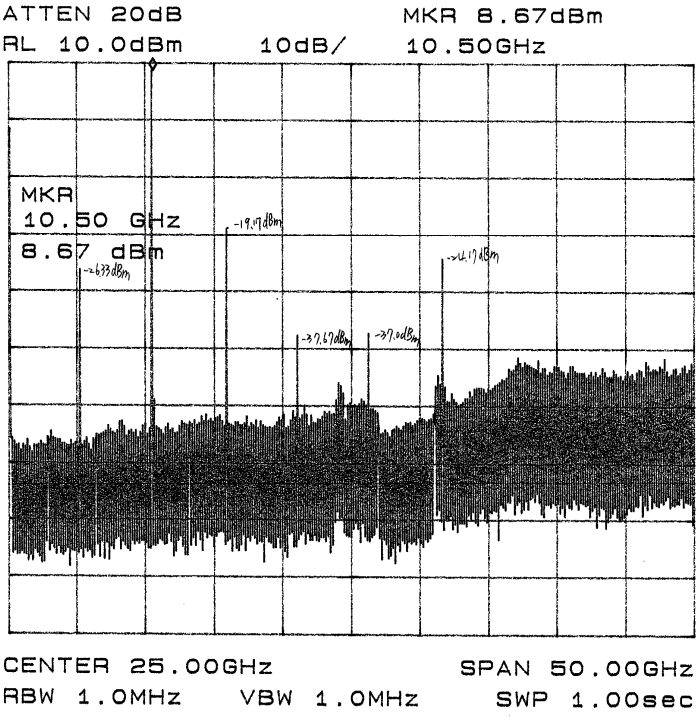

(b)

Figure 3.29 Measured (a) output power and (b) harmonic spectrum of the frequency doubler with input power of 4 dBm.

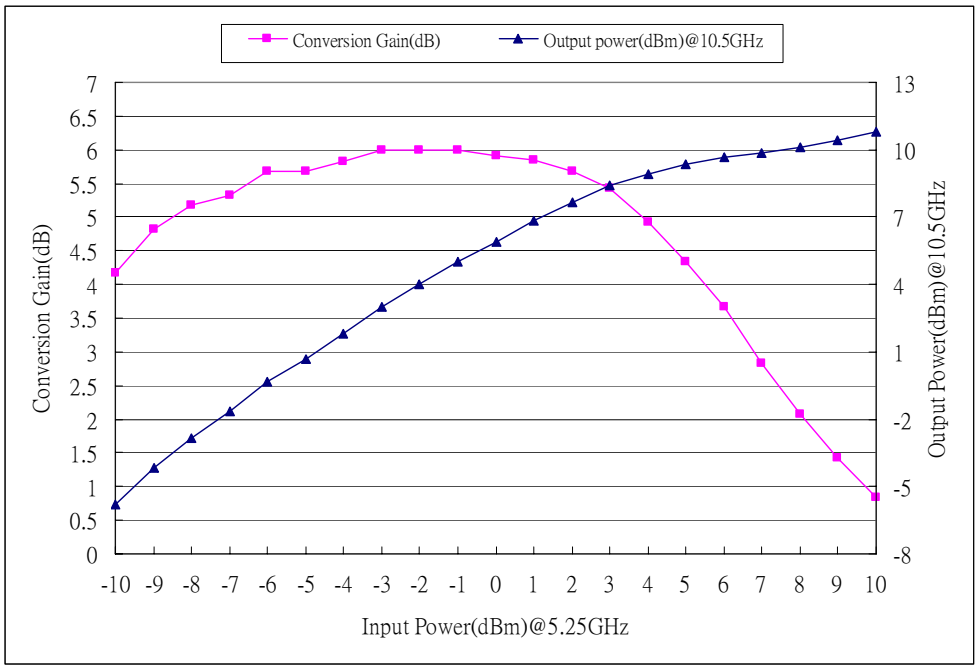

Figure 3.30 Measured conversion gain and output power of the frequency doubler versus the input power levels.

Figure 3.30 illustrates the conversion gain and output power performance versus the input power. From the result, the maximal conversion gain is around 6 dB with input power level of -2 dBm. As the input power increases the conversion gain decreases, and eventually the output power saturates to the output level of 11 dBm.

3.1.4 The 10.5 GHz band-pass filter

A edge-coupled microstrip BPF is designed in the transceiver architecture to filter out the unwanted harmonic signals. The design of the filter is performed by the EM-simulation software called IE3D. The BPF is designed on the substrate of RO-4003 with thickness of 20-mil. Figure 3.31 shows a photograph of the implemented BPF along with the measurement results. The result shows an insertion loss of 2.6 dB and a rejection ratio better than 40 dB at 5.25 GHz.

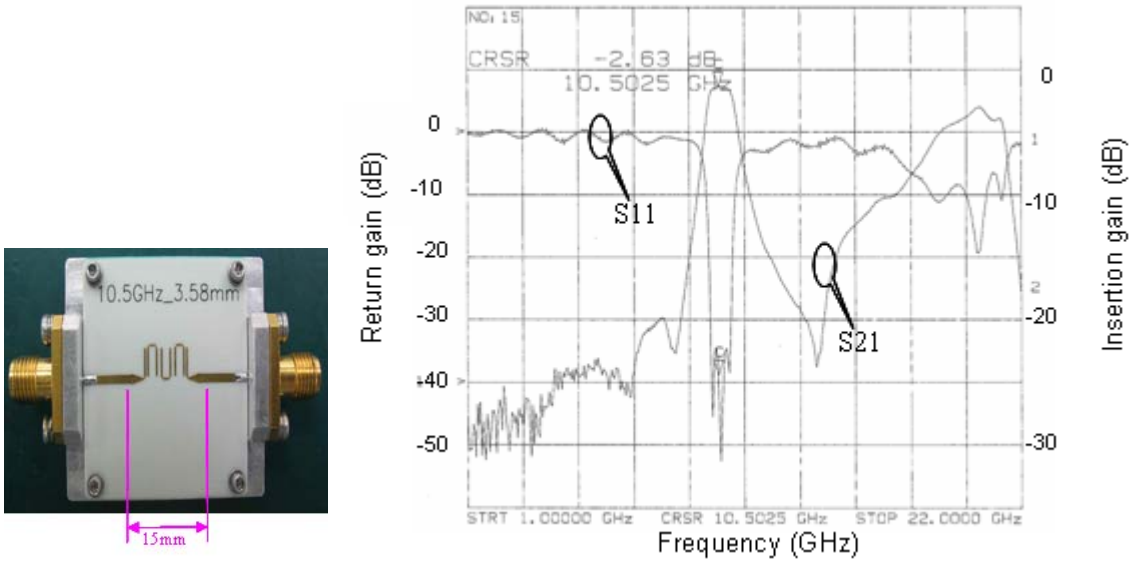

(a) (b)

Figure 3.31 (a) A photograph of the edge-coupled microstrip BPF and (b) the measurement result.

3.1.5 Integration of the single antenna radar transceiver

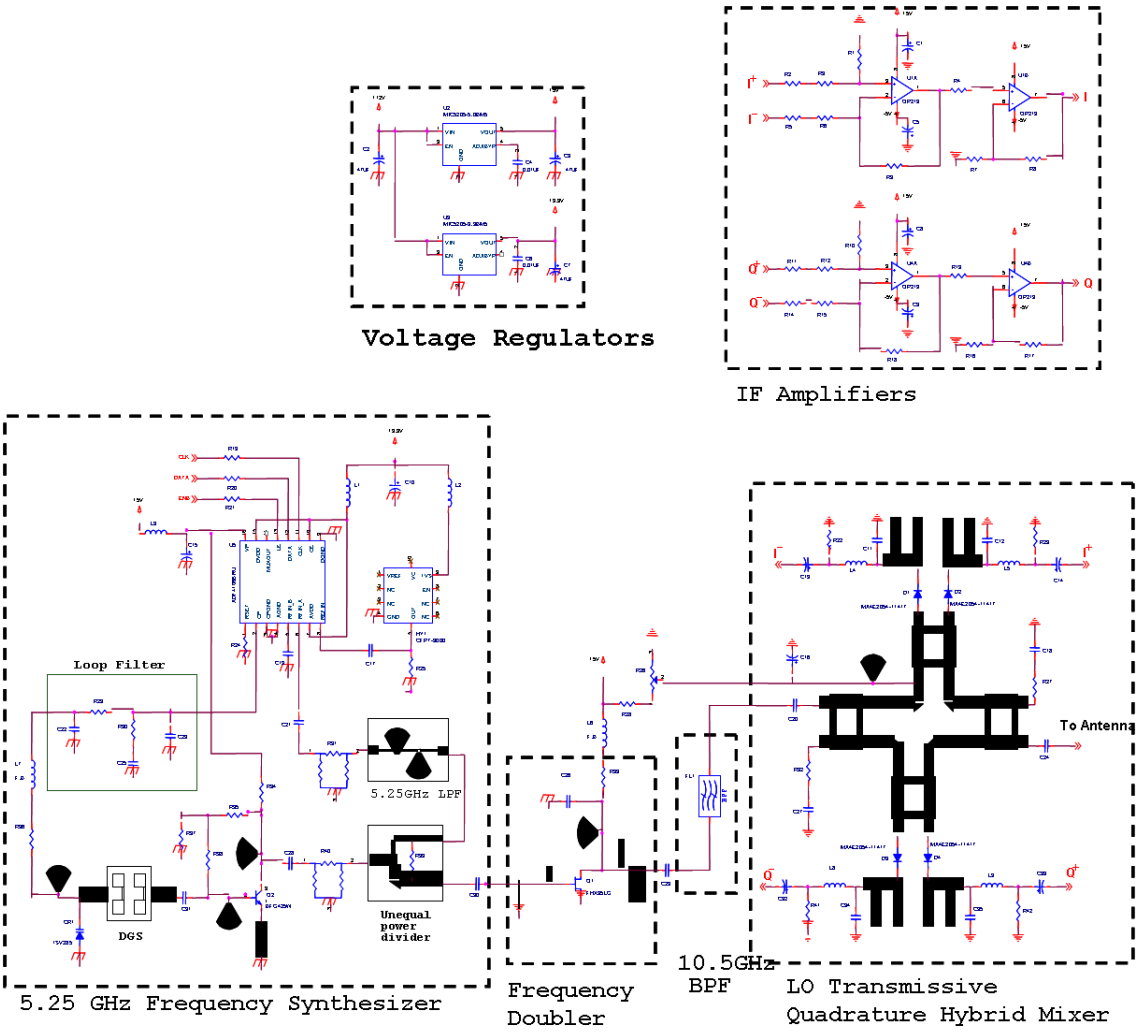

Figure 3.32 Complete schematic of the 10.5 GHz Doppler radar transceiver.

Figure 3.32 shows the complete circuit schematic of the presented 10.5 GHz Doppler radar transceiver. A 5.25 GHz frequency synthesizer, 5.25 to 10.5 GHz frequency doubler, a 10.5 GHz BPF, and a LO transmissive quadrature hybrid mixer are integrated into a single PCB. Two voltage regulators are also integrated to supply the required voltage source +5V and +3.3V. There are four IF amplifiers are used in this transceiver, two amplifiers for each I and Q channels. The amplifiers are used to convert the differential output from the hybrid mixer to single-ended and amplify the down-converted base-band signal. Figure 3.33 shows the photograph of the implemented radar transceiver.

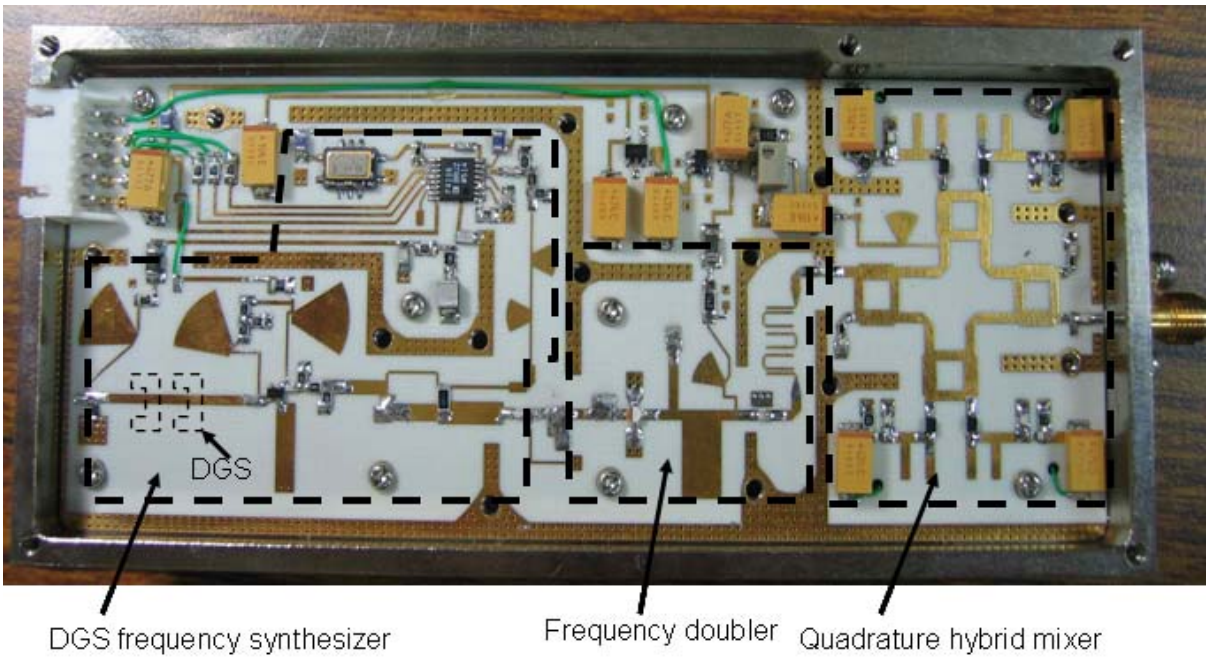

Figure 3.33 Photograph of the integrated 10.5 GHz Doppler radar transceiver.

Figure 3.34 shows the phase noise performance of the radar transceiver at the operating frequency of 10.5 GHz with the output power of 6 dBm and 0 dBm, respectively. The phase noise is -101 dBc/Hz when output power is 0 dBm, the result shows 8 dBc degradation from the 5.25 GHz synthesizer output. When the output power comes to 6 dBm, the phase noise degrades to -94 dBc/Hz. The descent of the phase noise performance is mainly contributed by the noise generated in the active frequency doubler. Figure 3.35 shows the measured harmonic spectrum of the radar transceiver in both 0 and 6 dBm output power levels. From this result, the fundamental frequency at 5.25 GHz is completely eliminated because of the help of 10.5 GHz BPF. The largest harmonic occurs at the frequency of 21 GHz with power of -47 and -32 dBm when output level is 0 and 6 dBm, respectively. Figure 3.36 gives a frequency sweep measurement of the output power. From this result, the transceiver is capable to generate RF signal from 10.36 to 10.76 GHz with a tuning range of 400 MHz and maximal power deviation less than 2 dB.

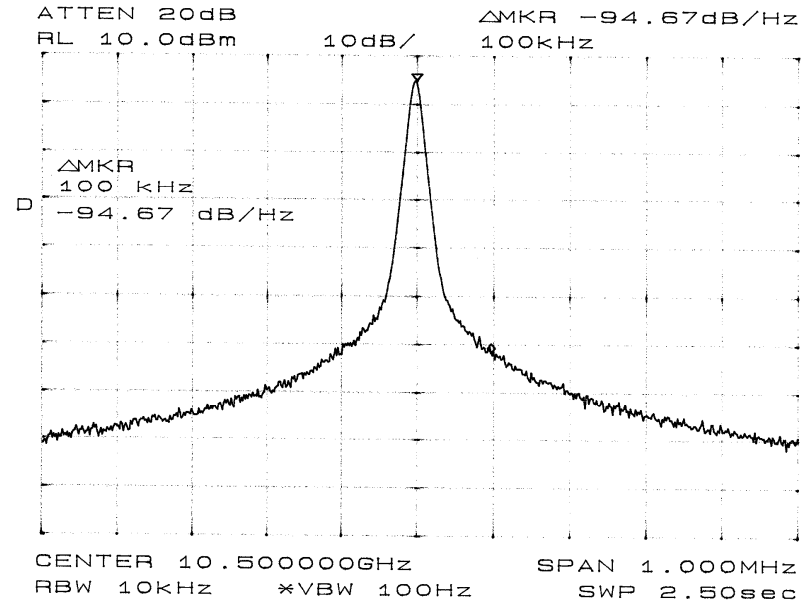

(a)

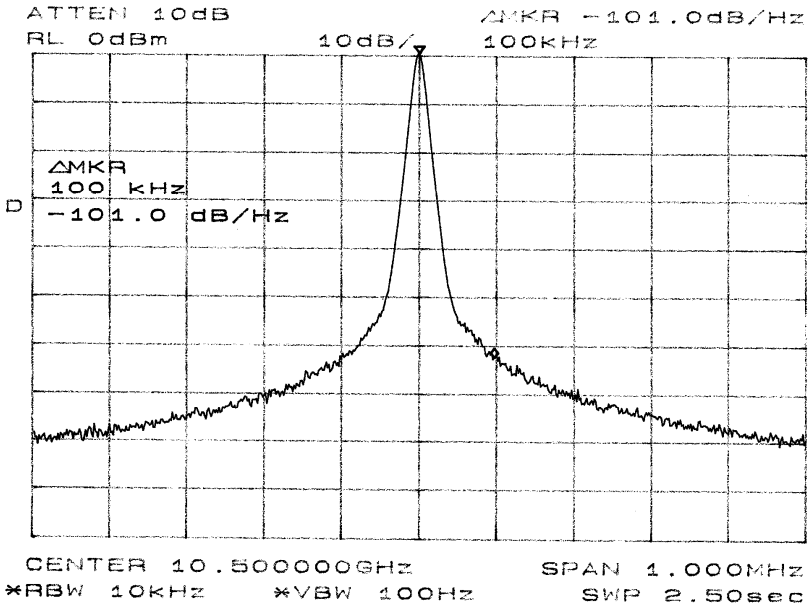

(b)

Figure 3.34 Measured phase noises of the radar transceiver at 10.5 GHz when output power is (a) 0 dBm and (b) 6 dBm.

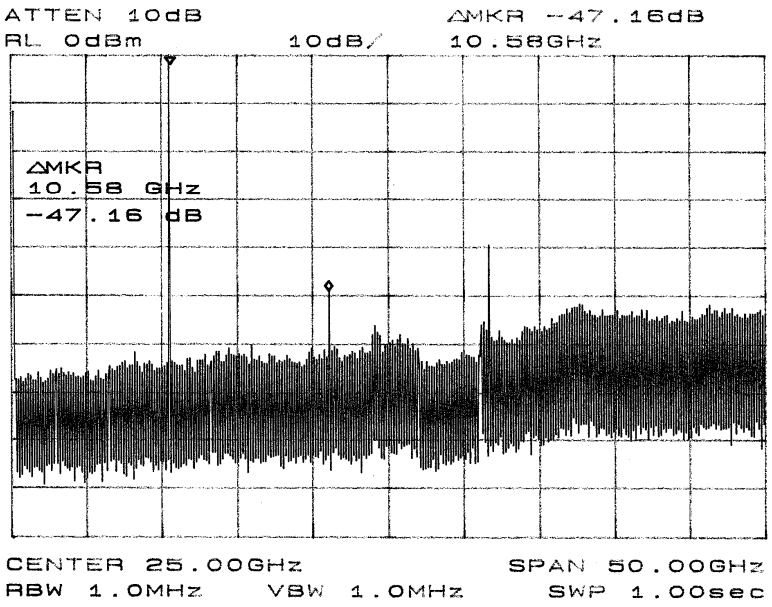

(a)

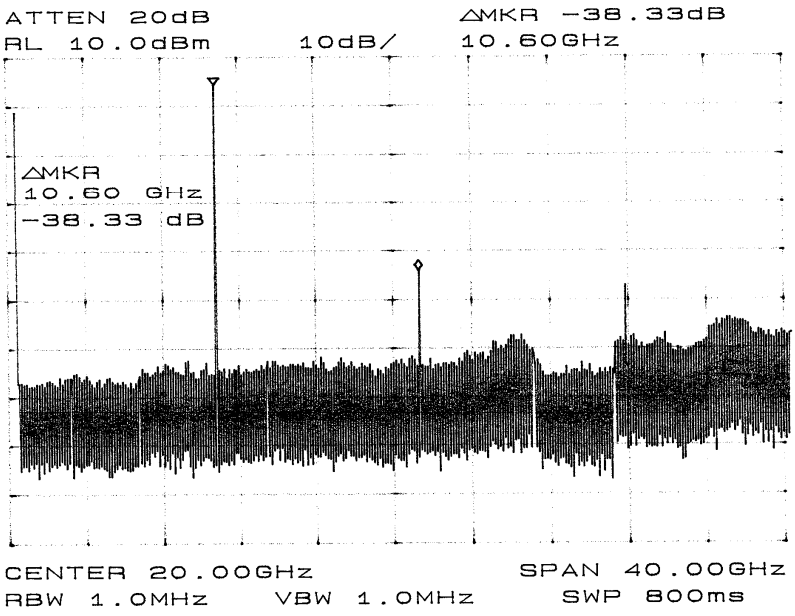

(b)

Figure 3.35 Measured harmonic spectrums of the radar transceiver when output power is (a) 0 dBm and (b) 6 dBm.

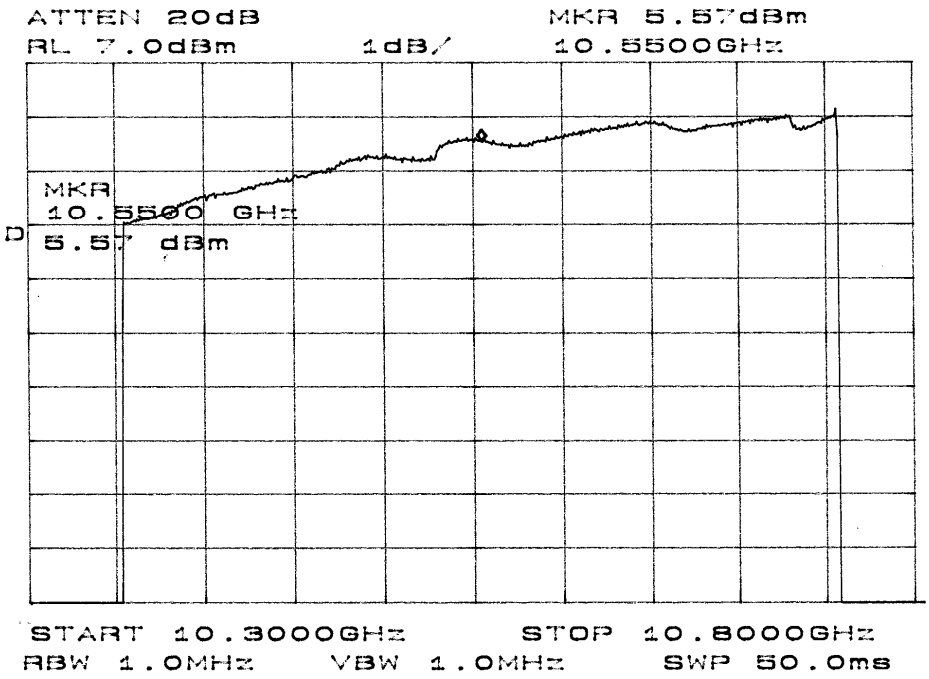

Figure 3.36 Measured output power of the presented radar transceiver with frequency sweep from 10.36 to 10.76 GHz.

3.2 Performance analysis between the LO transmissive quadrature hybrid mixer and conventional quadrature mixer

As depicted in chapter-2, the new quadrature hybrid mixer has the advantages of higher overall LO power usage efficiency, especially with limited output power level. In this section, another conventional quadrature mixer using ring mixer architecture as shown in figure 2.4 (a) is also fabricated and measured for comparison. The conventional one is designed using the same diode and followed by the same tuning network but replaces the hybrid mixers with a conventional ring mixer. Figure 3.37 shows the simulated conversion loss versus LO power level of both new LO transparent hybrid mixer and ring mixer. The conversion performances are really similar from this result in the single mixer section.

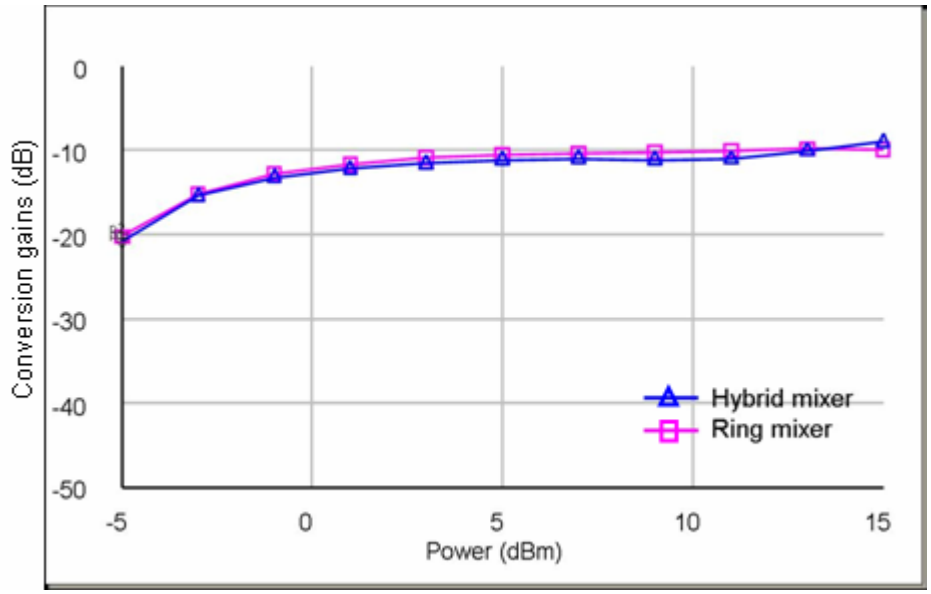

Figure 3.37 Simulated conversion losses of the proposed hybrid mixer and a ring mixer.

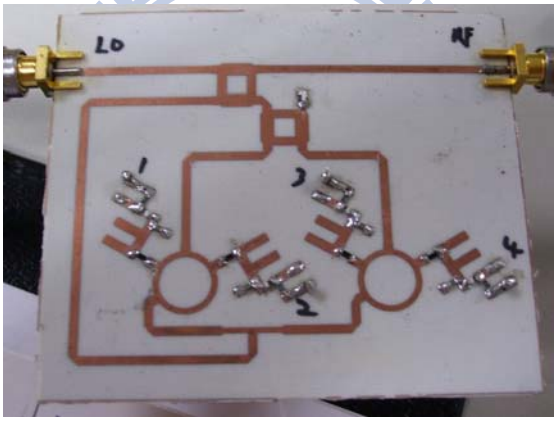

Figure 3.38 Photograph of the quadrature mixer using the conventional ring mixer architecture.

Figure 3.38 shows a photograph of the fabricated quadrature mixer using the ring mixer architecture. An inspecting equipment shown in figure 3.39 has been built up to evaluate the performances precisely. In this measurement, the mixers are driven by a precision signal generator (SG) Agilent E83640B. A running belt driven by a servo motor provides a constant Doppler frequency shift to the radar. An X-band standard horn antenna with 12 dBi gain is fixed above the belt with an incident angle of 15 degrees aimed to the running belt. The four IF ports of both the proposed and

conventional mixers are amplified independently, then these IF signals are acquired through a NI-DAQ (DAQ-6065) for analysis.

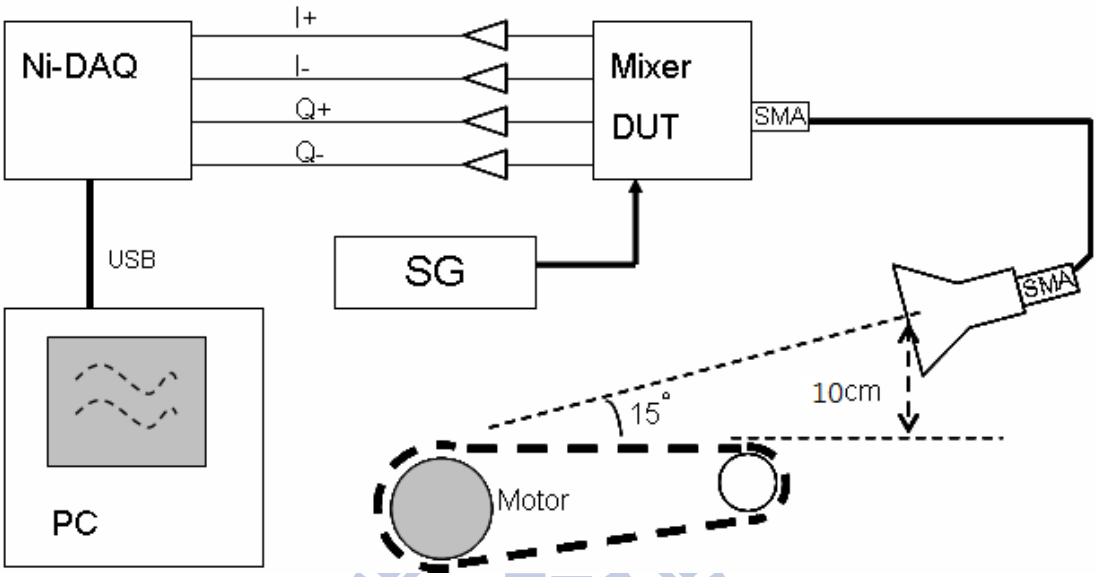

(a)

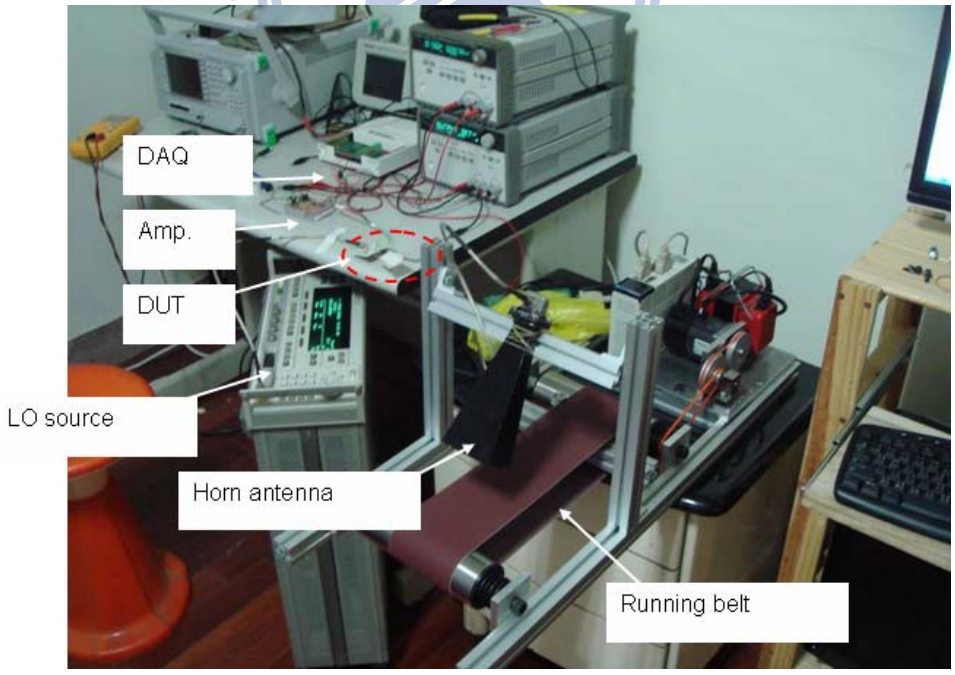

(b)

Figure 3.39 The environment (a) setup and (b) picture for the radar architecture evaluation.

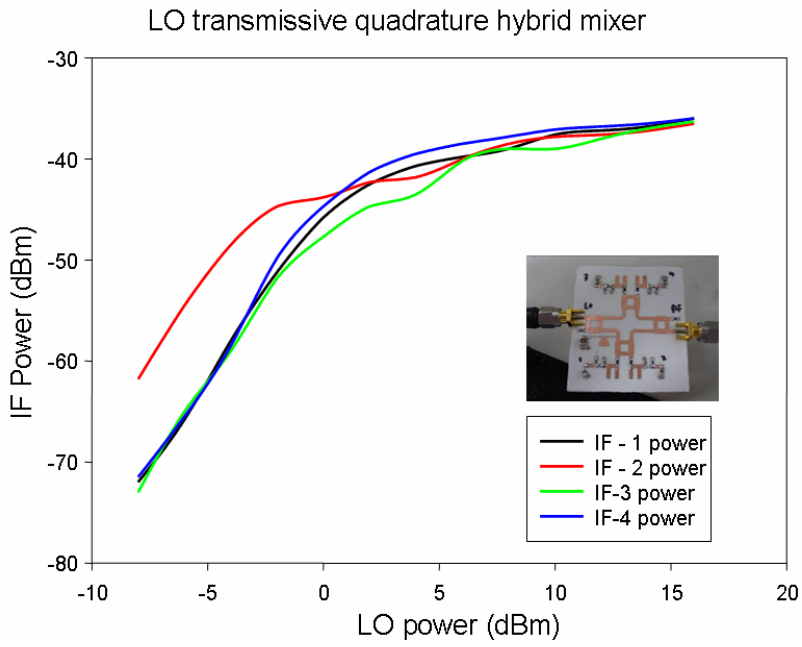

(a)

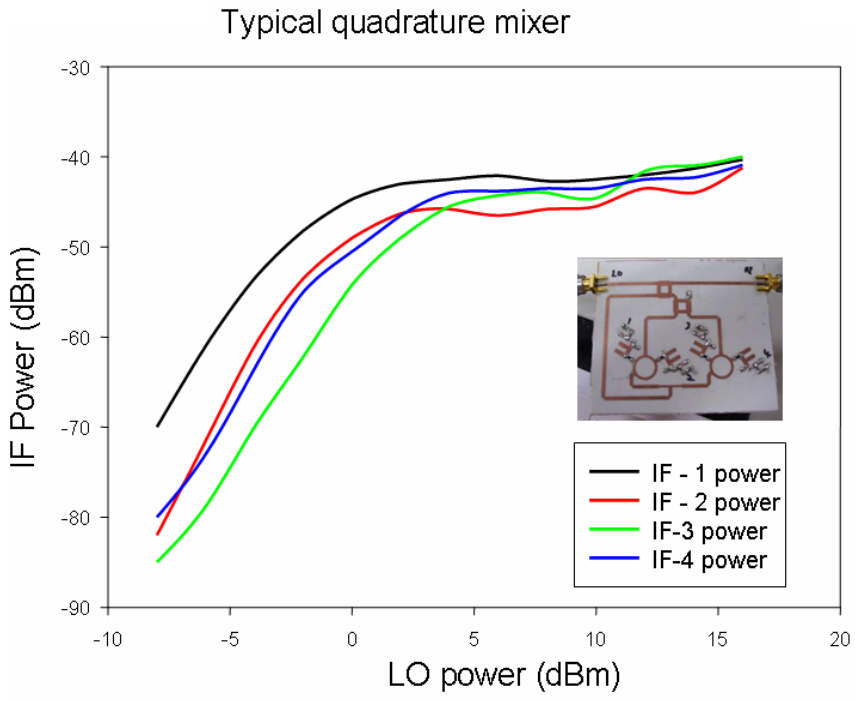

(b)

Figure 3.40 The received power at each IF ports of (a) the LO transmissive quadrature hybrid mixer and (b) a conventional quadrature mixer.

Figure 3.40 gives the measured receiving power at each IF ports of both LO transmissive quadrature hybrid mixer and conventional quadrature mixer. The received

powers deviate a lot when input power is lower than 5 dBm. The power difference is mainly contributed by the unbalance and mis-match of the mixer diode itself. As the LO power increase, all the mixer diodes are driven properly with sufficient LO power, then the power deviation is eased.

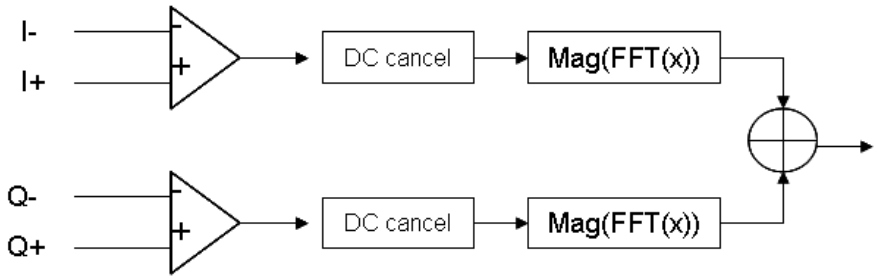

Figure 3.41 Signal processing flow of accumulating the total received power.

The received powers at each channel are then summed to obtain the overall power using the signal processing flow illustrated in figure 3.41. The positive and negative parts of both I and Q signals are subtracted first to get the real I / Q signals. Then these signals pass through a DC cancellation filter and perform the real-part FFT. The processed I and Q magnitude spectrum at the specified frequency index are summed together to get the total received power. Figure 3.42 shows the processed power spectrum density of the received I / Q and total power with various input LO power levels.

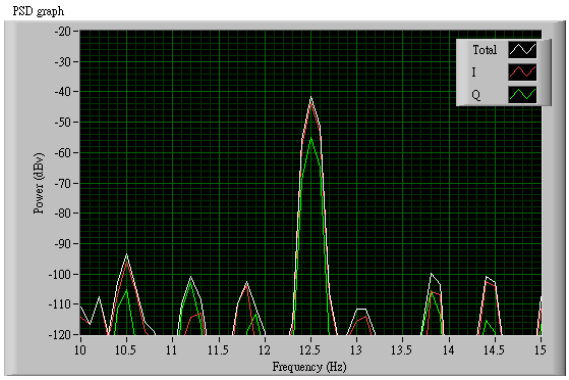

Hybrid mixer architecture 0dBm

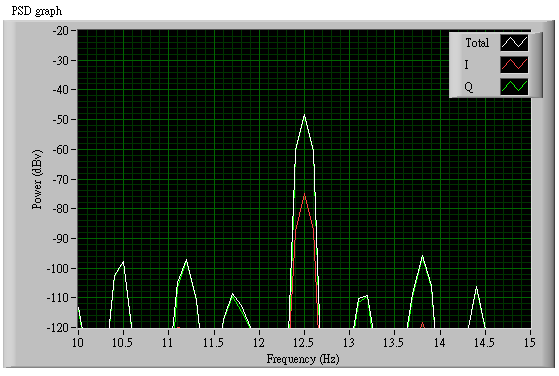

Ring mixer architecture 0dBm

(a)

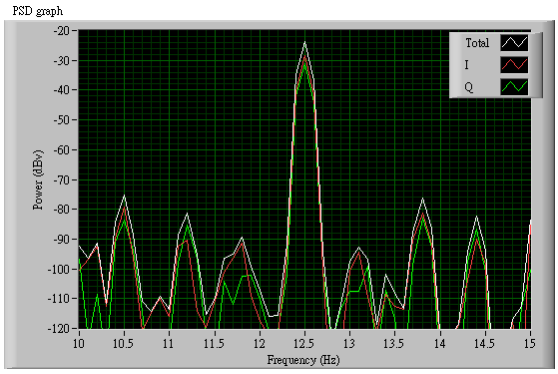

Hybrid mixer architecture 5dBm

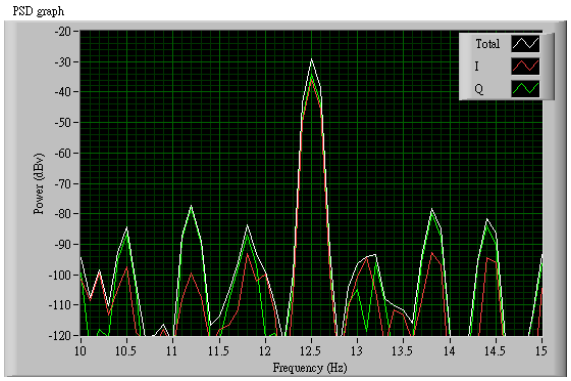

Ring mixer architecture 5dBm

(b)

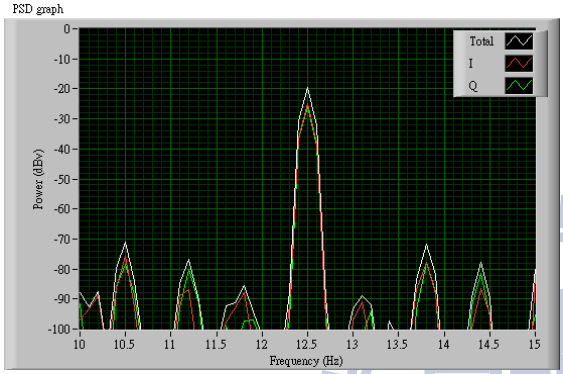

Hybrid mixer architecture 10dBm

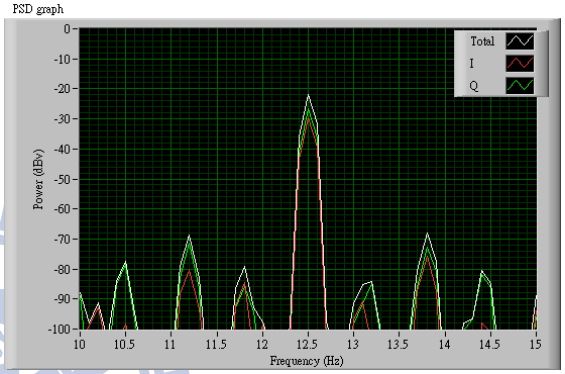

Ring mixer architecture 10dBm

(c)

Figure 3.42 Measured power spectrums of the received I / Q signals with input power of (a) 0 dBm, (b) 5 dBm, and (c) 10 dBm.

From this measurement, even though the received I and Q signal powers differ, the total power received by the proposed LO transmissive quadrature hybrid mixer architecture is higher than that of the conventional one at all LO power levels. Figure 3.43 gives a plot of the accumulated power at all ports versus the input power level. From this result, the proposed radar architecture has more than 3.6 dB improvement in the receiving power level than the conventional one. As mentioned in the first section of this chapter, the LO quadrature hybrid mixer is able to be biased to obtain the optimum performance, especially at low LO power condition. Figure 3.44 shows another experiment result of the quadrature hybrid mixer with additional bias voltage. The result shows a significant improvement in the conversion efficiency when LO power is lower

than 5 dBm. About 16.2 dB enhancement is achieved when the LO power is 0 dBm.

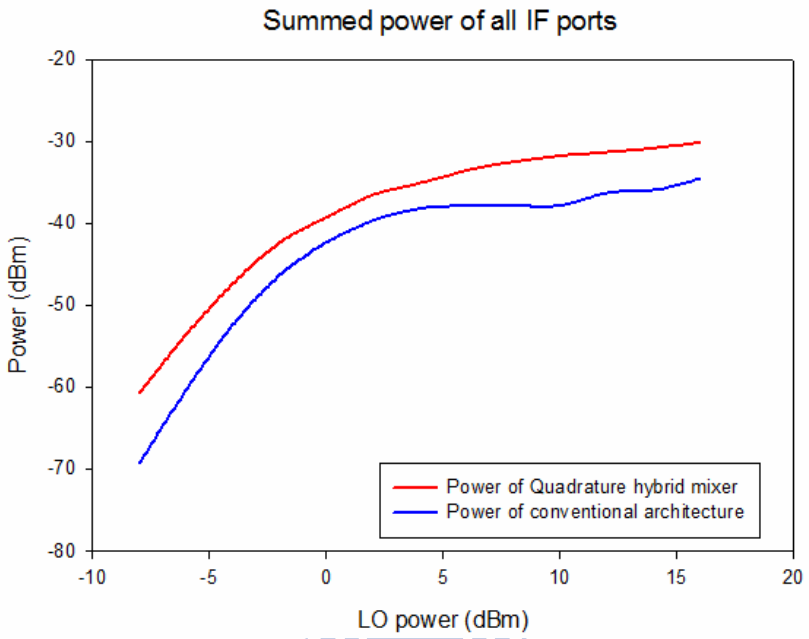

Figure 3.43 Accumulated power at all ports versus the input power level.

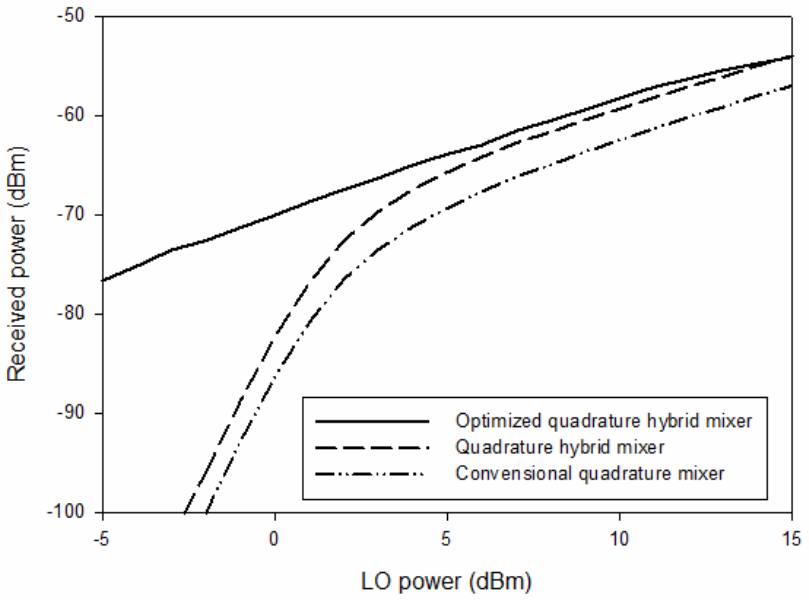

Figure 3.44 Received power of the LO transmissive quadrature hybrid mixer and conventional one versus LO power level.

3.3 Test of the 10.5 GH Doppler radar

A 10.5 GHz Doppler radar using the new LO transmissive quadrature hybrid mixer architecture and DGS frequency synthesizer is implemented to detect the direction and

speed of moving target. The radar front-end module is implemented on a RO4003 substrate. The Doppler radar transceiver is composed of a 5.25 GHz frequency synthesizer with DGS to enhance the phase noise performance, an 5.25 to 10.5 GHz active frequency doubler, a LO transmissive quadrature hybrid mixer, a 10.5 GHz band-pass filter, a base-band amplifier, and two voltage regulators. The output frequency can be synthesized from 10.4 to 10.8 GHz via digital control interface and the output power can also be adjusted by tuning the driving voltage to the active frequency doubler. The down-converted radar signal is filtered through an operational amplifier composed active LPF, which has a cut-off frequency at 100 kHz with 20 dB/decade slope and gain of 40 dB. A horn antenna with 12 dBi gain is used to transmit and receive the radar signals, and an ARM7 based microprocessor ADuC7021 with 12-bit analog-to-digital converters (ADC) and 12-bit digital-to-analog converters (DAC) is used to control the output frequency and power, acquire the base-band signal, and process the radar signal.

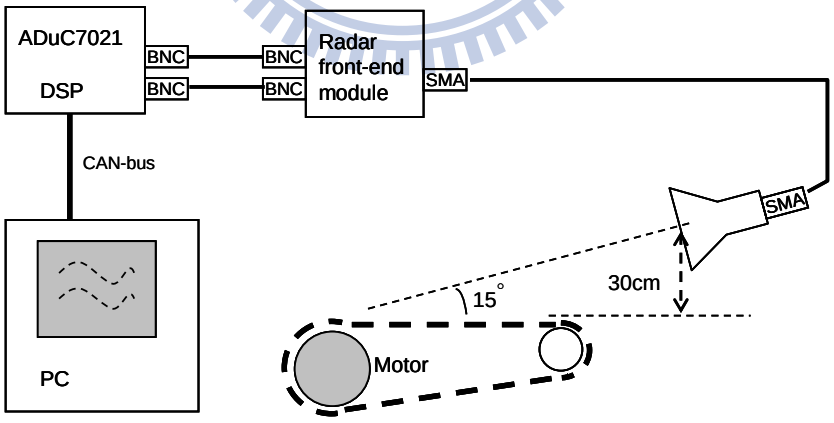

Figure 3.45 Environment setup to measure the Doppler radar module performance of acquiring the ground speed.

To evaluate the performance of ground speed acquirement, a test environment is setup in that way as shown in figure 3.45. There is a belt driven by a servo motor to simulate the relative speed to the ground. Table 3-6 gives the summary of the Doppler

shift measurement. The relative speed from 1 to 150 km/hr has been tested and evaluated. The measured speed has good agreement with the real belt speed.

Table 3-6 Summary of ground speed measurement.

Belt speed (km/h)	Measured Doppler frequency (Hz)	Estimated speed (km/h)
-150	-2817	-149.99
-75	-1409	-75.02
-25	-470	-25.02
-5	-94	-5
-1	-19	-1.01
1	18	0.96
5	93	4.95
25	469	24.97
75	1408	74.97
150	2817	149.99

The developed radar is tested to measure the direction and speed of a real vehicle on the roadside. The detection point is in a location approximate 20 m away from the antenna and there is a 10 degree difference between the main-beam direction and vehicle moving direction. Figure 3.46 shows the measured time-domain waveform at both I and Q channels with a vehicle (a) approaching at a velocity of 60 km/h, and (b) leaving at a velocity of 45 km/h. Figure 3.47 gives the calculated frequency-domain spectrum relate to figure 3.46. The result shows the Doppler frequency shift is 1149 Hz for the approaching target at the velocity of 60km/hr, and –861 Hz for the removing target at the velocity of 45 km/hr. Furthermore, the image rejection ratio of the transceiver is better than 25 dBc.

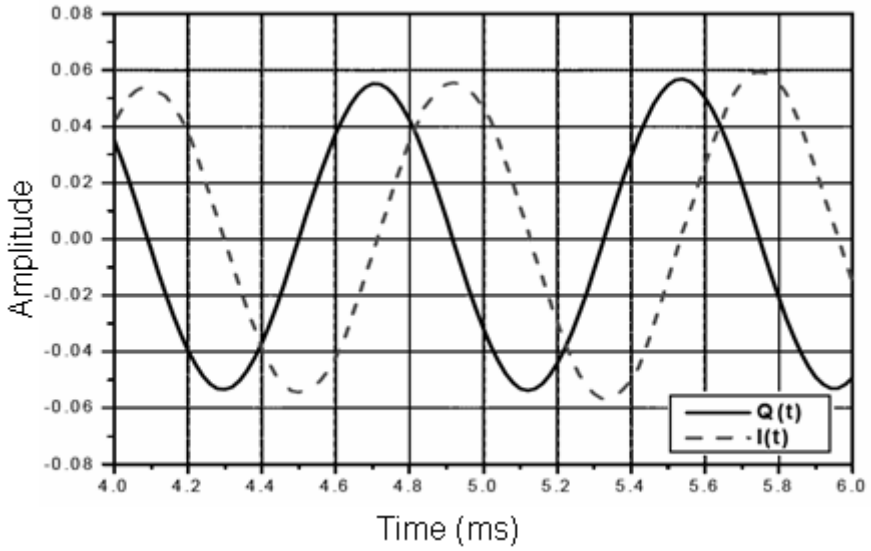

(a)

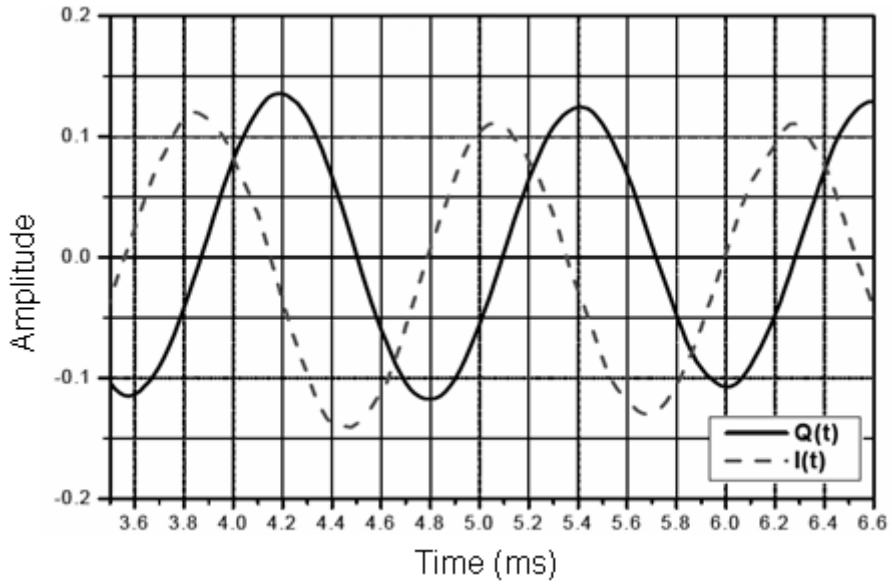

(b)

Figure 3.46 The acquired time-domain waveforms of the base-band signals from the output of the quadrature hybrid mixer for (a) a target with speed of 60 km/hr moving toward the sensor, and (b) a target with speed of -45 km/hr moving away from the sensor.

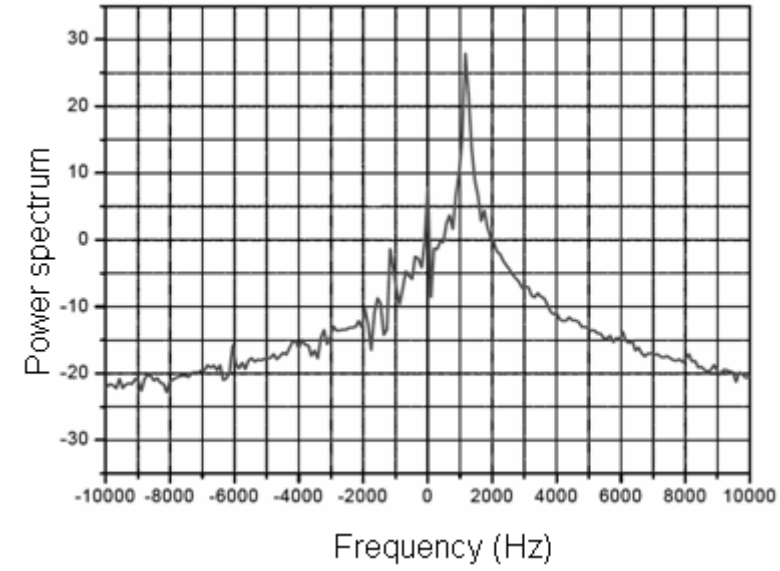

(a)

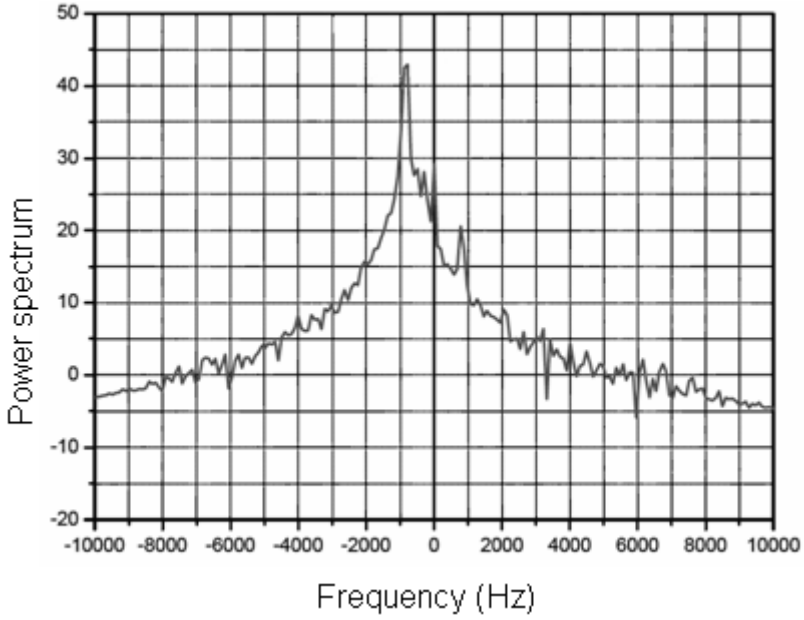

(b)

Figure 3.47 The power spectrum densities of the quadrature signals acquired from the proposed Doppler radar transceiver with (a) an approaching target with speed of 60 km/hr, and (b) a leaving target with speed of -45 km/hr.

Chapter 4 24 GHz Vehicle Collision Warning Radars

The collision warning radars are key equipment in the advanced vehicle safety system. In this chapter, two 24 GHz radar systems are presented. Comparing to the 77 GHz system, the 24 GHz systems has the advantages of lower cost and reliable durability. The linear FMCW technology has been adopted, which provides good distance resolution with relatively simpler circuit architecture. Within this chapter, the FMCW radar principle is first described, then, the design and implementation of the components used in the 24 GHz radar system are illustrated. In the following, a sideway-looking radar designed for vehicle blind-spot detection is presented. In the end of this chapter, the forward looking radar is proposed. A new frequency linearizer mechanism is adopted in this radar system to improve the modulation linearity. The two-dimensional Fast Fourier-Transform (2D-FFT) algorithm is also applied to this radar to estimate the obstacle relative distance and speed simultaneously.

4.1 FMCW radar principle

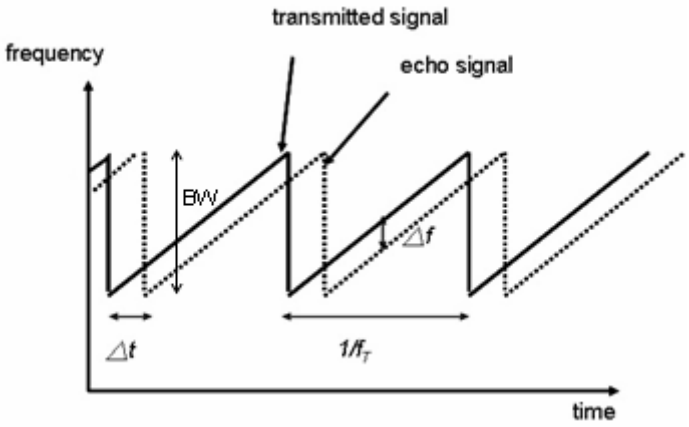

Figure 4.1 Modulation waveform of the FMCW mechanism.

The FMCW is a frequency modulation method which provides a way to acquire obstacle distance with simple circuit complexity and good resolution for the radar

applications. Figure 4.1 illustrates the basic concept of this technique.

In figure 4.1, the transmitter generates a linearly frequency modulated signal (also called as ramp signal) as the detection signal. The linear FM signal can be generated by applying a saw-tooth waveform to a regular VCO. The radar signal reflected from the obstacle is then received by the receiver. There is a relative time difference △t between the transmitted and received signals owing to the wave propagation delay in space. Because the output frequency varies as a function of time, there is a frequency difference between the transmitting and receiving signals. In other words, the relative distance can be obtained by measuring the frequency difference between the transmitting and receiving signals. In the analytical view point, the transmitting signal can be expressed as:

$$Tx(t) = A\cos[2\pi(f_0 t + \frac{1}{2}\alpha t^2 + \theta_0)] \qquad (4\text{-}1)$$

where A is the signal strength of the output power, f_0 is the fundamental frequency of the output ramp, α is the ramp slope, and θ_0 is the initial phase of the ramp signal. The T*x*(t) is the integral result of the linear ramp function $f_{Tx}(t) = 2\pi(f_0 + \alpha t)t$. The received signal can be obtained by replacing the *t* in Equ. (4-1) with *(t-△t)* , which can be expressed as:

$$Rx(t) = A\cos\begin{pmatrix} 2\pi\left[(f_0 - \alpha\Delta t)t\right] + \frac{1}{2}\alpha t^2 \\ +\left(-f_0\Delta t + \frac{1}{2}\alpha\Delta t^2 + \theta_r\right) \end{pmatrix} \qquad (4\text{-}2)$$

After mixing the Tx and Rx signals and extract the IF term by filtering the mixed signal through a LPF (ie, extract the phase difference term only), the IF signal can be expressed as:

$$IF(t) = M\cos\left(2\pi\left(\alpha\Delta t\right)t + f_0\Delta t - \tfrac{1}{2}\alpha\Delta t^2 + \theta_c\right) \qquad (4\text{-}3)$$

From this result, for a non-moving object, the time difference Δt is a constant, where the IF signal is simply a single-tone signal. The frequency of the IF signal is $\alpha\Delta t$, where Δt is a function of distance $\Delta t = \frac{2d}{c}$ (c is speed of light). Thus, the distance of object can be obtained by measuring the frequency of IF signal. In practice, the DFT (Discrete Fourier-Transform) is use to transfer time-domain signal to frequency-domain. Because of the limitation of sampling duration when applying the DFT, the frequency resolution can not be better than 1/T (T is the ramp duration) in theory. Thus, the theoretical distance resolution is limited to $\frac{c}{2BW}$, BW is the modulation frequency bandwidth occupied.

In the case of a moving target, Δt in Equ (4-2) is a function of time, because of the dynamic distance is changing. Where Δt is shown as $\Delta t = \frac{2(d_0 + vt)}{c}$ (v is the relative speed). The Equ. (4-3) should be rewritten like:

$$IF(t) = M\cos\left(2\pi\left[\begin{array}{l}\left(\frac{2\alpha d}{c} + \frac{2f_0 v}{c}\right)t \\ -\frac{4\alpha d_0 vt}{c^2} - \frac{2v^2t^2}{c^2} - \frac{2\alpha d_0}{c} + \theta_c\end{array}\right]\right) \qquad (4\text{-}4)$$

In the automotive applications, the relative speed v is much smaller then the speed of light c, the $1/c^2$ terms within the Equ. (4-4) can be omitted, thus, which can be simplified as:

$$IF(t) = M\cos\left(2\pi\left[\left(\frac{2\alpha d}{c} + \frac{2f_0 v}{c}\right)t + \theta_m\right]\right) \qquad (4\text{-}5)$$

From this result, the speed will influence the IF signal by adding a Doppler frequency shift to the IF output. When the Doppler shift is larger than half of the frequency resolution of DFT, the influence becomes visible and results in an inaccurate reading of the estimated target distance. From this view point, the ramp frequency should be larger than twice of the maximal Doppler shift to avoid the influence of Doppler shifting.

4.2 Design and implementation of the components for 24 GHz radars

Several components are developed for the 24 GHz radars, includes a 6 GHz VCO, a 6 to 12 GHz frequency doubler, a 12 to 24 GHz frequency doubler, a 12 GHz gain block, a SHM (Sub-Harmonic Mixer), and a 24 GHz LNA. The 6 GHz VCO is selected as the signal source because of the advantages of lower cost, good stability, and relative easier to fabricate. The transmitting signal is doubled twice to 24 GHz by two frequency doublers. The SHM is adopted which can down-convert the received 24 GHz signal to base-band with 12 GHz LO signal. The forward-looking system needs longer detecting range than the blind-spot detecting system, which means a higher sensitivity receiver is required. A 24 GHz LNA is also designed to provide better signal-to-noise ratio than just connect the mixer to the antenna directly.

4.2.1 6 GHz Voltage-Controlled Oscillator

Figure 4.2 (a) shows the schematic of the designed 6 GHz VCO. A general purposed BJT (BFG425W) is used in this design. The transistor is biased at a 3V with I_C = 18 mA. The varactor diode is selected using SMV-1232.

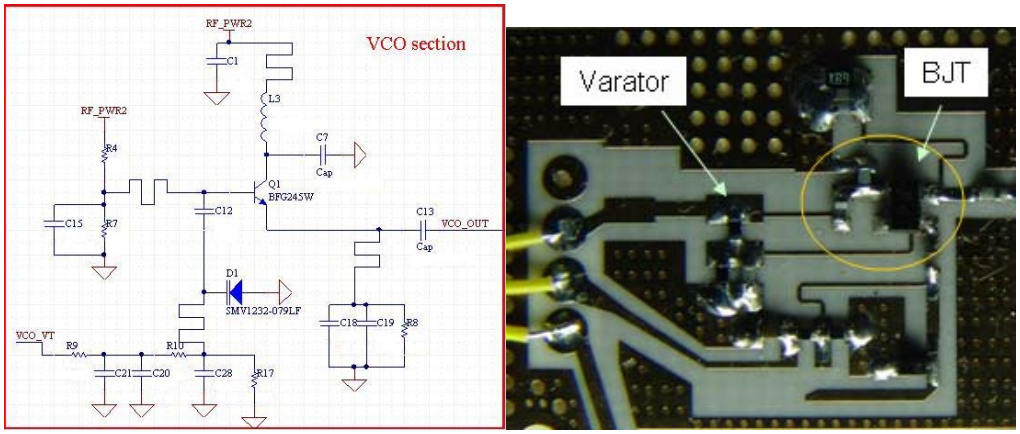

Figure 4.2 (a) Schematic and (b) photograph of the 6 GHz VCO.

Figure 4.3 (a) gives the output frequency response versus the tuning voltage of the 6 GHz VCO. For a tuning voltage range from 0 to 5 V, the VCO output varies from 5.85 to 6.2 GHz. As illustrated in the Figure 4.3 (b), this design also shows phase noise of -98 dBc/Hz at 100 kHz offset. The measured output power of the fabricated one is 8 dBm.

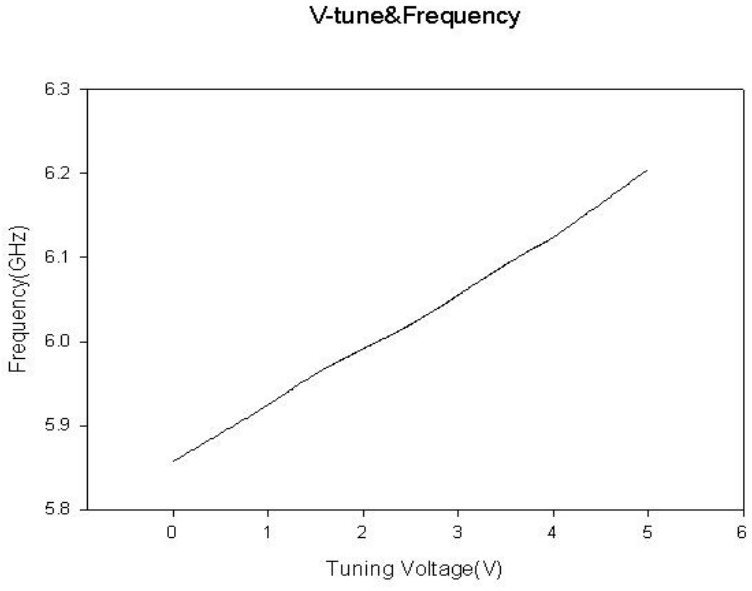

(a)

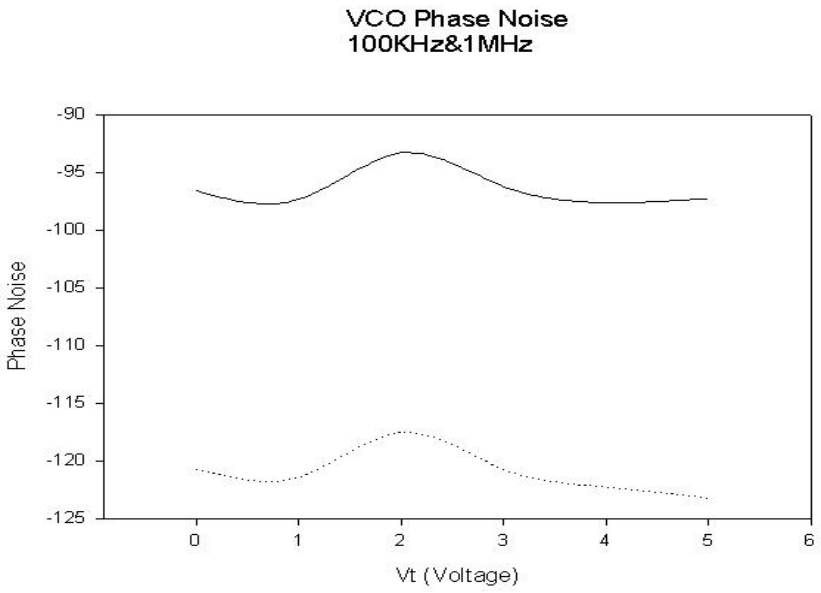

(b)

Figure 4.3 Measured (a) output frequency and (b) the phase noise of the 6 GHz VCO.

4.2.2 Active Frequency doublers

Figure 4.4 shows the schematic of the 6 to 12 GHz frequency doubler. A FET (FHX76LP) is used in this design. The FET is biased at the condition of V_{GS} = 0 V for the best non-linear characteristics, the current is controlled to I_D = 20mA by a series resistor connected between the power supplier and drain port of the FET. An open stub with length equal to half wavelength at 12 GHz is connected to the output port. The open stub doesn't affect the output impedance for the 12 GHz signal, however it shows a short circuit condition to the 6 GHz signal thus eliminates the 6 GHz signal leakage. In the input, another open stub with length equal to quarter wavelength at 12 GHz is connected. The open stub in the input section helps to reflect the leaked 12 GHz signal back to the FET and thus improves the conversion efficiency. Another short stub with length of half wavelength of 12 GHz signal also added in the input section. The short stub keeps the gate DC voltage to zero and also helps to reflect the 12 GHz signal back

to the FET because of the short circuit characteristic shown at 12 GHz.

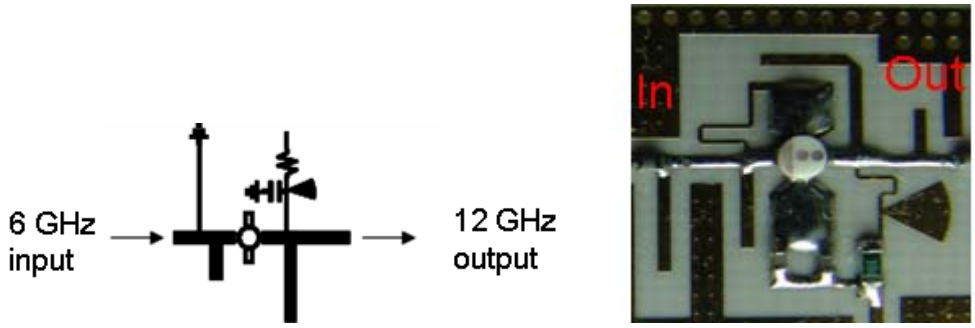

(a) (b)

Figure 4.4 (a) Schematic and (b) photograph of the 6 to 12 GHz frequency doubler.

Figure 4.5 shows the measurement result of the 6 to 12 GHz frequency doubler. The conversion loss is 5 dB when applying an input power of 8 dBm. From this result, a 3 dBm 12 GHz output power level can be expected when connect the previous 6 GHz VCO to the frequency doubler input directly.

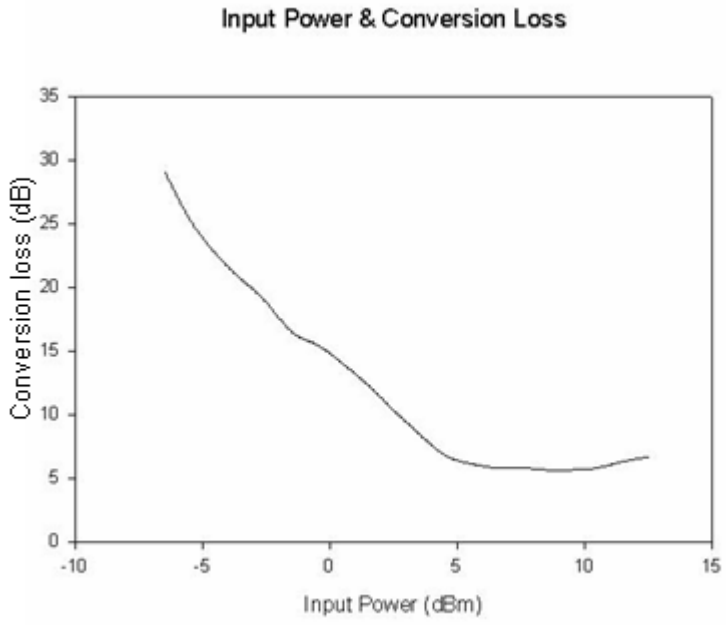

(a)

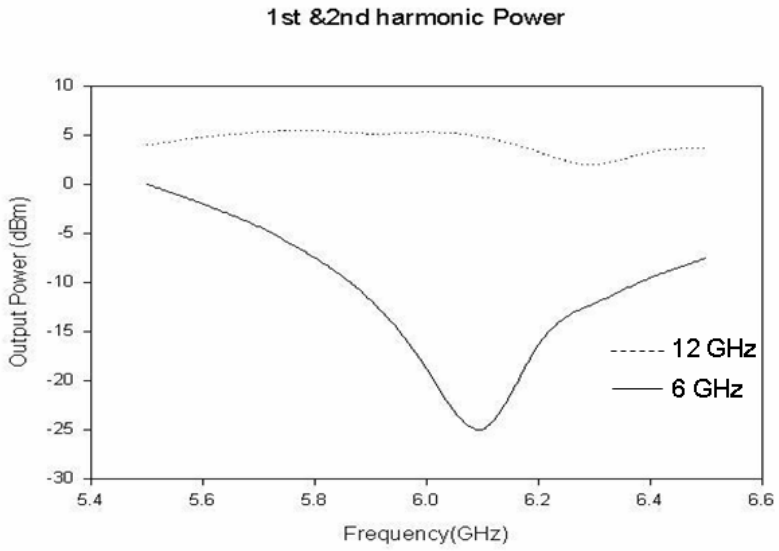

(b)

Figure 4.5 Measured (a) conversion loss and (b) output harmonic powers of the frequency doubler with input power of 8 dBm.

Another 12 to 24 GHz frequency doubler is also designed to convert the LO signal to the required frequency band. Figure 4.6 shows the (a) schematic and (b) photograph of the designed 12 to 24 GHz frequency doubler. The transistor is selected as FHX76LP with a bias point of V_{GS} = 0 V, I_D = 20 mA. In the output part, a 24 GHz BPF is connected. The BPF allows the 2nd harmonic pass through only, and thus eliminates the leakage of the1st and 3rd harmonic signals. In the input section, a short stub with a length of 12 GHz quarter wavelength is connected.

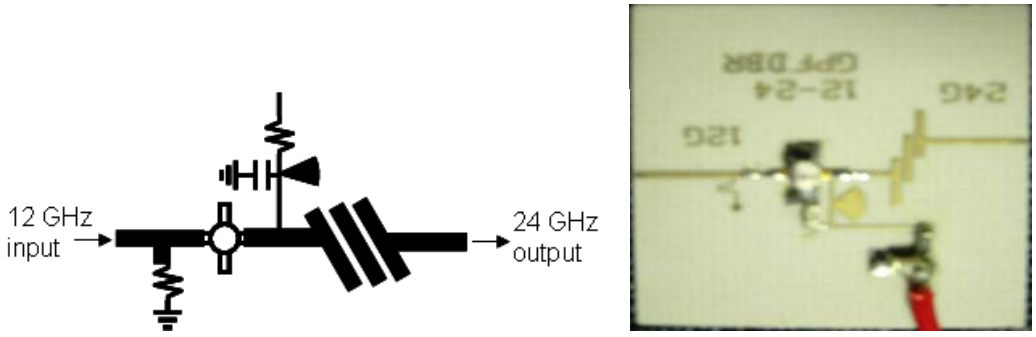

(a) (b)

Figure 4.6 (a) Schematic and (b) photograph of the 12 to 24 GHz frequency doubler.

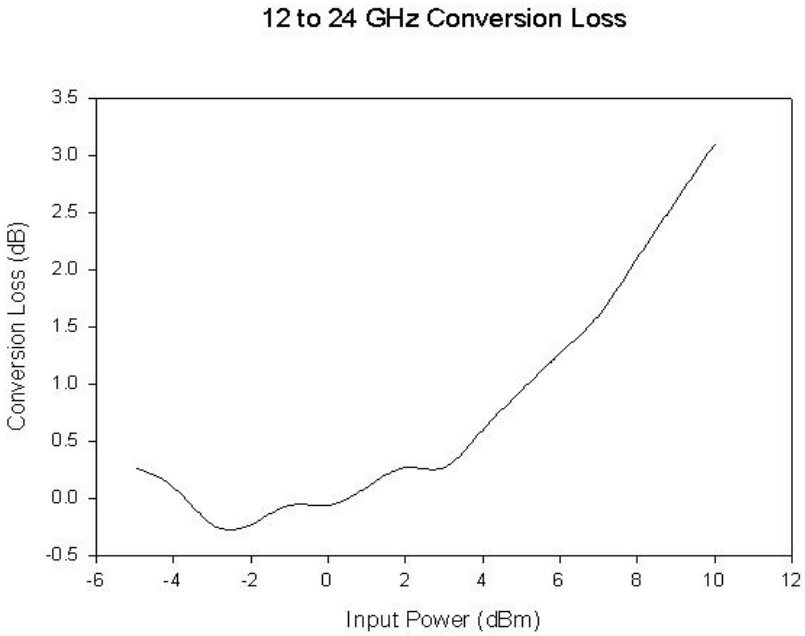

Figure 4.7 Measured conversion loss of the 12 to 24 GHz frequency doubler.

Figure 4.7 gives the measured conversion loss of the 12 to 24 GHz frequency doubler. The designed doubler shows an optimum conversion gain of 0.2 dB when input power is -3 dBm. The 1st harmonic is suppressed below -30 dBm. When the input power is 3 dBm, a 24 GHz output power of 2.6 dBm can be obtained.

4.2.3 12 GHz Gain Block

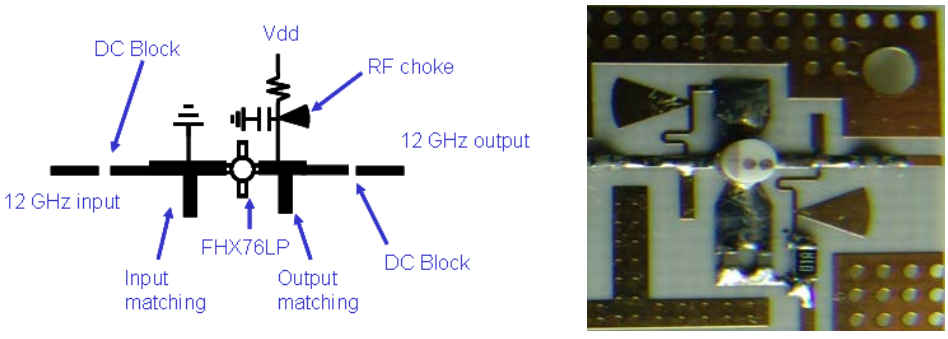

(a) (b)

Figure 4.8 (a) Schematic and (b) photograph of the 12 GHz gain block.

Figure 4.8 shows the schematic and photograph of the 12 GHz gain block. The gain block is designed using the FHX76LP FET which is biased at V_{GS} = 0 V and I_D = 35 mA. The purpose of this gain block is to enhance the 12 GHz signal strength for the down-converting mixer. In the FMCW system, the AM noise contributed by variance of LO power is significant. The gain block also performs as a power limiter to the LO signal, which ensures a stable power level delivered to the mixer in different FM modulating index.

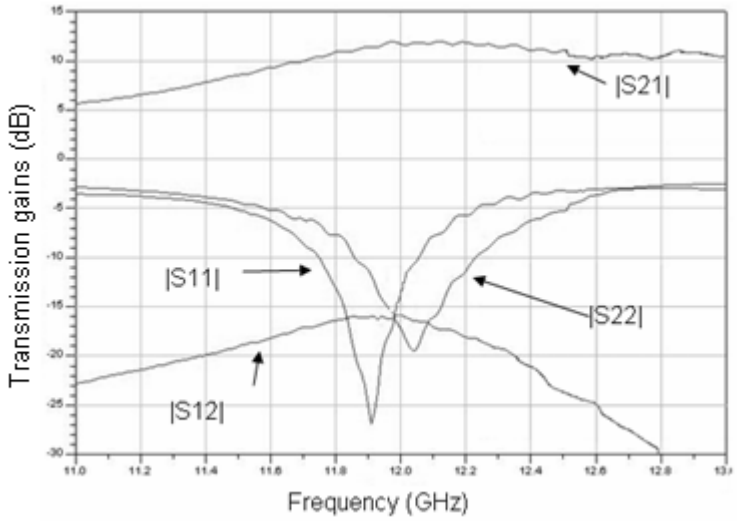

(a)

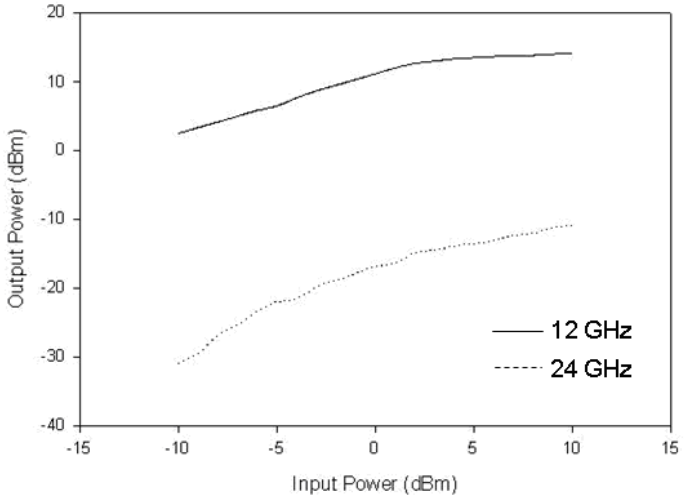

(b)

Figure 4.9 Measured (a) frequency response and (b) output power of the 12 GHz gain block.

Figure 4.9 (a) and (b) shows the measured frequency response and output power of the 12 GHz gain block, respectively. From this result, the transmission gain is about 12 dB around 12 GHz. The output power saturates to 12.5 dBm when input power is larger than 3 dBm, thus, a stable output power can be obtained when input power larger than 3 dBm even if the input power varies.

4.2.4 24 GHz LNA

A 24 GHz LNA is designed for the forward-looking radar application. Figure 4.10 (a) and (b) gives the schematic and photograph of the designed 24 GHz LNA, respectively. There are two stages in the LNA. The input matching of the first stage is designed to have the optimum noise figure, while the second stage provides the necessary gain to the output. The transistors are selected using the FHX76LP, with bias condition of V_{GS} = 0 V, and I_D = 20 mA each.

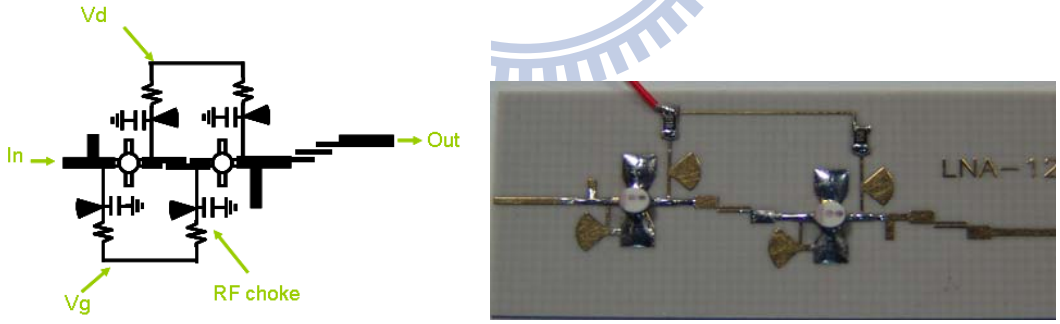

(a) (b)

Figure 4.10 (a) Schematic and (b) photograph of the 24 GHz LNA.

Figure 4.11 gives the measured amplifier gain and noise figure of the designed 24 GHz LNA. The transmission gain is about 18 dB around 24 GHz, with the noise figure of 3 dB.

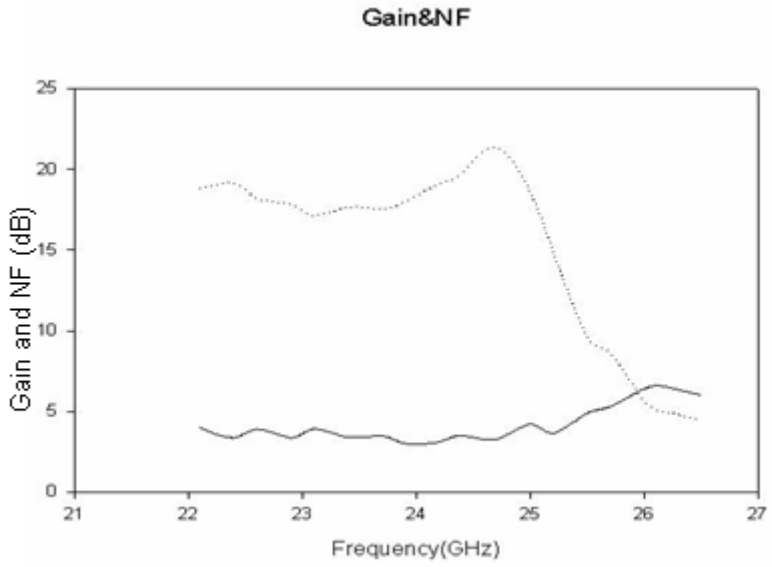

Figure 4.11 Measured gain and noise figure of the 24 GHz LNA.

4.2.5 Sub-Harmonic Mixer (SHM)

A SHM is designed as the down-converting mixer in the 24 GHz radar systems. An anti-paralleled Schottky diode DMK-2308 is used in this design because of the excellent characteristic that no 2nd harmonic signal can be generated from this diode configuration. Figure 4.12 shows the schematic of the SHM. In the RF terminal, an open stub with length of half wavelength at 24 GHz is connected. The open stub shows as a virtual short to the 12 GHz signal and thus eliminates the leakage to antenna. In the LO terminal, a pair of open / short stubs are connected. Each stub has the length of quarter wavelength at 24 GHz. The open stubs show a virtual ground characteristic which reflects the 24 GHz signal and thus enhances the conversion gain. The open stubs will also affect the input impedance to the 12 GHz signal. Thus, two short stubs are connected to compensate the influence of open stubs to the 12 GHz signal.

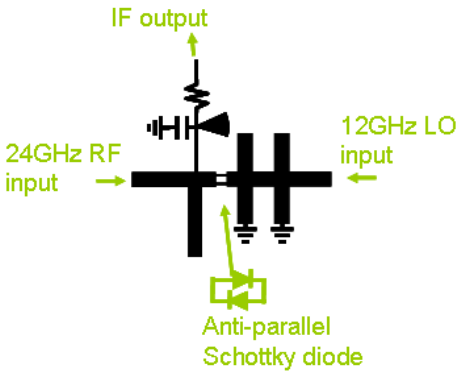

Figure 4.12 Schematic of the SHM.

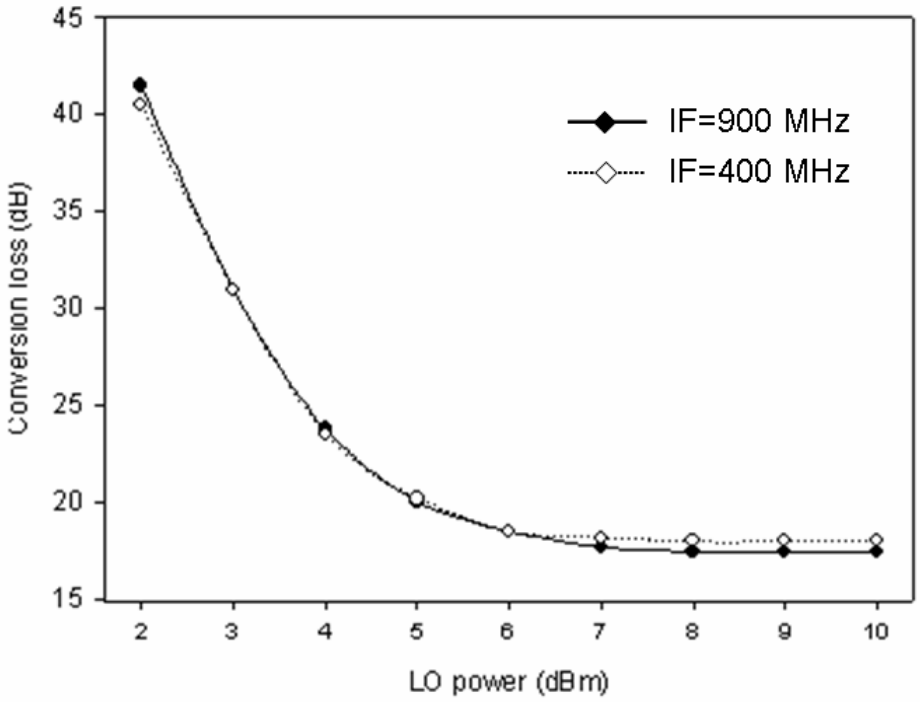

Figure 4.13 Measured conversion loss of the SHM.

Figure 4.13 shows the measured conversion loss of the SHM. The conversion loss is about 17 dB when the LO power is larger than 7 dBm.

4.3 A compact 24 GHz radar sensor for sideway-looking applications

A sideway-looking radar is proposed to be installed under the back-mirror of a small vehicle. The radar provides an active safety function to alarm the driver when there is any object (other vehicle) inside the vision blind spot area, like shown in figure 4.13. According to the ISO specification [40], if any object inside the red area the radar must alarm, while no object inside either the red or yellow area must not alarm. The radar should detect an area with minimal distance about 3.5 meters.

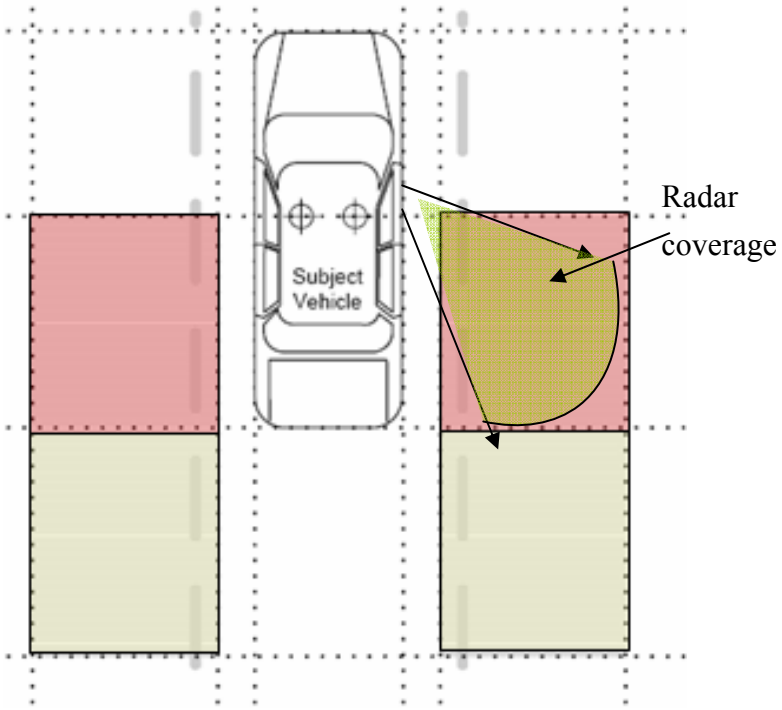

Figure 4.14 Blind spot area around a small vehicle and sideway-looking radar coverage area.

Figure 4.14 also shows the coverage of the presented sideway-looking radar. The radar is designed to have a detection range of 4 meters with a FOV (Field-of-View) angle of 30 degrees.

Figure 4.15 shows the system diagram of the 24 GHz sideway-looking radar system. The RF components are designed and illustrated in the previous section of this chapter. A 6 GHz VCO is adopted as the signal source, the signal is multiplied to the frequency

of 24 GHz by two active frequency doublers. A SHM is used to down-convert the received signal. A micro-controller (MCU) is used to generate the required modulating waveform. A digital signal processor (DSP) is implemented to process the signal and identify the objects.

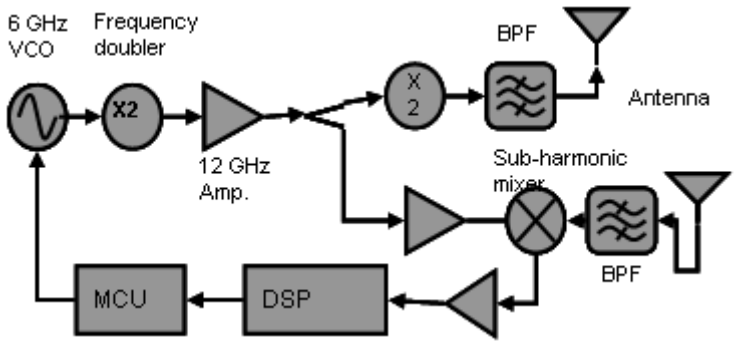

Figure 4.15 Block diagram of the 24 GHz sideway-looking radar.

The antenna used in this radar sensor is co-designed with the RF circuit board. Figure 4.16 shows the architecture of a patch-fed horn antenna. The feed of the antenna is a square probe planar patch designed at 24 GHz. The horn is fabricated using a light metal plat, which acts as the wave reflector and thus enhances the gain of the antenna. The antenna frames are connected to the RF circuit board by soldering. The antenna main beam is designed to have a 5 degree tilt angle from the broadside direction, in order to make the detection direction point to the vehicle blind spot. Figure 4.17 shows the directivity of the implemented antenna. The maximal gain of the designed one is about 10.2 dBi. The half-power beam width (HPBW) is around 30 degrees.

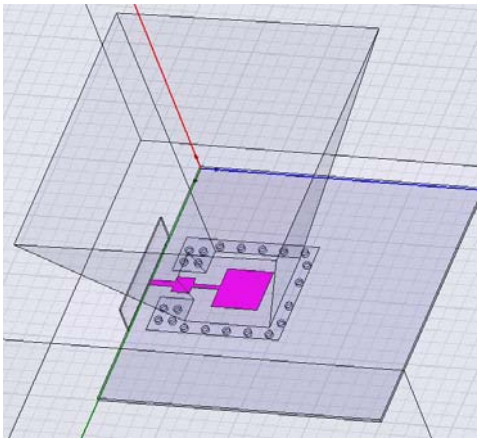

Figure 4.16 The architecture of the patch-fed horn antenna.

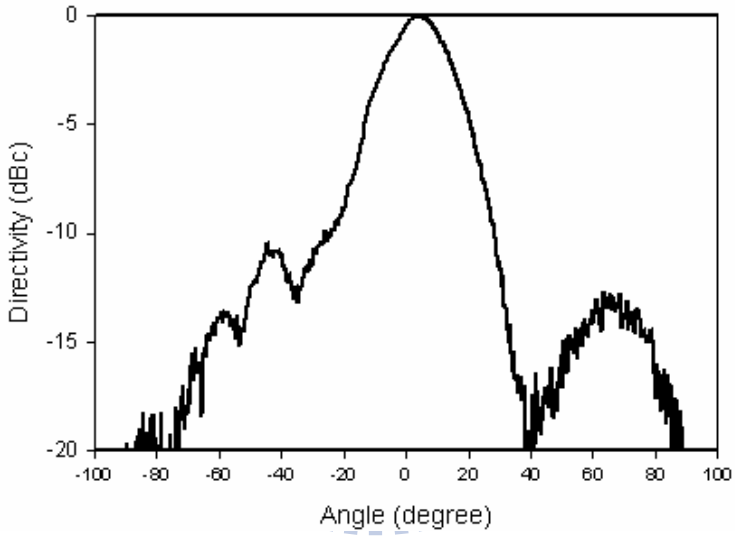

Figure 4.17 Measured antenna directivity of the patch-fed horn antenna.

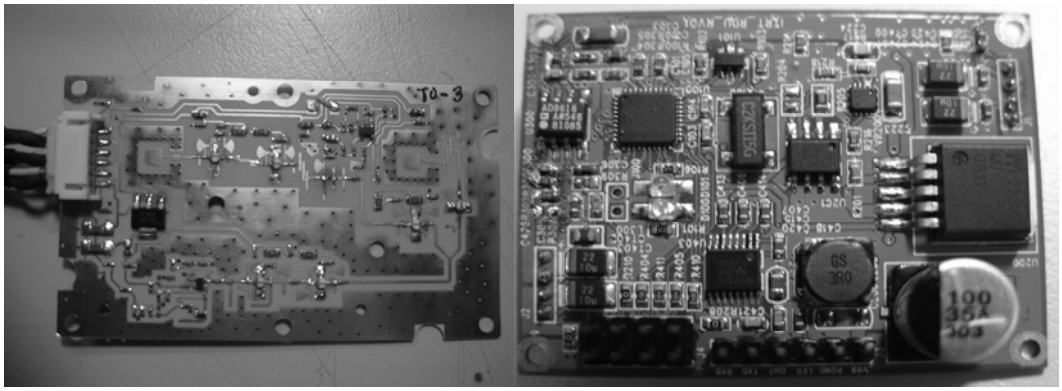

(a) (b)

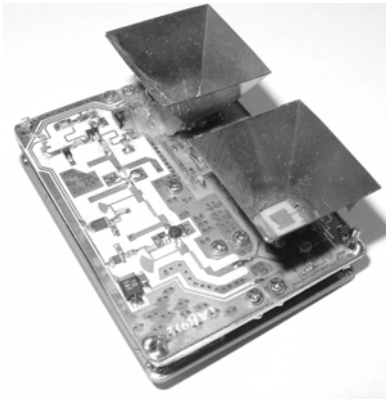

(c)

Figure 4.18 Photographs of (a) RF circuit board, (b) base-band circuit board, and (c) the integrated 24 GHz sideway-looking radar.

Figure 4.18 shows the photographs of the implemented 24 GHz sideway-looking radar system. The dimension of this module is 60 × 45 × 30 mm^3 (L × D × H). This size is acceptable to be integrated into the right / left back-mirror of a small vehicle. A 8051 based MCU ADuC831 is integrated into the base-band PCB. The MCU contains a 12-bit DAC (Digital-to-Analog Converter), which provides the tuning voltage waveform to the VCO. A DSP TMS320F2812 is also integrated in the back-side. The DSP acquires the IF signal by the ADC and performs the FFT function, then estimate the possible obstacle within the detecting region. Table 4-1 gives a summary of the integrated 24 GHz sideway-looking radar.

Table 4-1 The summary of the 24 GHz sideway-looking radar.

Operation frequency	24.125	GHz
Bandwidth	250	MHz
Maximal output EIRP	15	dBm
Power flatness	< 0.7	dB
Phase noise	-76	dBc/Hz
Sensitivity	< -90	dBm
Detection range	15	Meters
Field of view	30	Degrees
Distance resolution	0.6	meter
Power consumption	<3	Watts

Figure 4.19 shows a test result of the 24 GHz radar sensor. The horizontal axis indicates the target distance and the vertical axis shows the relative power in log scale. In this test, a small car and a person placed in a distance of 10 and 7 meters, respectively. There are two distinguishable peaks on this chart. Each peak represents a significant object. Noticeably, there is a big power observed near the zero distance. This peak is mainly contributed by the leaked power from Tx to Rx antenna.

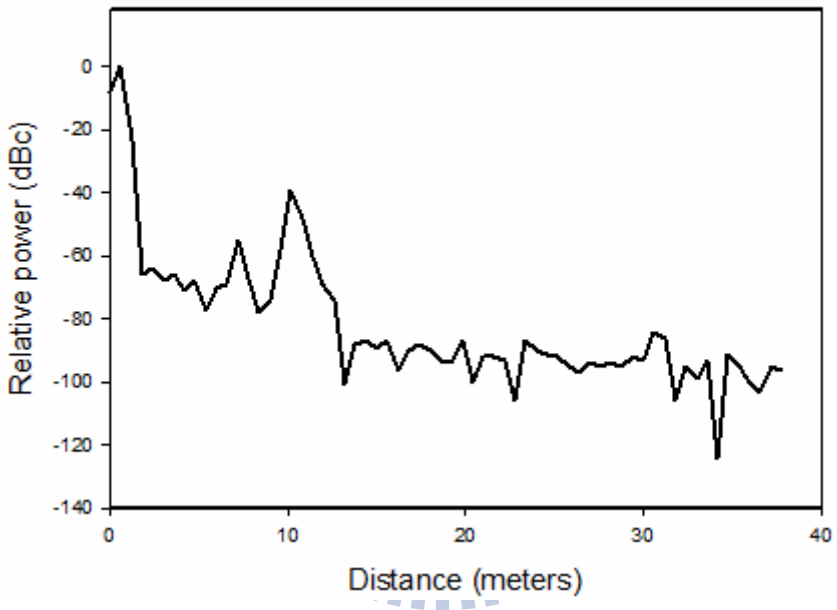

Figure 4.19 DSP result of the radar echo when two targets are located in a distance of 7 and 10 meters.

4.4 A 24 GHz FMCW radar for automotive obstacle detection

4.4.1 Implementation of the 24 GHz forward looking radar

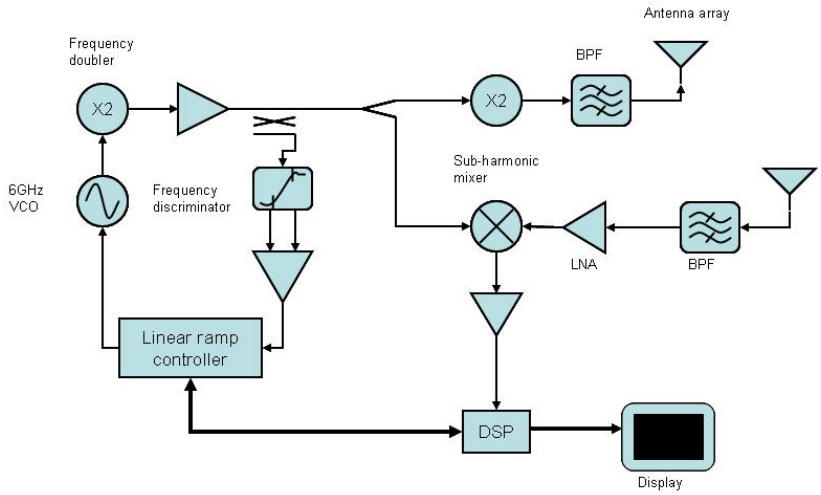

Figure 4.20 System block diagram of the 24 GHz forward-looking radar.

This forward-looking radar is to be installed inside the front bumper a car. Different to the 77 GHz system, the 24 GHz forward-looking radar covers a region up to 20 meters long. Figure 4.20 shows the system block diagram of the proposed 24 GHz forward-looking radar system. Referring to the sideway-looking system, the RF source is generated from a 6 GHz VCO. The transmitting signal is multiplied to 24 GHz by two frequency doublers. A SHM is used as the down-converter, which converts the radar echo to base-band signal directly. An additional LNA is use in this system to provide better signal-to-noise ratio (SNR). A frequency discriminator based frequency linearizer is also integrated into the system. A MCU is used to monitor the modulated frequency and then generate the adjusted tuning voltage to the VCO.

Figure 4.21 shows the architecture of the 9x8 series-fed patch antenna array used in the forward-looking system. Along the x-axis, each element within the series-fed antenna chain is designed independently, before integration. Treating the elements like two-port resistive elements, the input / output impedances are designed uniformly and the insertion phase difference are all zero. The radiating resistance of the center element

is higher than that of the side elements, thus, a bow-type power distribution is arranged and results in lower side-lobe level (SLL). Along the y-axis, a Chebyshev power distributing network is designed for the lowest SLL.

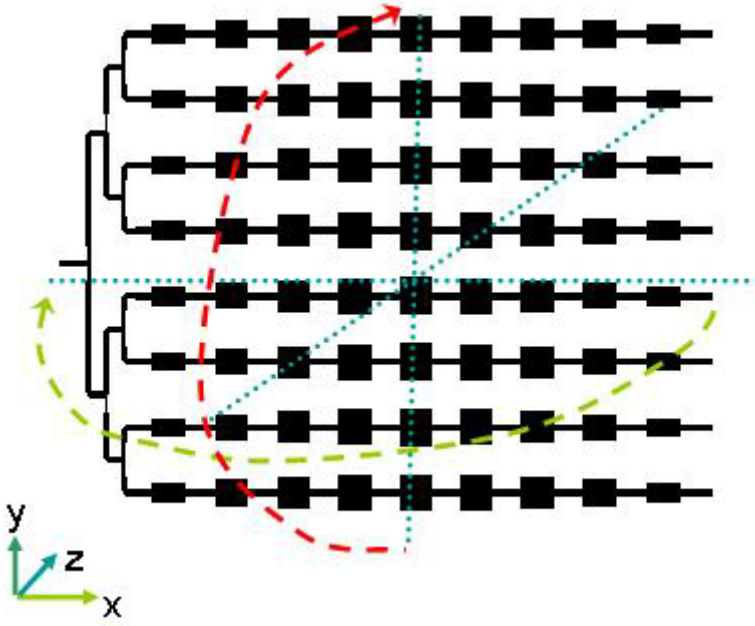

Figure 4.21 Architecture of the 9x8 series-fed antenna array.

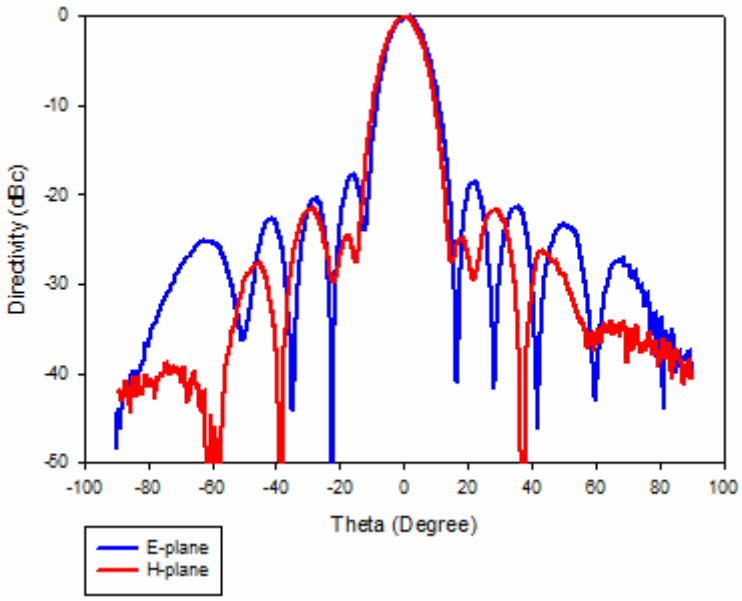

(a)

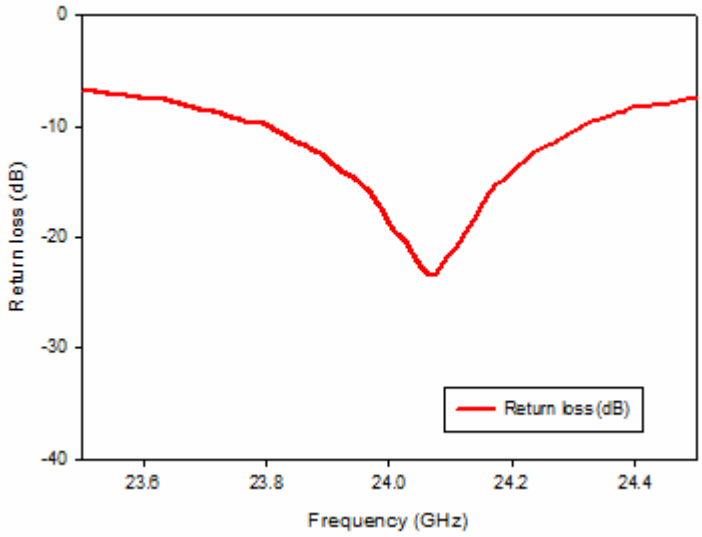

(b)

Figure 4.22 (a) The antenna directivity and (b) return loss of the 9x8 series-fed antenna array.

Figure 4.22 gives the measured antenna performances of the fabricated 9x8 series-fed antenna array. The developed antenna has a 10 dB bandwidth of 600 MHz from 23.7 to 24.3 GHz. The peak gain of the antenna is 18.5 dBi measured in the board-side direction. The largest side-lobe level is 18.8 and 21.2 dBc lower than the peak in the E- and H- plane, respectively. The half-power beam-width is 10.5 and 11.2 degrees in E- and H-plane respectively.

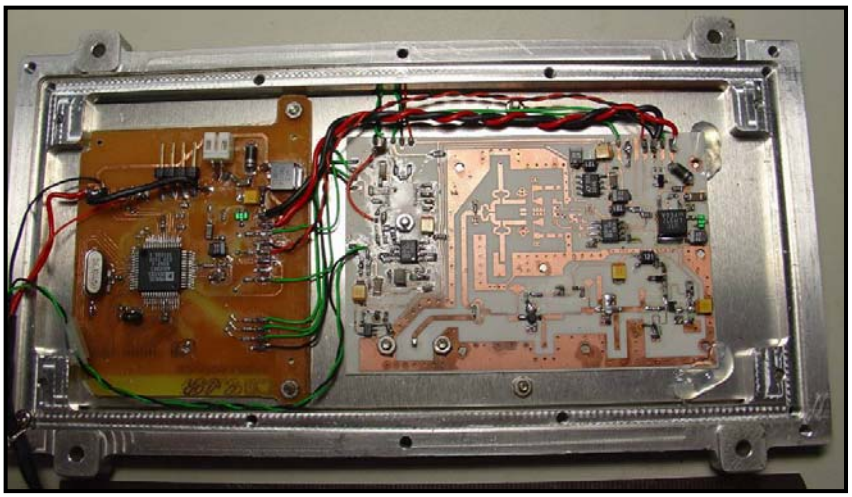

(a)

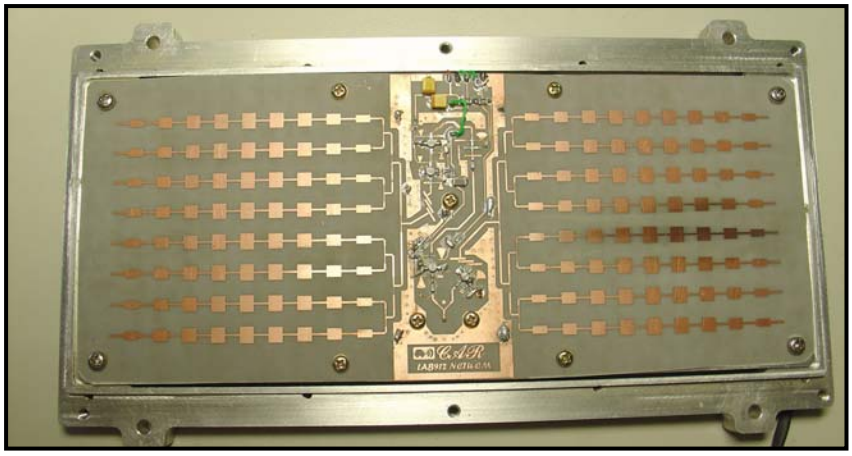

(b)

Figure 4.23 (a) Backside and (b) front-side photographs of fabricated 24 GHz forward-looking radar system.

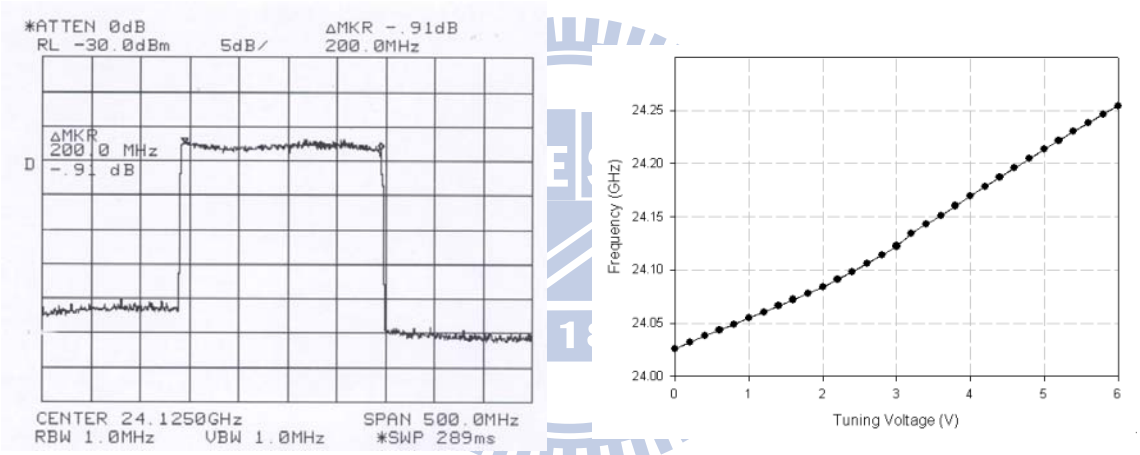

(a) (b)

Figure 4.24 Transmitting (a) power and (b) frequency of the forward-looking radar.

Figure 4.23 shows the photographs of the integrated 24 GHz forward-looking radar. The VCO, 6 to 12 GHz doubler, 12 GHz gain block, and frequency discriminator are integrated in the backside. A tuning voltage controller PCB is also integrated. In the front-side, a 12 to 24 GHz frequency doubler, a 24 GHz LNA, SHM, and two 9x8 series-fed antenna array are implemented. Figure 4.24 gives the output performances of the implemented radar. The maximal output EIRP is 23 dBm. During the frequency sweep range, the power variance is lower than 0.7 dB.

A frequency linearizer mechanism is proposed in this radar transceiver. The purpose

of this mechanism is to compensate the non-linearity of VCO by adjusting the modulating waveform. Figure 4.25 shows the algorithm of the frequency linearizer mechanism. An initial ramp modulation signal is generated when power up sequence. The frequency discriminator output is compared to the ideal ramp (the goal). Then the difference between each sampling point is weighted and fed back to the modulating waveform. This algorithm is a close-loop control function, by changing the modulating waveform little by little, in the end the output from discriminator will approach to the ideal ramp.

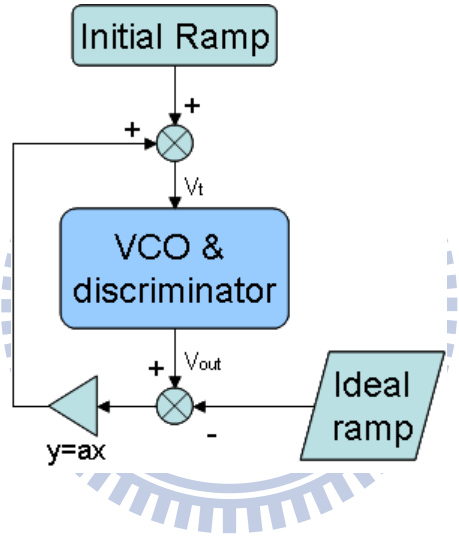

Figure 4.25 The frequency linearizer algorithm.

Figure 4.26 shows the experiment result of the frequency linearizer algorithm. In figure 4.26, (a) gives the modulating waveform and frequency discriminator output before linearization. In the beginning, the initial waveform is a pure saw-tooth wave (the upper chart). Because of the non-linear voltage-frequency characteristic of the VCO, the modulated frequency is not linear, a significant difference between the measured (white) and ideal (red) line, that a 9 % maximal deviation observed. The linearized result shows in figure 4.26 (b). After several times of iterations, the tuning voltage changes and frequency linearity approaches to the goal (only 0.3% maximal deviation

observed).

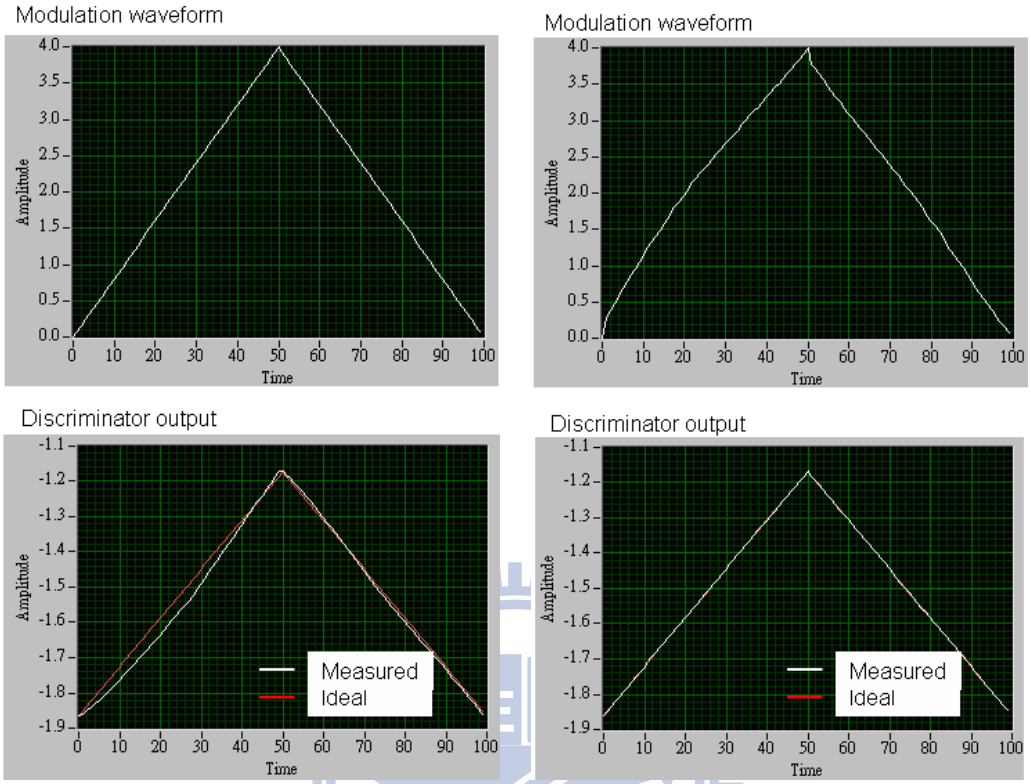

(a) (b)

Figure 4.26 Tuning voltage (up) and frequency discriminator output (down) of the frequency linearizer (a) before and (b) after linearization.

4.4.2 Implementation of 2D-FFT

In the forward-looking system, the relative speed with direction is quite important in the decision of warning level. However, the relative speed and distance information are mixed in the FMCW system. A 2D-FFT algorithm is presented to separate the speed and distance information into two different axes.

When detecting an object with relative speed, the Equ. (4-5) can be expressed in the complex form like:

$$IF(t) = \frac{M}{2}\left[e^{2\pi\left(\frac{2\alpha d}{c}+\frac{2 f_0 v}{c}\right)t+\theta_m} + e^{-2\pi\left(\frac{2\alpha d}{c}+\frac{2 f_0 v}{c}\right)t-\theta_m} \right] \qquad (4\text{-}6)$$

Within Equ (4-6), θ_m is a constant value for the same object, thus, if only looking for the magnitude of power spectrum, θ_m can be ignored. Obviously, there will be two signal peaks located in the frequency of $\frac{2\alpha d + 2f_0 v}{c}$ and $-\frac{2\alpha d + 2f_0 v}{c}$ when performing the complex Fourier-Transform. In most case, the Doppler frequency shift should be controlled much smaller than the resolution frequency of FMCW ramp. It means the Doppler frequency shift is not observable in the magnitude term when performing the DFT to a single ramp signal, thus it will not influence the distance measurement. A 2D-FFT mechanism is proposed in order to estimate the distance and speed of target at the same time.

The 2D-FFT mechanism uses number of FMCW ramps to obtain the requested speed information. Figure 4.27 illustrates the sampling mechanism for the 2D-FFT function.

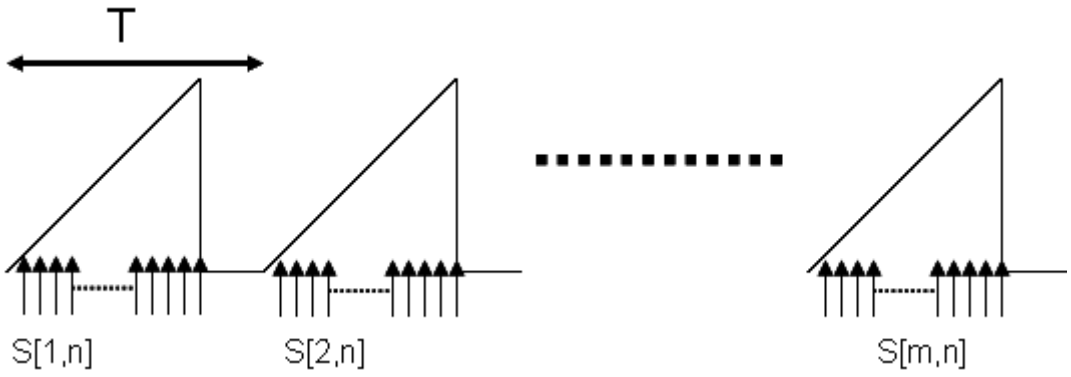

Figure 4.27 Sampling mechanism for the 2D-FFT function.

The echo waveform within the FMCW ramp duration is sampled by the sampling frequency f_S, where the ramp repeats in a repeating frequency f_T. Apply the periodic modulating function into Equ. (4-1), the transmitting signal can thus be re-written as:

$$Tx(m,t) = A\cos[2\pi(f_0 t + \frac{1}{2}\alpha t^2 + \theta_0 + m\theta_{acc})] \quad (4\text{-}7)$$

Where m is the index of specific FMCW ramp, and θ_{acc} is the constant accumulated phase difference within the ramp duration. The IF output can thus be expressed like:

$$IF(m,t) = \frac{M}{2}\begin{bmatrix} e^{2\pi\left(\frac{2\alpha d}{c}+\frac{2f_0 v}{c}\right)t+\theta_m} \times e^{2\pi\frac{2f_0 vT}{c}m} \\ +e^{-2\pi\left(\frac{2\alpha d}{c}+\frac{2f_0 v}{c}\right)t-\theta_m} \times e^{-2\pi\frac{2f_0 vT}{c}m} \end{bmatrix} \quad (4\text{-}8)$$

After performing the Fourier-Transform over the t-axis on each FMCW ramp, the power spectrum density at a specific frequency index of $\frac{2\alpha d}{c}$ can be expressed as:

$$P_{\frac{2\alpha d}{c}}(m) = K_p e^{\frac{4\pi f_0 vT}{c}m} \quad (4\text{-}9)$$

From this result, speed and moving direction of the object can be obtained by performing the complex Fourier-Transform again over the m-axis. The sign of speed is also distinguishable from this result.

Figure 4.28 shows the whole DSP flow chart of the 24 GHz forward-looking radar using the 2D-FFT algorithm. In the following experiment, the sampling frequency of the implemented system is set to 200 KHz. 128 points are sampled within each FMCW ramp, where 64 ramps are acquired for one process. From the ADC output, a digital filter is inserted to filter out the DC component. Because the ADC and DAC maybe not running synchronously, the start point of each ramp signal needs to be aligned first. Then perform the t-axis FFT to obtain the target distance information. After the t-axis FFT, perform the m-axis FFT to estimate the speed information. The m-axis FFT can be performed for only the specified distance index to minimize the calculating time. Figure

4.29 shows a screen shot of the 2D-FFT result. The x-axis indicates the target distance while the y-axis shows the relative speed. In this experiment, a human located in a distance of 11.5 meters is moving toward the radar with a relative speed of 4 km/hr. There is a significant spot in the 2D power spectrum, which indicates the relative distance and speed.

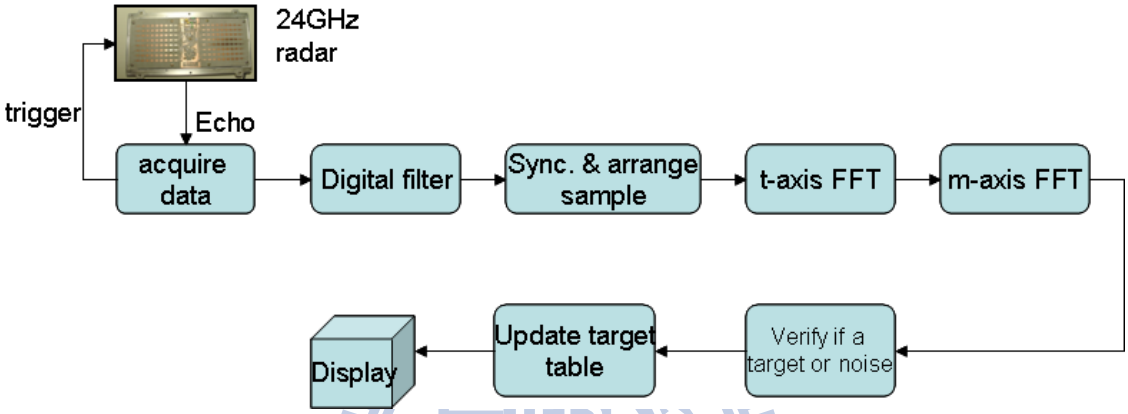

Figure 4.28 DSP flow chart of the 24 GHz forward-looking radar system.

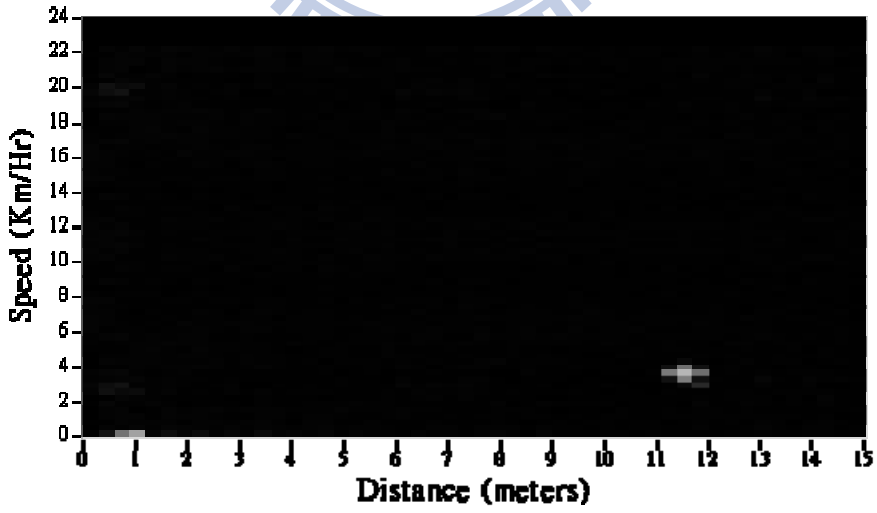

Figure 4.29 A screen shot of the 2D power spectrum. (A human in 11.5 meters away moving toward the radar with relative speed 4 km/hr).

E S A
1896

Chapter 5 A Compact RF Front-End Configuration for Short-Range Communication

Due to the dramatic increase of the wireless personal communication need in recent years, many new transceiver architectures have been proposed to simplify the circuit configuration and to reduce the system cost. These designs may not focus on increasing the communication range but emphasize on the communication convenience in the near proximity of the users. This chapter proposes a compact RF front-end configuration for short-range communication using a novel full-duplex bi-directional amplifier. The configuration uses single path for the transmitting / receiving signals. Without using any signal switch or diplexer, the proposed architecture is suitable to be applied to both half-duplex and full-duplex systems.

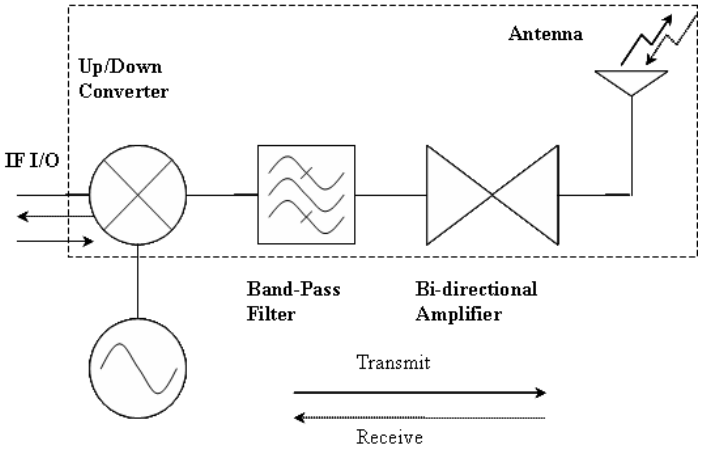

Figure 5.1 Block diagram of the transceiver front-end using the full-duplex bi-directional amplifier.

Figure 5.1 shows the block diagram of the proposed RF front-end architecture. The front-end is composed of a full-duplex bi-directional amplifier, a band-pass filter, a balanced mixer, and a planar Yagi-antenna. The operating frequency of this RF front-end is around 10 GHz. The proposed bi-directional amplifier provides gain to both the incoming and outgoing signals, simultaneously. The band-pass filter is used to filter

out the image signal and out-band signals such as harmonics and noises. The balanced mixer serves as a frequency up / down converter at the same time. In this study, an external RF signal generator is connected to the circuit. All the circuits and antenna are developed on the RT/duroid 5880 20-mil substrate.

5.1 The design of full-duplex bi-directional amplifier

As illustrated in chapter-2, the proposed bi-directional amplifier consists of a 90° -hybrid and two reflection-type amplifiers. A branch-line coupler is used as the 90° -hybrid, with two ports connected to the reflection-type amplifiers and the other two as the I/O ports of the bi-directional amplifier. The reflection-type amplifier is designed using a NE32584C p-HMET. Figure 5.2 illustrates the schematic of the reflection type amplifier. The reflection-type amplifier is designed from the negative impedance concept. In the source terminal of transistor, a short-stub and open fan architecture are connected. These architectures are used to force the transistor unstable in the required frequency band. The I/O port is placed in the drain terminal of the transistor for the purpose of obtaining the maximal output power. A quarter wave impedance matching network is connected to the drain of transistor to achieve the required signal gain. Figure 5.3 shows the simulated and measured gain of the reflection-type amplifier. The measured maximal gain obtained at 9.7 GHz is 13 dB.

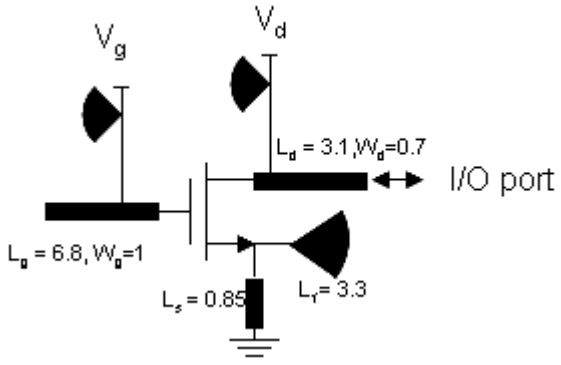

Figure 5.2 Schematic of the reflection-type amplifier.

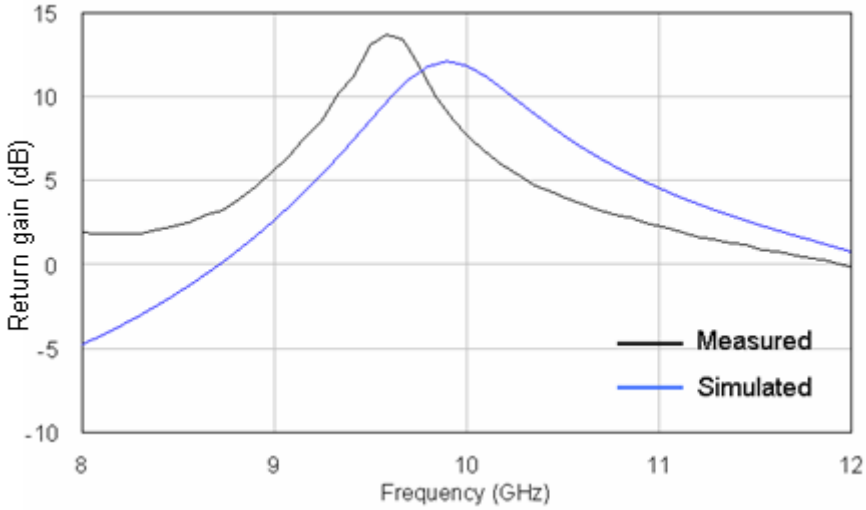

Figure 5.3 Simulated and measured return gain of the reflection-type amplifier.

Signals coming from either the I/O ports of the bi-directional amplifier are equally split by the branch line coupler with 90° phase difference. These signals are enhanced and reflected from the reflection-type amplifiers, then the reflected signals sum up at the output port and cancel with each other at the input port because of a 180° round-trip phase difference. In theory, the bi-directional gain of bi-directional amplifier is equal to the gain of each reflection-type amplifier, and the power handling capability will be twice larger because the power into a reflection-type amplifier is only half of the input power to the amplifier. The symmetry in circuit structure results in a balanced gain in both forward and reverse directions. Figure 5.4 shows the photograph of the implemented bi-directional amplifier. Figure 5.5 shows the measured gains of the bi-directional amplifier in both forward and reverse directions. It is seen that the frequency responses of the forward and reverse gains match quite well. In the range from 9.6GHz to 9.8GHz, both the measured gains are larger than 10dB. The observed peak gains are located around 9.7GHz with levels about 13.5 dB.

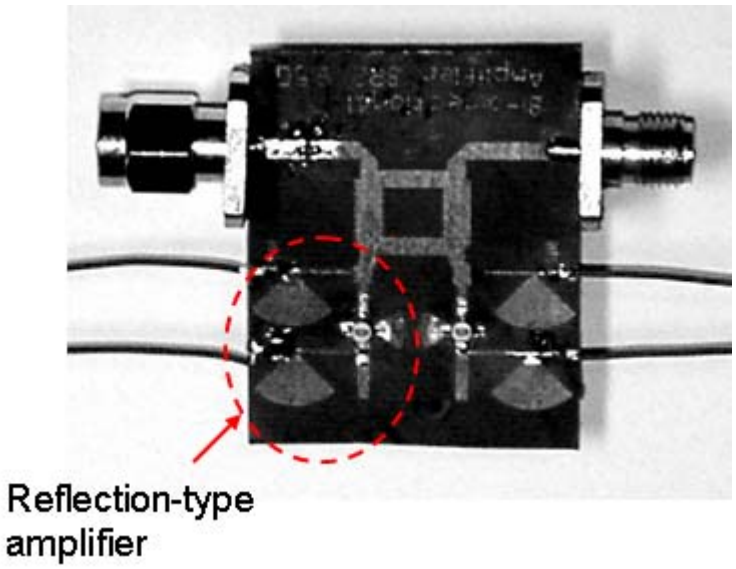

Figure 5.4 Photograph of the bi-directional amplifier.

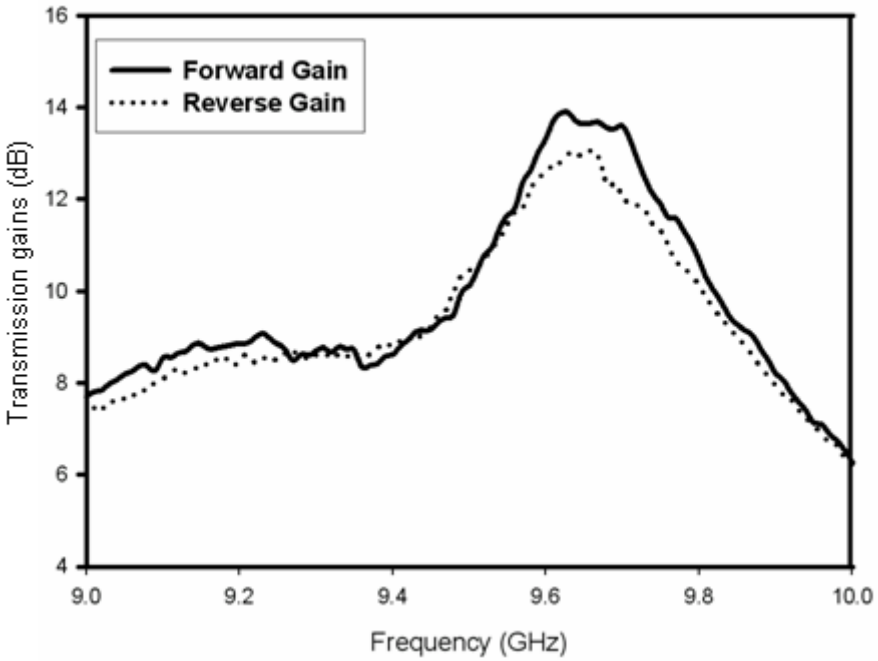

Figure 5.5 Measured bi-directional gains of the bi-directional amplifier.

5.2 The implementation of bi-directional transceiver

The proposed RF front-end includes a bi-directional amplifier, a balanced mixer, a band-pass filter (BPF), and an antenna. The mixer is composed of a 180°-hybrid and two Schottky diodes, which is used to up-convert the transmitting signal to the RF and to

down-convert the received signal to the IF frequency. The measured up and down conversion losses of the balanced mixer are 5.3 and 5.1 dB, respectively, when the LO power is 8 dBm. In the measurement, the LO, IF, and RF frequencies are set as 9.35 GHz, 400 MHz, and 9.75 GHz, respectively. The BPF is designed as a second-order folded edge-coupled microstrip (ECM) filter with a relative bandwidth of 5 %. The measured insertion loss of the band-pass filter is 1.8 dB and the half power bandwidth extends from 9.6 GHz to 9.9 GHz. Because the bi-directional amplifier enhances the power in both forward and reverse directions, the amplifier is relatively easy to self-oscillate when input / output ports are not well matched. To avoid self-oscillation in the bi-directional amplifier, a wide-band antenna is needed in the study. To this end, a printed Yagi-antenna with seven directors [41] is adopted. Figure 5.6 shows the measured return loss of the designed antenna. The antenna shows a 10 dB bandwidth of 1.3 GHz from 8.6 to 9.9 GHz. Figure 5.7 gives the simulated radiation patterns in both E- and H-planes. From this result, the directivity of the antenna is 12 dBi. The half-power beam width is around 40° in both E- and H- planes.

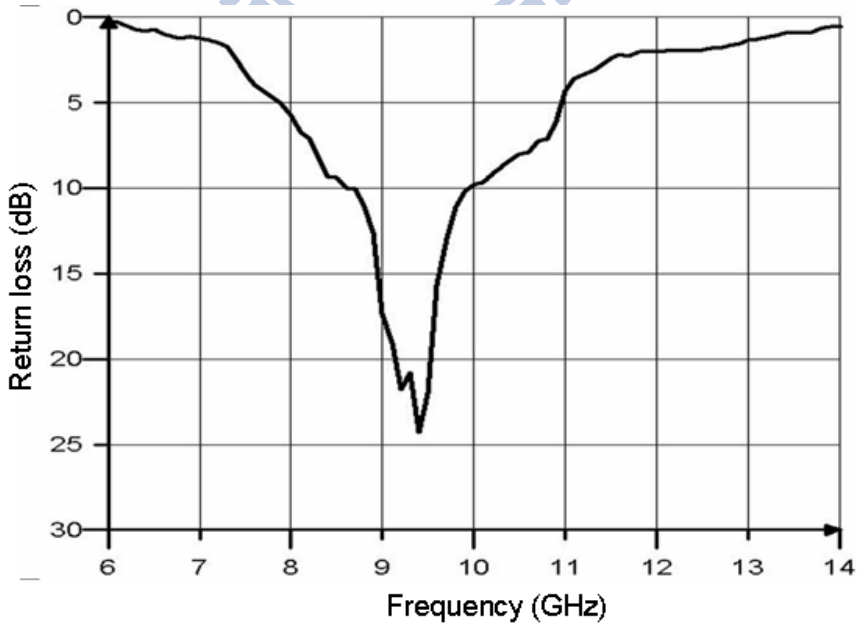

Figure 5.6 Measured return loss of the designed planar Yagi-antenna.

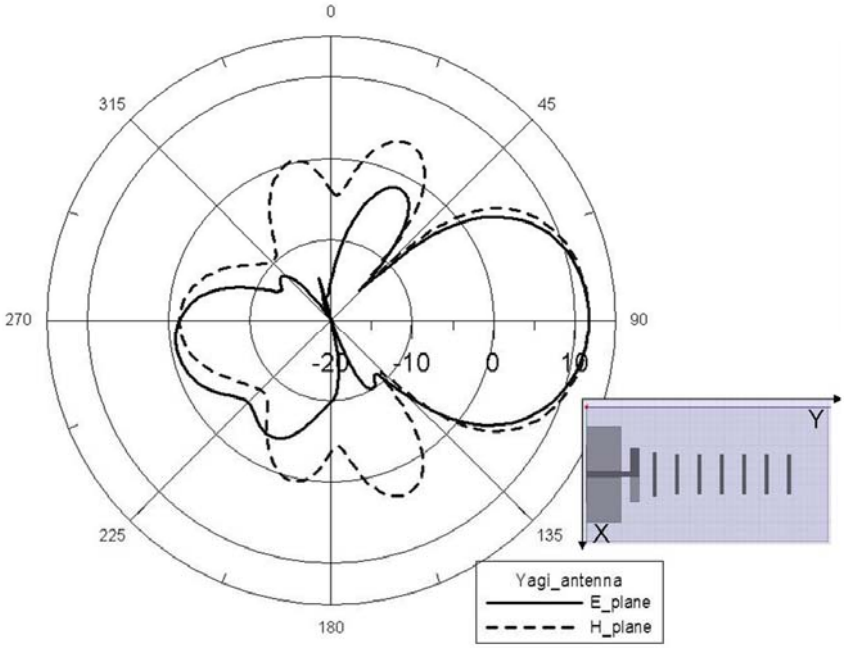

Figure 5.7 Simulated radiation pattern of the planar Yagi-antenna.

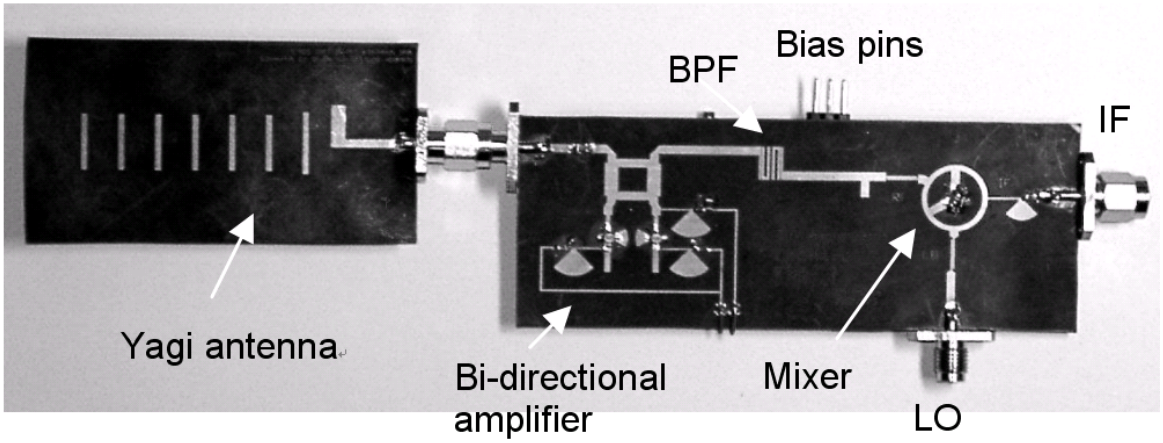

Figure 5.8 Photograph of the implemented transceiver front-end using the bi-directional amplifier architecture.

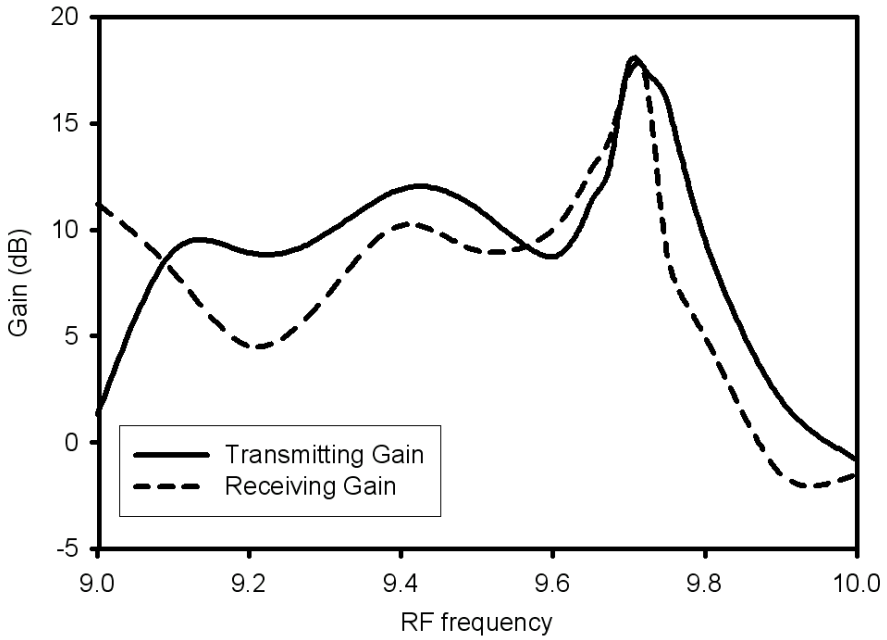

Figure 5.9 Measured overall conversion gain of the bi-directional transceiver front-end.

Figure 5.8 shows a photograph of the implemented RF front-end using the proposed bi-directional amplifier, the components are integrated on a single substrate with a dimension of 130 x 40 mm^2. Figure 5.9 shows the measured transmission gains of the integrated RF front-end from IF to space. In this measurement, a standard horn antenna used to receive / transmit the power from / to the RF front-end. The observation antenna was placed in a distance of 5 meters away. The transmitted and received power was calibrated using a standard antenna before this measurement. It is seen that the integrated RF front-end achieves an overall gain of 17 dB from RF to IF in both transmitting and receiving modes. This value is quite approximate to the summation of the gains / losses of the bi-directional amplifier, band-pass filter, mixer, and antenna. The estimated maximum EIRP of the front-end is 15.5 dBm and the measured overall noise figure is 10.5 dB. The noise figure is mostly contributed by the reflection-type amplifiers in the bi-directional amplifier. The IO port is located at the FET drain terminal of the reflection-type amplifier, which may result in a larger noise figure [42].

E S A
1896

Chapter 6 Conclusion

The development of vehicle collision warning radars and short-range communication RF front-end was illustrated. In the chapter-2, three new quadrature hybrid composed circuits were presented. A new LO transparent hybrid mixer architecture was proposed. The proposed hybrid mixer is composed of a quadrature hybrid and two Schottky diodes, with the unique characteristic to pass the LO power through, which is suitable to be used to simplify the radar front-end complexity. A new LO transmissive quadrature hybrid mixer using the proposed hybrid mixer was developed. The quadrature hybrid mixer was designed to have similar characteristics to the proposed hybrid mixer but output quadrature signals. A novel full-duplex bi-directional amplifier was also presented. The bi-directional amplifier has the characteristic to amplify the signals in two directions, which is proposed to simplify a RF transceiver front-end architecture.

In chapter-3, a Doppler radar using the new quadrature hybrid mixer was presented. A LO transmissive quadrature hybrid mixer and a 10.5 GHz radar transceiver were implemented. The implemented quadrature hybrid mixer showed 3.1 dB LO to RF insertion loss and 15.5 dB conversion loss from RF to base-band when the LO power was 10 dBm. Only small performance regressed when the LO power dropped to the value as low as 0 dBm. Within the 10.5 GHz radar system, a 5.25 GHz frequency synthesizer with the defected-gound-structure was implemented for the requirement of excellent frequency stability. It had been measured that the frequency synthesizer had output phase noise of -110 dBc/Hz. The integrated 10.5 GHz radar had output power of 6 dBm with adjustable frequency range from 10.36 to 10.74 GHz. Compared to the conventional single antenna quadrature radar, the radar using the proposed LO transmissive quadrature hybrid mixer had more than 3 dB power enhancement in the received signal strength. The proposed one also had the ability to be optimized for

different LO power levels. This result implies about 1.2 times of the detection range was achieved. The experiment showed that the presented radar still worked when the LO power reduced to the level below 0 dBm. The implemented radar had been demonstrated to be operated as a road-side-unit in a traffic management system to monitor the traffic flow and a speed sensor to measure the vehicle speed, which provides a speed resolution of 0.25 km/hr. It is also able to detect the sign of the Doppler shift due to the quadrature radar technology. The image rejection ratio of the implemented one was better than 25 dBc. With high local power usage efficiency, compact size, and capability to operate under low local power condition. The proposed radar architecture using the LO transmissive quadrature hybrid mixer is ready to be utilized in many radar applications.

In chapter-4, two complete 24 GHz vehicle collision warning radar systems were illustrated. The radars were developed for the sideway-looking and forward-looking applications, respectively. A complete radar front-end was implemented includes a 6 GHz VCO, active frequency doublers, amplifiers, and antennas. The FMCW technique was adopted in these radar systems to measure the object distance with relative simpler circuit complexity. The implemented sideway-looking one had ability to detect a human within 8 meters, field-of-view 30 degrees, which fulfills the requirement of blind-spot warning system. In the forward-looking system, a 9x8 series-fed patch antenna array was developed. The implemented antenna showed a gain of 18.5 dBi, with side-lobe level lower than 18.8 dBc in both E- and H- planes. A modulation frequency linearizer mechanism was also verified in this system. The result showed the modulation linearity deviation improved from 9 % to 0.3 %. The signal processing mechanism was also implemented in the 24 GHz radar systems. A 2D-FFT algorithm was presented to measure the object relative speed and distance, simultaneously. The implemented forward-looking radar had the capability to measure a human in 15 meters with

field-of-view angle 10 degrees. The developed front-end architecture and the signal processing mechanism were verified and ready to be utilized for automotive applications.

In chapter-5, a full-duplex RF front-end using a novel bi-directional amplifier was presented. A transceiver front-end architecture was proposed for the short-range wireless communication applications, which contains a bi-directional amplifier, a up / down conversion mixer, a band-pass filter, and an antenna. Using the bi-directional amplifier architecture, the requirements for RF signal switches or diplexers to separate the Tx / Rx signals are eliminated. The designed bi-directional amplifier provided a gain of 13.5 dB in both Tx / Rx direction. The measurement overall conversion gain from base-band signal to emission was 17 dB at 9.7GHz for both Tx /Rx modes. The estimated maximal output EIRP of the designed one was 15dBm.

The LO transparent hybrid mixer architecture was verified in a low power Doppler radar system, the future work is suggested to implement this architecture into a large power system or a FMCW radar system. The future works of the bi-directional amplifier is to improve the amplifier noise figure and maximal output power in the meantime.

E S A
1896

References

[1] H. H. Meinel, “Commercial applications of millimeter waves history, present status, and future trends,” *IEEE Trans. Microw. Theory Tech.*, vol. 43, no. 7, pp. 1639–1653, Jul. 1995.

[2] M. E. Russell, C. A. Drubin, A. S. Marinilli, W. G. Woodington, M. J. D. Checcolo, “Integrated automotive sensors, ” *IEEE Trans. Microw. Theory Tech.*, vol. 50, no. 3, pp. 674–677, Mar. 2002.

[3] D. Ward, N. Tanaka, J. Short, A. Steiner, “50 by 50 global fuel economy initiative”, *United Nations Information Network*, Mar. 2009.

[4] Y. Zhao, *Vehicle Location and Navigation System*. London: Artech House, 1997.

[5] A. E. Braun, “Intelligent transportation system: mirage or reality?” *Microwave Journal*, pp.22-38, Aug. 1997.

[6] P. Varaiya, “Smart car on smart roads: problem of control,” *IEEE Trans. Automatic Control*, vol.38, no.2, Feb. 1993.

[7] P. L. Lowbridge, “Low cost millimeter-wave radar systems for intelligent vehicle cruise control applications,” *Microwave Journal*, pp.20-33, Oct. 1995.

[8] S. Tokoro, “Automotive application systems of a millimeter-wave radar,” *IEEE Proc. of Intelligent Vehicles Symp*, pp. 260-265, 1996.

[9] R. Feger, C. Wagner, S. Schuster, S. Scheiblhofer, H. Jager, A Stelzer, “A 77 GHz FMCW MIMO radar based on an SiGe single-chip transceiver,” *IEEE Trans. Microw. Theory Tech.*, vol. 57, no. 5, pp. 1020–1035, May 2009.

[10] H. H. Meinel, “Automotive radar and related traffic applications of millimeterwaves,” *1997 Topical Symp. On Millimeter Waves*, pp. 151 –154, 1998.

[11] P. L. Lowbridge, P. Brigginshaw, B. Kumar, “A low cost mm-wave cruise control system for automotive applications,” *Microwave Journal*, pp.24-36, Oct. 1993.

[12] K. W. Chang, “Forward-looking automotive radar using a W-band single-chip transceiver,” *IEEE Trans. Microw. Theory Tech.*, vol.43, pp.1659-1668, July 1995.

[13] Millitech Corporation, “Crash avoidance FLR sensors,” *Microwave Journal*, pp.122-126, July 1994.

[14] D. A. Williams, “Millimeter wave radars for automotive applications,” *IEEE MTT-s Int. Microwave Symp*. Dig., vol.2, pp.721-724, New Mexico, June 1992.

[15] L. H. Eriksson, B. O. As, “A high performance automotive radar for automatic AICC,” *IEEE International Radar Conf.*, pp.380-385,1995.

[16] H. H. Meinel, “Atomotive millimeterwave radar,” *Digest of 2000 Topical Symposium on Millimeter Waves*, Yokosuka, Japan, March, 2000.

[17] D. Richardson, “An FMCW radar sensor for collision avoidance,” *IEEE Conf. on Intelligert Transpertation System*, pp.427-432, 1997.

[18] J. T. G. Partida, P. A. Gonzalez, M. B. Garcia, B. P. D. Naranjo, J. I. Alonso, "Through-the-wall surveillance with millimeter-wave LFMCW radars", *IEEE Trans on Geoscience and Remote Sensing*, Vol. 47, No. 6, pp. 1796-1805, Jun. 2009.

[19] S. J. Chung, S. M. Chen, Y. C. Lee, "A novel bi-directional amplifier with applications in active Van Atta retrodirective arrays", *IEEE Trans. Microw. Theory Tech.*, vol. 5, pp. 542-547, Feb. 2003.

[20] L. Roselli, F. Alimenti, M. Comez, V. Palazzari, F. Placentino, N. Porzi, A. Scarponi, "A cost driven 24 GHz Doppler radar sensor development for automotive applications," *IEEE Radar Conf.*, pp. 335-338, Oct. 2005.

[21] J. Wenger, "Automotive mm-wave radar: status and trends in system design and technology," *IEE Automotive Radar Navigat. Tech. Colloq.*, pp. 1/1–1/7, Feb. 1998.

[22] F. Placentino, F. Alimenti, A. Battistini, W. Bernardini, P. Mezzanotte, V. Palazzari, S. Leone, A. Scarponi, N. Porzi, M. Comez, L. Roselli, "Measurements of length and velocity of vehicles with a low cost sensor radar Doppler operating at 24GHz**,**" *IEEE Int. Workshop Advan. In Sensors and Interface*, pp. 1-5, Jun. 2007.

[23] S. T. Nicolson, P. Chevalier, B. Sautreuil, S. P. Voinigescu, "Single-chip W-band SiGe HBT transceivers and receivers for Doppler radar and millimeter-wave imaging", *IEEE Journal Solid-State Circuits*, vol. 43, no. 10, Oct. 2008.

[24] S. Kim, C. Nguyen, “A displacement measurement technique using millimeter-wave interferometry,” *IEEE Trans. Microw. Theory Tech.*, vol. 51, no. 6, pp. 1724-1728, Jun. 2003.

[25] S. Kim, C. Nguyen, “On the development of a multifunction millimeter-wave sensor for displacement sensing and low-velocity measurement,” *IEEE Trans. Microw. Theory Tech.*, vol. 52, no. 11, pp. 2503-2512, Nov. 2004.

[26] A. D. Droitcour, O. B. Lubecke, V. M. Lubecke, J. Lin, G. T. A. Kovacs, “Range correlation and I/Q performance benefits in single-chip silicon Doppler radars for noncontact cardiopulmonary monitoring,” *IEEE Trans. Microw. Theory Tech.*, vol. 52, no. 3, pp. 838-848, Mar. 2004.

[27] A. Vergara, N. Petrochilos, O. B. Lubecke, A. H. Madsen, V. Lubecke, “Blind source separation of human body motion using direct conversion Doppler radar,” *IEEE MTT-S Int. Microw. Symp. Dig.*, Jun. 2008, pp. 1321-1324.

[28] C. Fager, K. Yhland, H. Zirath, “A balanced FET FMCW radar transceiver with improved AM noise performance,” *IEEE Trans. Microw. Theory Tech.*, vol. 50, no. 4, pp. 1224-1227, Apr. 2002.

[29] C. Y. Kim, J. G. Kim, S. Hong, “A Quadrature radar topology with Tx leakage canceller for 24-GHz radar applications,” *IEEE Trans. Microw. Theory Tech.*, vol. 55, no. 7, pp. 1438-1444, Jul. 2007.

[30] C. Y. Kim, J. G. Kim, D. Baek, S. C. Hong, “A circularly polarized balanced radar front-end with a single antenna for 24-GHz radar applications”, *IEEE Trans. Microw. Theory Tech.*, vol. 57, no. 2, pp. 293-297, Feb. 2009.

[31] T. Tukii, S. G. Houng, M. J. Schindler, “Wideband bidirectional MMIC amplifiers for new generation T/R module”, *IEEE MTT-S Digest*, vol. 2, pp. 907-910, 1990.

[32] J. W., Archer, O. Sevimli, R. A. Batchelor, “Bi-directional amplifiers for half-duplex transceivers”, *IEEE GaAs IC Symp.*, pp.251-254, 1999.

[33] E. A. M. Klumperink, S. M. Louwsma, G. J. M. Wienk, B. Nauta, “A CMOS switched transconductor mixer,” *IEEE Journal Solid-State Circuits*, vol. 39, no. 8, pp. 1231-1240, Apr. 2004.

[34] D. M. Pozar , *Microwave Engineering*, 3rd edition, John Wiley & Son , pp. 333-336, 2003.

[35] *IE3D electromagnetic simulator*, Zealand Software, USA., 1997.

[36] *Microwave Office*, AWR Corporation, El Segundo, CA, USA, 2002.

[37] J. W. Carr, “The stabilization of mixer diode performance against L.O. power changes with optimum DC bias,” *IEEE Trans. Microw. Theory Tech.*, vol. 11, no. 2, pp. 123-129, Mar. 1963.

[38] D. Ahn, J. S. Park, C. S. Kim, J. Kim, Y. Qian, T. Itoh, “A design of the low-pass filter using the novel microstrip defected ground structure,” *IEEE Trans. Microw. Theory Tech.*, vol. 49, no. 1, pp. 86-93, Jan. 2001.

[39] Y. T. Lee, J. S. Lim, J. S. Park, D. Ahn, S. Nam, “A novel phase noise reduction technique in oscillators using defected ground structure,” *IEEE Microw. Wireless Compon. Lett.*, vol. 12, no. 2, pp. 39-41, Feb. 2002.

[40] *Intelligent Transportation Systems – Land changing decision aid system – performance requirements and test procedure*, ISO/TC204/WG14/N40.30 Jul, 2005.

[41] Y. C. Lee, S. J. Chung, “Design of a 38-GHz printed Yagi antenna with multiple directors”, *IEEE AP-S int, Symp.*, vol. 3, pp.606-609, 2001.

[42] L. Boglione, R. D. Pollard, V. Postoyalko, “Optimum noise-source reflection-coefficient design with feedback amplifiers”, *IEEE Trans. Microwave Theory Tech.*, vol. 45, pp.402-407, Mar. 1997.

Appendix

Abbreviation	Full name
ACC	Adaptive cruise control
ADC	Analog to digital converter
APTC	Advanced public transportation system
ATIS	Advanced traveler information system
ATMS	Advanced traffic management system
AVCSS	Advanced vehicle control and safety system
BLDS	Blind sport detecting system
BPF	Band pass filter
CVO	Commercial vehicle organization
CW	Continuous wave
DAC	Digital to analog converter
DFT	Discrete Fourier transform
DGS	Defected ground structure
DSP	Digital signal processor
ECM	Edge coupled microstrip
FFT	Fast Fourier transform
FMCW	Frequency modulated continuous wave
FOV	Field of view
HPBW	Half power beam width
IF	Intermediate frequency
ITS	Intelligent transportation system
LNA	Low noise amplifier
LO	Local oscillator
LPF	Low pass filter
MCU	Micro-controller unit
PLL	Phase lock loop
RF	Radio frequency
SHM	Sub-harmonic mixer
SLL	Side lobe level
TCXO	Temperature compensated crystal oscillator
UNEP	United Nations environment programme
VCO	Voltage controlled oscillator

Vita

Tan-Hsiung Ho was born on November 27, 1980, in Yunlin county, Taiwan, R.O.C. He received the B.S. and M.S. degrees in communication engineering from the National Chao-Tung University, Hsinchu, Taiwan, in 2002 and 2003 respectively. He is currently working toward the Ph.D. degree in communication engineering in the National Chiao-Tung University, Hsinchu, Taiwan, R.O.C. His current research interests include the microwave circuitry, automotive radar system, and antenna.

Publication List

Journal Papers:

[1] T. H. Ho, S. J. Chung, “Compact RF front-end configuration for short-range communication", *IEE Electronic Letters*, vol. 40, No. 5, pp. 314-315, Mar,. 2004.

[2] T. H. Ho, S. J. Chung, “A 2-D Amplifying Array Using Multi-Ported Aperture-Coupled Patch Antennas,” *IEICE Trans. Communications*, Vol.E92-B, No.07, pp.2461-2467, Jul. 2009.

[3] T. H. Ho, S. J. Chung, "Design and Measurement of a Doppler Radar with New Quadrature Hybrid Mixer for Vehicle Applications," *IEEE Trans. Microwave Theory Tech.*, Vol. 58, Issue 1, pp.1-8,Jan. 2010.

[4] G. -.F. Cheng, T. –H. Ho, W. –T. Wang, C. -Y. Chang and S. -J. Chung, "Highly Integrated Automotive Radar Sensor" , *Electronics Letters*,. Vol. 43, Issue 18, pp. 993 – 994, Aug. 2007.

Conference Papers:

[1] T. H. Ho, S. J. Chung, “Development of A 24-GHz FMCW Radar for Automotive Obstacle Detection,” *APMC Digest*, pp. 134, Session B3-3, India, Dec., 2004.

[2] T. H. Ho and S.-J. Chung, "A compact Doppler radar using a new hybrid mixer for vehicle speed detection" , Symp. on Millimeter-Waves (TSMMW2004), YRP, Yokosuka, Japan, Feb, 2004.

[3] T. H. Ho, S. J. Chung, "A Compact 24 GHz Radar Sensor for Vehicle Sideway-Looking Applications" , *2005 EuMC*, Paris, Oct., 2005, pp. 351-354

[4] T. H. Ho, S. J. Chung, "24 GHz radar transceiver for large-vehicle sideway collision warning application", *CSTRWC0*5, Beijing, Aug., 2005.

Book Chapter

[1] S. J. Ching, T. H. Ho, “Van Atta Array Reflector”, *the six-volume Wiley Encyclopedia of RF and Microwave Engineering*, 2004.